Conductive Networks of Plasma-Synthesized Zinc Oxide Nanocrystals

A Dissertation
SUBMITTED TO THE FACULTY OF
UNIVERSITY OF MINNESOTA
BY

Benjamin L. Greenberg

IN PARTIAL FULFILLMENT OF THE REQUIREMENTS
FOR THE DEGREE OF
DOCTOR OF PHILOSOPHY

Prof. Uwe R. Kortshagen & Prof. Eray S. Aydil, Advisers

October 2017

in memory of Jihua Yang

Contents

Figures ..... **iii**
Table ..... **iii**
1. Introduction **1**
1.1 Applications of semiconductor nanocrystal networks 1
1.2 The insulator-metal transition in semiconductor nanocrystal networks 3
1.3 Localized surface plasmon resonance 7
1.4 The utility of ZnO nanocrystals 9
1.5 Plasma synthesis of ZnO nanocrystals 11
1.6 Thesis overview 14
2. Aluminum doping in the plasma **17**
2.1 Introduction 17
2.2 Results and discussion 18
2.3 Conclusion 29
2.4 Experimental methods 30
3. Photodoping and photonic sintering: approaching the insulator-metal transition **35**
3.1 Introduction 35
3.1 Results and discussion 38
3.3 Conclusion 50
3.4 Experimental methods 50
4. Crossing the insulator-metal transition **53**
4.1 Introduction 53
4.2 Results and discussion 53
4.3 Conclusion 61
4.4 Experimental methods 61
5. Technological potential **63**
5.1 Introduction 63
5.2 Plasmonic nanocomposites of zinc oxide and titanium nitride 63
5.2 Thermopower and thermal conductivity 65
5.3 Reducing roughness and porosity with hydraulic compaction 67
5.4 Attaining high air-stable conductivity without atomic layer deposition 69
5.5 Synthesis at atmospheric pressure 70
References **74**
Appendix A: Supporting information for chapter 2 ..... **86**
Appendix B: Supporting information for chapter 3 ..... **91**
Appendix C: Copyright permissions **103**

Figures

Figure 1.1: NC applications. 2
Figure 1.2: Schematics of hopping transport mechanisms 5
Figure 1.3: Insulator-metal transitions (IMTs) 7
Figure 1.4: Localized surface plasmon resonance (LSPR) in NCs 8
Figure 1.5: Flexible perovskite solar cell 10
Figure 1.6: Nonthermal plasma synthesis of ZnO NCs 12
Figure 1.7: Elemental maps of a ZnO NC network infilled with Al_2O_3 by ALD 13
Figure 2.1: TEM and FTIR of AZO NCs 20
Figure 2.2: Effect of quantum confinement on the LSPR 23
Figure 2.3: Schematic representations of AZO NC doping 26
Figure 2.4: Evidence of lattice-expanding defect in the AZO NCs 27
Figure 2.5: Electrical resistivity of AZO NC films with and without etching 29
Figure 3.1: IMTs and IPL-based treatment strategy. 36
Figure 3.2: Evolution of ρ with sintering IPL 40
Figure 3.3: FTIR absorption spectra evolution with IPL dose 42
Figure 3.4: Room-temperature σ, μ, and n vs. number of IPL flashes 45
Figure 3.5: Temperature dependence of σ of IPL treated films. 47
Figure 4.1: Strategy for crossing the IMT 55
Figure 4.2: LSPR and electron transport at the IMT 56
Figure 4.3: Results of UV irradiation experiments far from the IMT 58
Figure 4.4: $n\rho^3$ near the IMT 60
Figure 5.1: ZnO/TiN nanocomposite 65
Figure 5.2: Hydraulic compaction of ZnO NC networks 68
Figure 5.3: Strategy for achieving high air-stable σ without ALD 70
Figure 5.4: APGD synthesis of ZnO NCs 71

Table

Table 5.1: Thermoelectric properties of ZnO NC networks 67

1. Introduction

1.1 Applications of semiconductor nanocrystal networks

Nearly all modern electronic devices are based on semiconductors—materials more electrically conductive than insulators but less conductive than metals. A critical feature of these materials is that their electronic properties can be controlled by altering the density of free charge carriers. Whereas the free carrier density of a metal is typically fixed at one carrier per atom, that of a semiconductor is highly variable and largely determined by impurities in the material. Modulation of the carrier density by intentional introduction of impurities is known as doping.

Some electronic properties, however, are not easily controlled by doping. One such property is the bandgap—the fundamental energy gap between bound and free electrons—which is an influential parameter in any application. For example, the bandgap is generally the primary determinant of a semiconductor's light emission spectrum and thus dictates applicability in light-emitting diodes and display technologies. While the bandgap can change at very high doping levels, the change is typically small and accompanied by other effects that compromise light emission.

The key asset of semiconductor nanocrystals (NCs) is that they can attain properties not accessible by simply modifying the composition of conventional bulk semiconductors. Typically defined as crystalline semiconductor spheroids less than 100 nm in diameter (at least one thousand times smaller than the width of a human hair), semiconductor NCs offer their size as an additional powerful tuning parameter. When the NC radius is comparable to the Bohr exciton radius—the size of the bound electron-hole pairs (excitons) responsible for light emission—the bandgap becomes highly tunable. For example, CdSe has a Bohr exciton radius of ~5 nm, and the peak light emission of a CdSe NC can be tuned across the entire visible spectrum by varying the NC radius from ~1 to ~3 nm.[1] Size reduction, in combination with surface effects, can also be used to obtain full-spectrum emission from Si NCs, as shown in Figure 1.1.a.[2] This dependence of optical/electronic properties on NC size is known as quantum confinement; hence

semiconductor NCs are often referred to as "quantum dots". So-called quantum dot displays, currently the predominant commercial application of semiconductor NCs, employ the tunable light emission of CdSe or InP NCs.

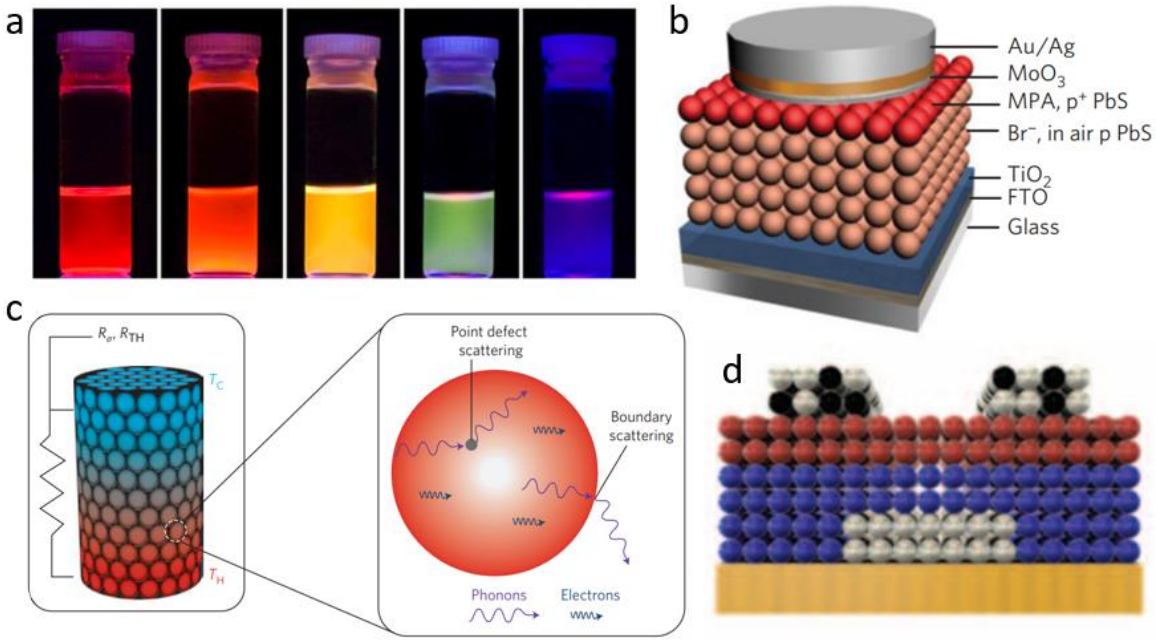

Figure 1.1: NC applications. (a) Photoluminescence of plasma-synthesized Si NCs dispersed in methanol.[*] The emission peak is tuned from red to green by quantum confinement, and blue emission is due to defect states. (b) Schematic of a quantum dot solar cell.[†] PbS NCs form the absorber layer. (c) Schematic of an NC-based thermoelectric generator.[‡] Nanostructuring can enhance thermopower and suppress thermal conduction. (d) Schematic of flexible field-effect transistor composed entirely of NCs.[§] CdSe, Ag/In, Ag, and Al_2O_3 NC networks form the semiconducting channel, source/drain electrodes, gate electrode, and gate insulator, respectively.

A promising route toward expanding the applicability of semiconductor NCs is to assemble them into networks. This approach can lead to materials with three important advantages over bulk semiconductors: (1) size-tunable properties within individual NCs, as described above, (2) interesting *network* properties that emerge when NCs are

[*] From "Air-stable full-visible-spectrum emission from silicon nanocrystals synthesized by an all-gas-phase plasma approach", *Nanotechnology*, 2008.[2] DOI: 10.1088/0957-4484/19/24/245603. © IOP Publishing. Reproduced with permission. All rights reserved.

[†] Reprinted by permission from Macmillan Publishers Ltd: *Nature Materials*, "Air-stable n-type colloidal quantum dot solids", copyright 2014.[3] DOI: 10.1038/NMAT4007.

[‡] Reprinted by permission from Macmillan Publishers Ltd: *Nature Nanotechnology*, "Prospects for thermoelectricity in quantum dot hybrid arrays", copyright 2015.[5] DOI: 10.1038/nnano.2015.289.

[§] From "Exploiting the nanocrystal library to construct electronic devices", *Science*, 2016.[6] Reprinted with permission from AAAS. DOI: 10.1126/science.aad0371.

consolidated, and (3) amenability to unconventional low-cost manufacturing techniques. Devices exemplifying these advantages are shown in Figures 1.1.b, c, and d, respectively. A quantum dot solar cell, shown in Figure 1.1.b, can exploit the tunable light absorption and potentially highly efficient exciton generation of quantum-confined PbS NCs.[3,4] A nanocrystalline thermoelectric generator, shown in Figure 1.1.c, can benefit from the enhanced thermopower and low thermal conductivity generally exhibited by NC networks.[5] A field-effect transistor composed entirely of NCs, shown in Figure 1.1.d, can be fabricated via room-temperature solution processing, allowing the use of flexible polymer substrates and potentially enabling roll-to-roll manufacturing.[6]

To produce high-performance commercially viable devices based on semiconductor NC networks, it is essential to understand and control the transport of charge and energy across the networks. A particularly difficult and important problem is attaining high electrical conductivity. In thermoelectric materials, high conductivity ($\geq 10^2\ \Omega^{-1}cm^{-1}$) is necessary for satisfactory power conversion efficiency. In solar cells, highly conductive NC networks could potentially replace layers currently composed of bulk materials (as will be discussed in Section 1.3) and thereby further reduce manufacturing costs. NC networks, however, are innately less conductive than bulk materials due to their disorder and high interparticle contact resistance. Therefore maximizing device performance requires a detailed examination of how these disadvantages limit conductivity and how they may be ameliorated.

1.2 The insulator-metal transition in semiconductor nanocrystal networks

By the definition given in the previous section, semiconductors are neither insulators nor metals and have electrical conductivity landing somewhere in the middle. However, a semiconductor's qualitative transport behavior typically falls into one of two categories: insulator-like or metal-like, i.e. charge carriers are either localized and their transport is thermally activated, or they are delocalized and their transport requires no activation. In this section we will use the terms "insulator" and "metal" to refer to these two types of semiconductors.

The vast majority of semiconductor NC networks described in the literature are insulators. In some cases, the NC surfaces are terminated in insulating ligands[7–9] (see Section 1.5), which present large energy barriers to interparticle charge transport. In other cases, the NCs are in direct contact,[10–13] but activation energies are still high due to energy level misalignment. With or without ligands, these systems exhibit Anderson localization (localization of free carriers due to disorder), which necessitates hopping transport: conduction proceeds via phonon-assisted tunneling of carriers between NCs. In this transport regime, an NC network can be modelled as a Miller Abrahams resistor network,[14] in which the resistance between NCs i and j is given by

$$R_{ij} = R_0 \exp\left[\frac{2r_{ij}}{\xi} + \frac{\varepsilon_{ij}}{k_B T}\right], \tag{1.1}$$

where r_{ij} is the distance between the NCs, ε_{ij} is the activation energy for interparticle tunneling, ξ is the electron localization length, k_B is Boltzmann's constant, T is the temperature, and the prefactor R_0 is generally assumed to be independent of T. The dominant conduction paths are dictated by minimization of R_{ij}.

Figure 1.2 shows the three possible types of hopping transport that may be observed in insulating NC networks. The key issue is that ε_{ij} can vary widely among NC pairs due to dispersion in ligand length, NC size, and other parameters. At high T, charge carriers readily acquire sufficient thermal energy to hop between adjacent NCs, regardless of ε_{ij}, and charge carriers simply take the path of lowest r_{ij}. In this case, nearest-neighbor hopping (NNR) occurs (Figure 1.2.a), and the temperature dependence of the network conductivity is described by a simple Arrhenius law,

$$\sigma \propto \exp\left[-\frac{E_a}{k_B T}\right], \tag{1.2}$$

where E_a is an activiation energy related to the ε_{ij}'s. At low T, however, variance in ε_{ij} becomes important, and charge carriers may hop farther in order to find paths of lower activation energy, i.e. the exponent of Equation 1.1 may be minimized at relatively high r_{ij}. In this case, variable-range hopping (VRH) occurs (Figure 1.2.b), and the temperature dependence of σ is weakened:

$$\sigma \propto \exp\left[-\left(\frac{T_0}{T}\right)^m\right], \tag{1.3}$$

where $m < 1$. Mott showed that when the density of states (DOS) is constant near the fermi energy, E_F, $m = ¼$ for a 3D material.[15] However, at high doping levels (several dopants per NC), the DOS is in fact typically nonconstant near E_F. This is due to dispersion in the number of dopants per NC, which causes some NCs (those with fewer dopants) to attain negative charge upon Fermi energy equilibration. This creates a "random energy landscape" in which there are many states near E_F, and the DOS function near E_F is determined by electron-electron interactions, which give rise to a parabolic Coulomb gap.[14] Under these conditions, Efros-Shklovskii VRH (ESVRH) occurs and $m = ½$.[16]

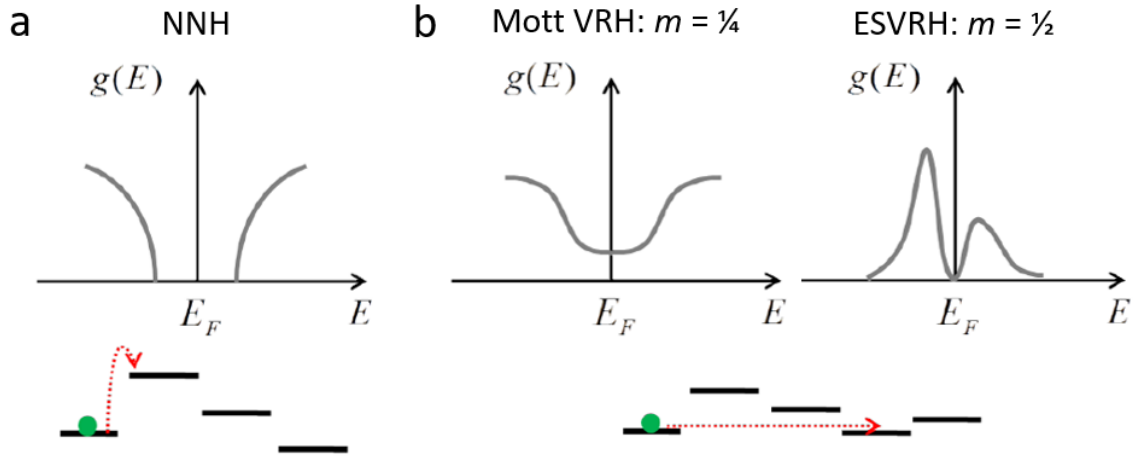

Figure 1.2: Schematics of hopping transport mechanisms and density of states (DOS) functions near the Fermi energy.[17] (a) Nearest-neighbor hopping (NNR). At high *T*, charge can hop between neighboring NCs, and the associated activation energy corresponds to a hard gap in the DOS. (b) Variable-range hopping (VRH). At low *T*, charge hops farther in order to minimize activation energy. A flat DOS near E_F corresponds to Mott VRH and a parabolic DOS near E_F (due to a Coulomb gap) corresponds to Efros-Shklovskii (ES) VRH.

In all of these hopping regimes, the high activation energy for interparticle conduction translates to electrical conductivity much lower than that of the bulk semiconductor. Approaching bulk conductivity requires crossing the insulator-metal transition (IMT), at which Anderson localization is eliminated and σ becomes independent of T. In principle, this transition o ccurs when the interparticle contact conductance equals the quantum conductance, $e^2/\pi\hbar$, at which point the width of electron energy levels becomes comparable to their spacing and the activation energy vanishes.[18] For NCs in direct contact, the interparticle conductance is given by

$$G_{\mathrm{i}} = \frac{e^2 {k_{\mathrm{F}}}^2 \rho^2}{4\pi\hbar}, \tag{1.4}$$

where e is the elementary charge, k_{F} is the Fermi wavevector, and ρ is the interparticle contact radius. Setting G_{i} equal to $e^2/\pi\hbar$ yields the IMT criterion $k_{\mathrm{F}}\rho \approx 2$. As shown in Figure 1.3.a, this formula states that the IMT occurs when the free carrier wavelength, k_{F}^{-1}, is comparable to ρ. Also, for large free carrier density, n, k_{F} is given by

$$k_{\mathrm{F}} = \left(\frac{3\pi^2 n}{g}\right)^{1/3}, \tag{1.5}$$

where g is the degeneracy of conduction band minima in the case of an n-type semiconductor (valence band maxima in the case of p-type), which leads to a simple IMT criterion in terms of n,[18]

$$(n\rho^3)_{\mathrm{c}} \approx 0.3g, \tag{1.6}$$

where $(n\rho^3)_{\mathrm{c}}$ denotes the critical value of $n\rho^3$. This IMT criterion for NC networks is analogous to the well-known Mott criterion for bulk semiconductors, illustrated in Figure 1.3b. When a bulk semiconductor exhibits insulating behavior due to large separation among charge donors, it is considered a Mott insulator. In this system an IMT can be induced by increasing n until the inter-donor spacing, $n^{-1/3}$, becomes comparable to the donor Bohr radius, a_{d}. Mott showed that this argument leads to the IMT criterion

$$(n{a_{\mathrm{d}}}^3)_{\mathrm{c}} \approx 0.02. \tag{1.7}$$

Combining Equations 1.6 and 1.7 produces the theoretical charge transport phase diagram shown in Figure 1.3.c. At low n, the Mott criterion is unsatisfied, and individual NCs are insulating. As n is increased, the NC network enters a regime where individual NCs are metallic, but the network remains insulating. The network becomes metallic only when the product $n\rho^3$ exceeds $0.3g$, which may occur at n significantly higher than that necessitated by the Mott criterion. For example, the critical n for the Mott transition in ZnO is ~4×10^{18} cm^{-3}, whereas for a ZnO NC network with $\rho \approx 1$ nm, the critical n for the network IMT exceeds 10^{20} cm^{-3}. Of course, since ρ appears as a cubic term in Equation 1.6, it is possible to reduce n dramatically by increasing ρ. This will be a key consideration when attempting to cross the IMT and maximize the conductivity of an NC network. However, as ρ approaches the NC radius, the network essentially becomes a

bulk semiconductor, and advantages such as quantum confinement or mechanical flexibility may be compromised. Hence it is necessary to understand how to control and measure both n and ρ in order to design highly conductive NC networks while maintaining other desirable properties of the NCs.

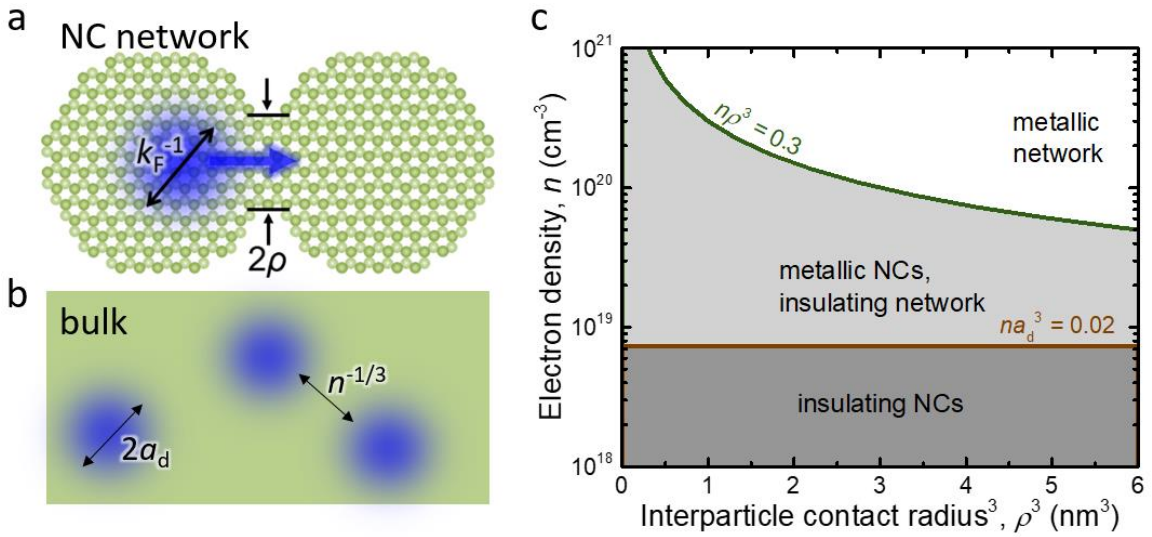

Figure 1.3: Insulator-metal transitions (IMTs). (a) A Mott IMT (equation 1.7) occurs in a bulk semiconductor when the inter-donor spacing, $n^{-1/3}$, becomes comparable to the donor Bohr radius, a_d. (b) In an NC network, an IMT (equation 1.6) occurs when the free carrier Fermi wavelength, k_F^{-1}, becomes comparable to the interparticle contact radius, ρ. (c) Theoretical charge transport phase diagram for NC networks based on equations 1.6 and 1.7. Here a_d is the donor Bohr radius of ZnO.

1.3 Localized surface plasmon resonance

Regardless of whether they exhibit high interparticle conductivity, heavily doped semiconductor NCs nearly always display high *intra*particle conductivity. This is typically observed optically: the free carriers in the NC oscillate collectively in response to incident light (Figure 1.4.a), and light is strongly absorbed near the carriers' resonant frequency. This phenomenon is known as localized surface plasmon resonance (LSPR). In an NC, the free carriers are localized by the restoring force supplied by charged donors (whereas in a dense film, charge oscillations propagate across the film surface). The resonant frequency is a function of the free carrier density, n; therefore n can be determined from optical measurements and modeling of the LSPR.

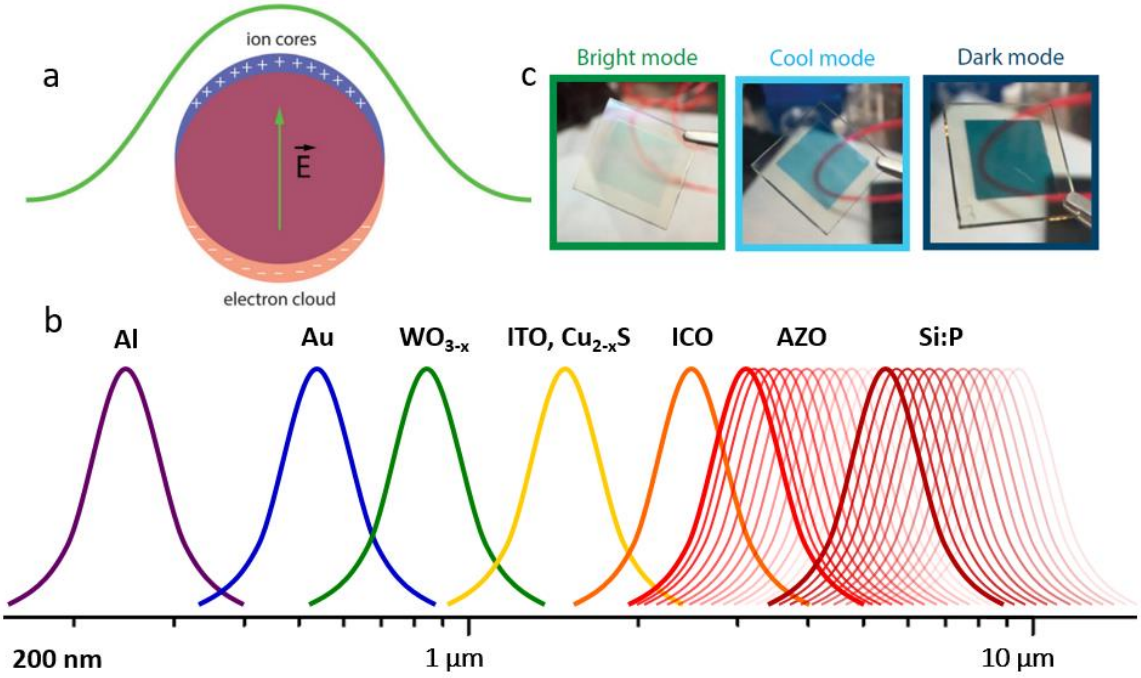

Figure 1.4: Localized surface plasmon resonance (LSPR) in NCs. (a) In an n-type semiconductor NC, free electrons oscillate in response to an applied electric field with a resonant frequency proportional to $n^{1/2}$. Positively charged donors supply the restoring force.[*] (b) Schematic of NC LSPR absorption features of Al,[19] Au,[20] WO_{3-x},[21] ITO,[22] $Cu_{2-x}S$,[23] ICO,[24] AZO,[25] and Si:P,[26] which have peaks ranging from the UV to the mid IR. (c) An electrochromic window in which the near-IR LSPR absorption of WO_{3-x} NCs is modulated electrochemically (absorption in the visible is due to NbO_x).[†]

The frequency-dependent dielectric function of a heavily doped semiconductor is given by the Drude equation,[27]

$$\varepsilon(\omega) = \varepsilon_\infty - \frac{{\omega_p}^2}{\omega^2 + i\omega\Gamma(\omega)}, \tag{1.8}$$

where ε_∞ is the high-frequency dielectric constant, $\Gamma(\omega)$ is the frequency-dependent carrier relaxation frequency, and ω_p is the plasma frequency given by

$$\omega_p = \sqrt{\frac{ne^2}{\varepsilon_0 m^*}} \tag{1.9}$$

where ε_0 is the permittivity of free space and m^* is the free carrier effective mass. Thus n can be extracted from an absorption spectrum if the dependence of absorption on the dielectric function is known. For a thin film composed of non-interacting NCs with

[*] "Nanostructured electrochromic smart windows: traditional materials and NIR-selective plasmonic nanocrystals", *Chem. Comm.*, 2014.[47] Published by The Royal Society of Chemistry.
[†] "Switchable Materials for Smart Windows", *Annu. Rev. Chem. Biomol. Eng.*, 2016.[31]

diameter much less than the wavelength of incident light, the absorption coefficient can be modelled using Mie theory:[28]

$$\alpha = \frac{18\pi\phi\omega}{c}\left(\frac{\varepsilon_2\varepsilon_m}{4\varepsilon_m{}^2 + 4\varepsilon_1\varepsilon_m + \varepsilon_1{}^2 + \varepsilon_2{}^2}\right), \quad (1.10)$$

where ϕ is the NC volume fraction, c is the speed of light, ε_1 and ε_2 are the real and imaginary parts of the NC dielectric function, and ε_m is the dielectric constant of the medium in which the NCs are embedded. Because Mie theory does not account for interparticle interactions, it is typically applied to ensembles of NCs with large interparticle spacing. As will be discussed in Chapter 3, effective medium approximations (EMAs) are often favored over Mie theory for networks of NCs in direct contact. Results presented in Chapter 4, however, will suggest that the absorption of NCs in direct contact can in fact be modelled accurately using Mie theory under certain conditions.

In addition to enabling optical measurement of n, LSPRs are useful in a variety emerging NC technologies.[29,30] As shown in Figure 1.4.b, a wide range of the electromagnetic spectrum is spanned by the LSPRs of various semiconductor and metal NCs, and in many cases the absorption peak of a particular semiconductor NC is widely tunable via doping. As shown in Figure 1.4.c, one intriguing (and photogenic) application of plasmonic semiconductor NCs is electrochromic smart windows. The near-IR absorption of these windows is due to the LSPR of oxygen-vacancy-doped WO_{3-x} NCs, which can be tuned dynamically by modulating n electrochemically.[31,32]

1.4 The utility of ZnO nanocrystals

While the aim of this thesis is to address fundamental questions about charge transport in semiconductor NCs in general, the experimental work presented herein is focused exclusively on NCs of ZnO. This is largely due to ZnO's amenability to control and measurement of electronic properties of interest. Like most metal oxides, ZnO generally does not undergo irreversible chemical or structural changes upon exposure to air at room temperature, which is a major advantage in studies requiring transfer of samples through the ambient among various synthesis and characterization chambers. For investigations of

the IMT, the key asset of ZnO is its direct bandgap, which obviates conduction band minima degeneracy, i.e. g = 1. This translates to a relatively attainable critical $n\rho^3$ compared to that of an indirect bandgap semiconductor such as Si (g = 6). For studies of the LSPR, doped ZnO offers a convenient resonant frequency typically ranging from 1000 to 3000 cm^{-1}, which enables measurement of n with a standard Fourier Transform infrared (FTIR) spectrometer. Because of these and other favorable properties as well as the availability of convenient low-cost ZnO synthesis precursors, ZnO NCs have been one of the most widely studied nanomaterials for over a decade; this popularity is itself a virtue to an experimentalist seeking a well-characterized prototypical material as a platform for basic science.

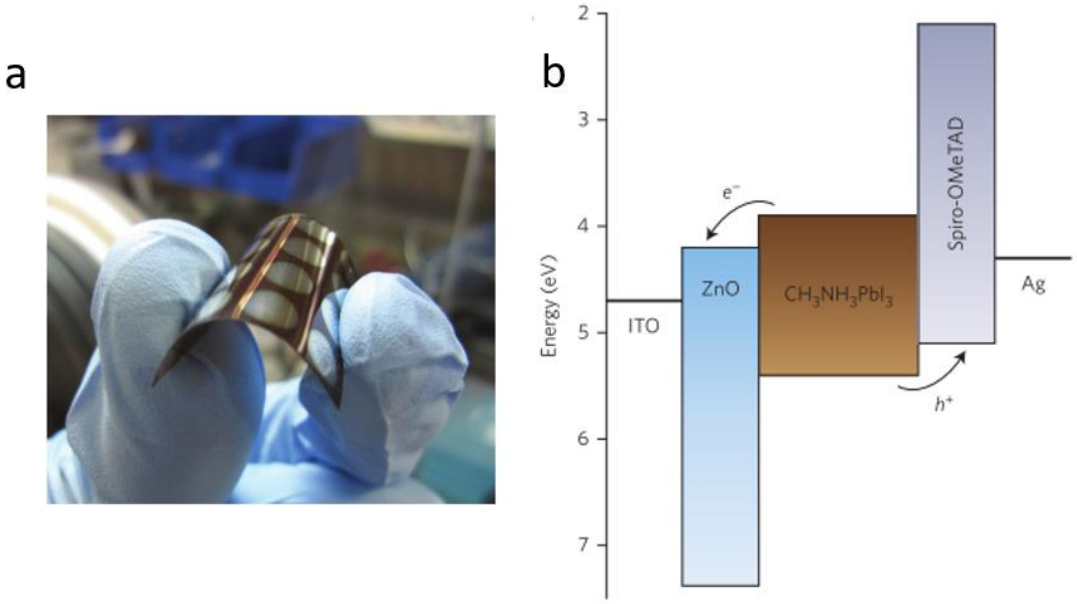

Figure 1.5: First flexible perovskite solar cell with power conversion efficiency (PCE) greater than 10% (PCE = 10.4%).[*] (a) Bending reduces the PCE by less than 15% even for bend radii less than 2 mm. (b) An energy level diagram shows that ZnO is well-suited for electron transport and hole blocking in this device.

Recently, ZnO NCs have also demonstrated considerable technological potential. In general, ZnO's wide bandgap (3.3 – 3.4 eV) and fairly high electron mobility (up to ~60 $cm^2V^{-1}s^{-1}$ in dense polycrystalline films grown by magnetron sputtering[33]) make it a

[*] Reprinted by permission from Macmillan Publishers Ltd: *Nature Photonics*, "Perovskite solar cells with a planar heterojunction structure prepared using room-temperature solution processing techniques", copyright 2013.[34] DOI: 10.1038/NPHOTON.2013.342.

promising transparent electron conductor. Doping with Al can increase n above 10^{20} cm^{-3}, typically resulting in σ between 10^3 and 10^4 $\Omega^{-1}cm^{-1}$. However, In-doped Sn_2O_3 (ITO), which typically has $\sigma \approx 10^4$ $\Omega^{-1}cm^{-1}$ and superior moisture tolerance, is overwhelmingly preferred for applications requiring high conductivity. Therefore, in solar cells and related devices, ITO is nearly always used as the transparent electrode for long-distance (lateral) electron transport, while ZnO is often used as a thin electron transport layer (ETL) for short-distance (vertical) electron transport and hole blocking, as shown in Figure 1.5.a. A sufficiently high-mobility ETL can be formed by ZnO NCs deposited via solution-based processes at room temperature;[34] a flexible perovskite solar cell based on this approach is shown in Figure 1.5.b (and quantum dot solar cells such as the one shown in Figure 1.1.b often employ similar ZnO NCs). Flexible ITO films, however, have to date been unable to match σ of rigid ITO films. A potential benefit of studying the IMT in ZnO NCs is gaining insights which may inform future design of highly conductive flexible ITO NC networks.

1.5 Plasma synthesis of ZnO nanocrystals

The majority of ZnO NCs (and most other semiconductor NCs) described in the literature are produced by colloidal synthesis. This method can produce high-purity crystalline NCs with low size dispersion (standard deviation <10%), and the average size is tunable via synthesis temperature and time. However, stabilizing the colloids and suppressing NC agglomeration generally necessitates long electrically insulating surface ligands. NCs from colloidal synthesis can be assembled into networks via solution-based coating processes such as spin coating or inkjet printing, but the resultant films have very low σ unless the ligands are somehow removed or replaced with short and/or conductive surface species.

Nonthermal plasma synthesis is an alternative approach which circumvents the ligand problem.[35,36] This method typically employs a low-pressure (1-10 Torr) radio-frequency (RF) Ar plasma in which there is a pronounced thermal nonequilibrium between electrons and heavy species (ions and neutrals). Electron temperature can reach ~40,000 K, whereas heavy species remain close to room temperature due to their larger

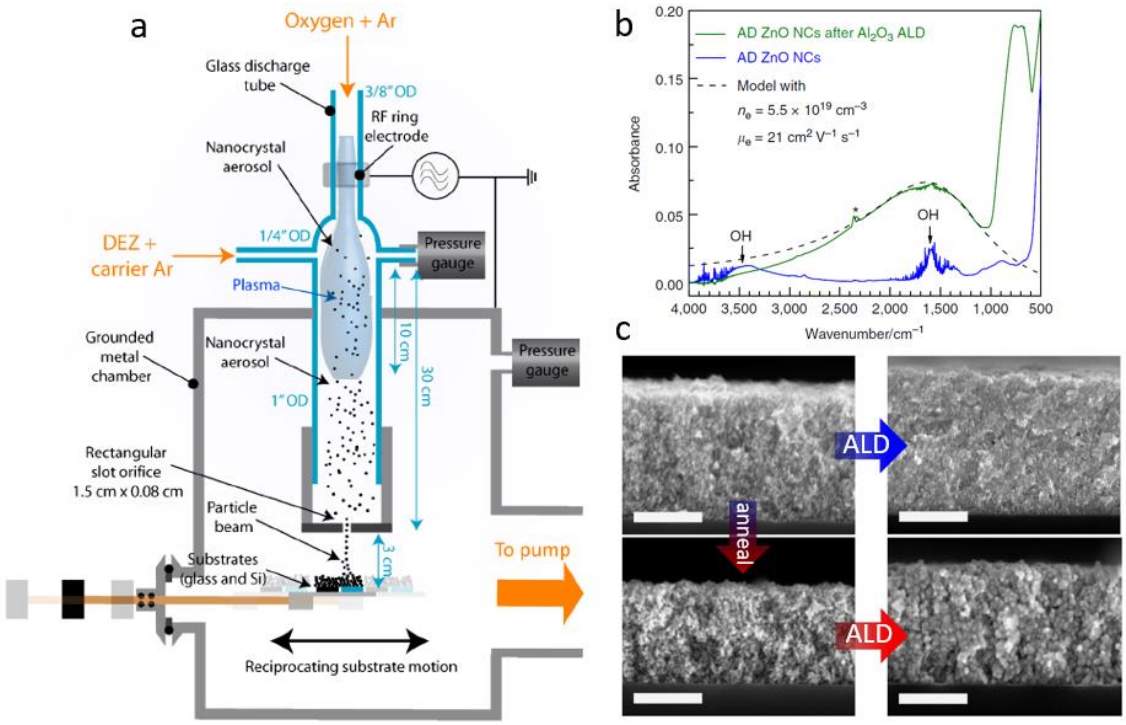

Figure 1.6: Nonthermal plasma synthesis and supersonic impact deposition of ZnO NCs.[*] (a) Schematic of synthesis and deposition system. (b) FTIR absorption spectra before and after a ZnO NC network is infilled with Al_2O_3 by atomic layer deposition (ALD). Infilling removes electron-trapping OH groups and seals the film, resulting in air-stable n = 5.5 x 10^{19} cm^{-3}, according to a fit of the LSPR absorption feature based on Mie theory. (c) Cross-sectional SEM of ZnO NC networks at various treatment stages. Clockwise from top left, network electrical conductivity is <10^{-9}, ~10^{-1}, 10^{1}, and 10^{-6} $\Omega^{-1}cm^{-1}$. Scale bars are 500 nm.

mass: ions absorb much less of the power supplied by the applied RF field than do the electrons, and both ions and neutrals receive little kinetic energy from collisions with fast but light electrons. Gaseous precursors are injected into the plasma, where they dissociate and ionize upon collisions with the hot electrons, generating highly reactive radicals and ions from which NCs nucleate and grow. Interparticle collision rates are suppressed by unipolar charging: NCs charge negatively because they collide more frequently with the high-velocity electrons than with the relatively low-velocity ions. This leads to low size dispersion that can approach that attained in typical colloidal synthesis as well as minimal agglomeration without the need for surface ligands. Moreover, NC synthesis can be seamlessly integrated with supersonic inertial impact deposition.[37,38] Feeding the NCs

[*] Reprinted by permission from Macmillan Publishers Ltd: *Nature Communications*, "High electron mobility in thin films formed via supersonic impact deposition of nanocrystals synthesized in nonthermal plasmas", copyright 2014.[39] DOI: 10.1038/ncomms6822.

through a nozzle into a lower-pressure (<100 mTorr) deposition chamber creates a supersonic particle beam, which forms a dense NC network upon impingement on a substrate translated perpendicularly to the beam.

Originally designed for the production of group IV semiconductor NC networks, this plasma-based synthesis/deposition process was recently adapted to ZnO.[39] A schematic of the ZnO reactor is shown in figure 1.6.a. Diethylzinc (DEZ) and O_2 were injected into an Ar plasma to form ZnO NCs with diameter $d \approx 7$nm, which were deposited supersonically to form films with thickness $t \approx 500$ nm and ZnO volume fraction $\phi \approx 35\%$. As deposited, the films had immeasurably low n and $\sigma < 10^9\ \Omega^{-1}\text{cm}^{-1}$ due to electron-trapping OH groups on the NC surfaces. These OH groups were removed by infilling the NC networks with Al_2O_3 by atomic layer deposition (ALD), resulting in an LSPR indicating $n > 10^{19}\ \text{cm}^{-3}$ (Figure 1.6.b) and $\sigma \approx 10^{-1}\ \Omega^{-1}\text{cm}^{-1}$. (Recently, EDX maps have confirmed that the infill is uniform, as shown in Figure 1.7). Thermally annealing the films prior to ALD further increased σ to $\sim 10^1\ \Omega^{-1}\text{cm}^{-1}$ (Figure 1.6.c), and σ was found to have a weak dependence on T suggestive of proximity to the IMT. However, control of n and ρ was not achieved and a detailed study of charge transport near the IMT was not conducted.

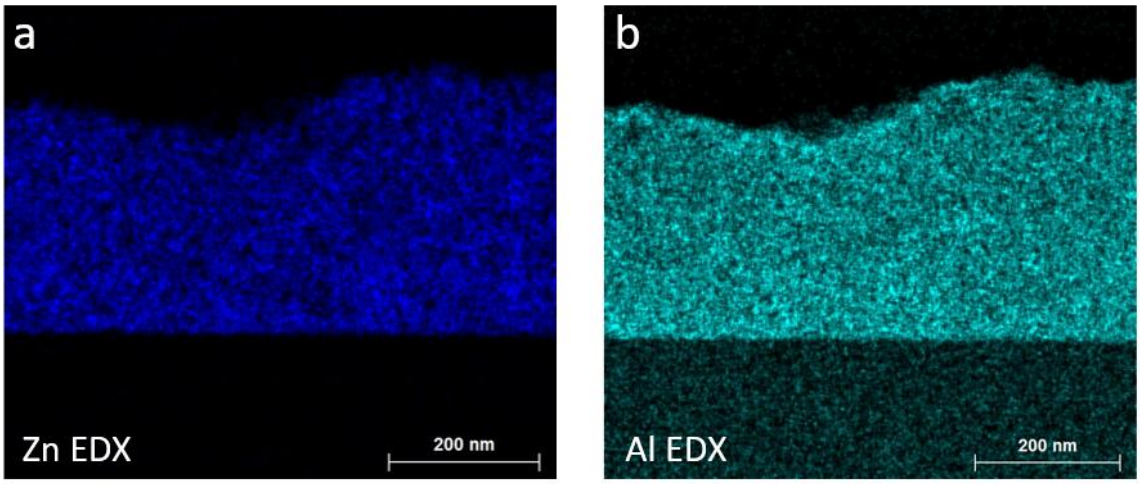

Figure 1.7: STEM-EDX elemental maps of a FIB-milled lamella of a ZnO NC network infilled with Al_2O_3 by ALD. The lamella is approximately 20-30 nm (two to three NC layers) in thickness. (a) Zn counts. (b) Al counts.

1.6 Thesis overview

To recapitulate Section 1.1, maximizing the applicability of semiconductor NCs requires fundamental understanding of charge transport across NC networks. The goal of this thesis is to tackle some of the critical questions surrounding a particularly difficult challenge in the field of NC network charge transport: achieving electrical conductivities comparable to those exhibited by bulk doped semiconductors. Specifically, does an IMT in fact occur when Equation 1.6 is satisfied? If so, how does an NC network behave near and beyond the transition, and how high can σ be raised? How can n and ρ be measured accurately, and can they be controlled using processes compatible with the ultimate goal of scalable low-cost production of NC-based devices? These questions and many others will be addressed through manipulation and detailed characterization of the structure and electron transport properties of ZnO NC networks produced using the plasma-based synthesis/deposition system shown in Figure 1.6.a.

We begin by endeavoring to control and measure n: Chapter 2 focuses on increasing n by doping the ZnO NCs with Al in the plasma synthesis reactor. This chapter was published in *Nano Letters* under the title "Nonequilibrium-Plasma-Synthesized ZnO Nanocrystals with Plasmon Resonance Tunable via Al Doping and Quantum Confinement". Prior to this work – as illustrated in Figure 1.4.b – ZnO NCs had been doped with Al in colloidal synthesis[25], and group IV semiconductor NCs had been doped with boron and phosphorous in nonthermal plasma synthesis,[26,40,41] but to our knowledge, no compound semiconductor had been impurity doped in a nonthermal plasma. Injecting an Al precursor into the ZnO NC synthesis plasma, we found that nonthermal plasma synthesis is in fact ideally suited for producing high-quality Al-doped ZnO (AZO) NCs. The NCs' LSPR absorption features and elemental maps from electron energy loss spectroscopy (EELS) suggested that Al dopants were distributed uniformly within the NCs and that a high fraction of them were electronically active. Moreover, high doping levels were maintained as the NC diameter was reduced to below 4 nm, enabling observation of a quantum confinement blueshift of the LSPR. However, Al doping did not increase σ, likely due to the formation of electrically insulating Al_2O_3 as a byproduct

of Al injection. This work was conducted in collaboration with Dr. Shreyashi Ganguly, Jacob Held, Dr. Nicolaas Kramer, and Dr. Andre Mkhoyan.

Chapter 3 describes our subsequent effort to increase n and σ and approach the IMT via photodoping. This chapter was published in *Nano Letters* under the title "ZnO Nanocrystal Networks Near the Insulator−Metal Transition: Tuning Contact Radius and Electron Density with Intense Pulsed Light". Unlike impurity doping, photodoping does not introduce impurity phases and typically has no deleterious effects on σ. To photodope ZnO NC networks we used intense pulsed light (IPL) annealing, in which samples are irradiated with a high-power Xe flashlamp. Applying IPL at a surface power density of 12 kW/cm^2, we were able to increase ρ in addition to n: ρ increased due to sintering while n increased due to photochemical removal of surface OH groups. Ellipsometry measurements of ρ and a LSPR fit based on Mie theory suggested that the maximum value of $n\rho^3$ attainable by this method was at least 0.7. At this value of $n\rho^3$, σ exceeded 10^1 Ω^{-1}cm^{-1}, and the dependence of σ on T suggested arrival at the critical region of the IMT, although truly metallic transport was not observed. Hence we concluded that $(n\rho^3)_c$ was in fact probably significantly greater than the predicted value of 0.3. This work was conducted in collaboration with Zachary Robinson, Dr. Konstantin Reich, Claudia Gorynski, Bryan Voigt, Dr. Lorraine Francis, and Dr. Boris Shklovskii.

In Chapter 4, we examine electron transport in ZnO NC networks with higher $n\rho^3$. Using ALD of ZnO to enlarge the interparticle necks, we increase ρ to values unobtainable by IPL-induced sintering. Then, using IPL to photodope and increase n as before, we raise σ to ~10^2 Ω^{-1}cm^{-1}, on par with the highest σ values obtained in bulk ZnO without impurity doping.[33] Concurrently we observe a complete IMT: σ becomes essentially independent of T throughout the measurement range (300K to ~50 mK). To our knowledge, this is the first unambiguous demonstration of a complete IMT driven by increasing $n\rho^3$ in a semiconductor NC network. Using a combination of Hall effect measurements and a modified approach to LSPR fitting, we refine our estimates of $n\rho^3$ and obtain further evidence that $(n\rho^3)_c$ is greater than 0.3. This motivates reevaluating the applicability of Equation 1.6. Moreover, at the critical point of the transition, the dependence of σ on T follows the unconventional power law $\sigma \sim T^{1/5}$, motivating further

theoretical studies of the critical behavior of NC networks. This work is an ongoing collaboration with Zachary Robinson, Yilikal Ayino, Jacob Held, Dr. Andre Mkhoyan, Dr. Vlad Pribiag, and Dr. Boris Shklovskii.

Having used the ZnO NC network as a platform for investigating NC doping and charge transport in Chapters 2, 3, and 4, we conclude by exploring the technological potential of these NCs in Chapter 5. We first show that ZnO NC networks can serve as scaffolds for deposition of TiN nanostructures by plasma-enhanced ALD (PEALD), resulting in plasmonic nanocomposites potentially applicable in hot-electron photodetection. We then measure the thermopower and thermal conductivity of variously treated ZnO NC networks and find that while they are unlikely to be used in high-efficiency thermoelectric generators, they show considerable potential to serve as transparent thermal insulation. Moreover, we demonstrate that visible light scattering can be substantially reduced by smoothing the films via hydraulic press compaction. Finally, we take preliminary steps toward eliminating the barriers to low-cost manufacturing of these ZnO NC networks. We demonstrate that high air-stable electrical conductivity is likely attainable without ALD and that scalable plasma synthesis of ZnO NCs may be possible at atmospheric synthesis pressure. Chad Beaudette, Claudia Gorynski, Jacob Held, and Gunnar Nelson made substantial contributions to the work presented in this chapter. The investigation of high-pressure synthesis was led by Dr. Narula Bilik and benefited from fluorescence measurements by Dr. Jihua Yang. An expanded version of Section 5.5 was published in *Journal of Applied Physics* under the title “Atmospheric-Pressure glow Plasma Synthesis of Plasmonic and Photoluminescent Zinc Oxide Nanocrystals”.

2. Aluminum doping in the plasma*

2.1 Introduction

In the past half decade, the colloidal synthesis community has developed an extensive library of doped metal oxide semiconductor nanocrystals (NCs) exhibiting tunable infrared (IR) localized surface plasmon resonances (LSPRs), including vacancy-doped tungsten oxide[21] and aliovalently doped oxides of indium,[22,42,43] cadmium,[24] titanium,[44] and zinc.[25,45,46] Near-IR applications include electrochromic sunlight management[47] and solar energy harvesting[48], and mid-IR applications include IR light-emitting diode efficiency enhancement[49] and surface-enhanced IR absorption spectroscopy[50]. Varying the dopant or vacancy concentrations in these materials modulates the free carrier concentration and thus the LSPR energy. Recently, a blueshift in LSPR energy has also been achieved via quantum confinement in sufficiently small photodoped ZnO NCs.[51]

Throughout the development of these materials, synthetic challenges have included finding molecules suitable for electronic passivation of surface defects, attaining high dopant activation fractions (fraction of dopant atoms serving as charge carrier donors), achieving uniform radial distribution of dopants within an NC, and simultaneously controlling doping level and NC size. Although substantial progress has been made in addressing these challenges in the liquid phase,[43,52–55] it has been difficult to simultaneously fulfill all of these requirements for diverse materials using a single synthesis technique. Nonthermal plasma synthesis is emerging as an alternative method for synthesizing materials inherently inaccessible by liquid phase routes, such as plasmonic P-doped Si.[26] However, until now the plasma synthesis approach has not been used for producing materials that are also accessible by colloidal synthesis, such as impurity-doped compound semiconductor NCs; exploring materials accessible by both colloidal and plasma synthesis allows comparison of the fundamental differences in dopant incorporation and activation mechanisms between these two methods. The

* Reproduced with permission from Greenberg, B. L.; Ganguly, S.; Held, J. T.; Kramer, N. J.; Mkhoyan, K. A.; Aydil, E. S.; Kortshagen, U. R. *Nano Lett.* **2015**, *15*, 8162. Copyright 2015 American Chemical Society.

nonthermal plasma approach is attractive not only as a novel chemical route, but also as a scalable, high-throughput, low-temperature process that, when integrated with inertial impaction deposition, is capable of producing high-performance nanocrystalline thin films suitable for myriad optoelectronic applications.[38]

Here we report nonthermal plasma synthesis of ligand-free, heavily Al-doped ZnO (AZO) NCs with high dopant activation fractions. Importantly, high doping levels are attained even within the cores of the NCs, a feat that has been difficult to achieve because dopants tend to segregate toward NC surfaces during colloidal synthesis. Doping of the cores is evinced by the high activation fractions, the lineshapes of the LSPR absorption features, and elemental maps produced by electron energy loss spectroscopy performed in a scanning transmission electron microscope (STEM-EELS). Moreover, we demonstrate that high *spatially averaged* doping levels (*i.e.* overall doping levels observable in ensemble measurements) can be maintained as NC size is reduced from 11.3 to 3.6 nm, which suggests high *local* doping levels not only beneath the outermost surface layers but deep within the cores, near the NC centers. Such dopant distributions enable simultaneous control of doping level and NC size, which we use to clearly experimentally demonstrate, for the first time, a quantum confinement effect on the LSPR energy of impurity-doped semiconductor NCs.

2.2 Results and discussion

In a typical synthesis, diethylzinc (DEZ) and trimethylaluminum (TMA) are injected into a low-pressure (5.6 Torr) radio-frequency Ar/O_2 plasma to form an aerosol containing AZO NCs. The aerosol accelerates through a rectangular slit orifice and the NCs, attaining supersonic velocities, deposit via inertial impaction onto a variety of substrates, forming nanocrystalline thin films at a deposition rate of 10 to 20 nm/s. Typical films are 500 ± 50 nm thick with 65 ± 5% porosity (ZnO volume fraction of ~35%). As deposited, the films have low free electron densities (n_e) due to hydroxyl groups on the NC surfaces acting as electron traps; we eliminate these traps by using atomic layer deposition (ALD) to infill the films with Al_2O_3, forming a ZnO/Al_2O_3 composite with a porosity of 10 ± 5%. A previous study of oxygen-vacancy-doped ZnO NCs[39] demonstrated that the ALD

infill removes surface OH groups and seals the NCs, resulting in air-stable conductive films with n_e sufficient to support LSPR at ~0.2 eV.

We control the Al doping level and thus the LSPR energy by varying the TMA concentration in the precursor feed gas. Increasing the TMA feed rate results in a linearly proportional rise of the Al concentration in the films ([Al]/[Zn+Al] atomic fraction, hereafter referred to as φ_{Al}) measured by inductively-coupled plasma mass spectroscopy (Figure S2.1 in the Supporting Information). STEM-EELS spectrum images (Figures 2.1a-c) indicate that Al atoms reside throughout the NCs including the NC cores, and that Al is not segregated to the NC surfaces; the apparent clusters of Al atoms that do reside on NC surfaces will be discussed later. As shown in Figure 2.1d, incrementing φ_{Al} from 0 to 3.2% results in an LSPR blueshift from ~0.2 to ~0.4 eV, indicating increasing incorporation of Al into the ZnO lattice and donation of its surplus valence electron to the conduction band[25]. The broadening of the LSPR feature indicates increased electron scattering[27], which is also consistent with Al incorporation[43]. Further evidence for electronically active Al is provided by UV-vis spectra which reveal optical bandgaps (E_g) blueshifted due to the Burstein-Moss effect[56] (see Figure S2.5 in the Supporting Information). We note that the increase in φ_{Al} is also accompanied by an incidental NC size reduction from 9.5 to ~7 nm (see Figure S2.4 in the Supporting Information), which, as discussed later, partially contributes to the LSPR blueshift, though minimally (<0.01 eV) in this size range.

Theoretical fits of the LSPR features in Figure 2.1d indicate high local doping levels in the NC cores, beneath the NC surface layers. To produce these fits we use Mie theory with the classical Drude dielectric function, assuming frequency-independent damping (for details, see ref. 39) and thus obtain estimates of the free electron densities (n_e) and intraparticle mobilities (μ_e). A representative comparison of this model and experimental data is shown in Figure 2.1e. For all φ_{Al}, such comparisons show good agreement at low energy but substantially underestimate the linewidth on the high-energy side. According to a recent study of tin-doped indium oxide (ITO) NCs,[43] this divergence at high energy indicates that damping is dominated by frequency-dependent ionized impurity scattering (in agreement with the LSPR peak broadening), which in turn suggests that dopants are

abundant in the NC cores as opposed to segregated to the surfaces, where they would not contribute strongly to damping. However, neglecting this frequency dependence introduces only a small error (~10%) to our estimates of n_e[43], which coincidentally cancels with that associated with neglecting particle-particle interactions.[57,58]

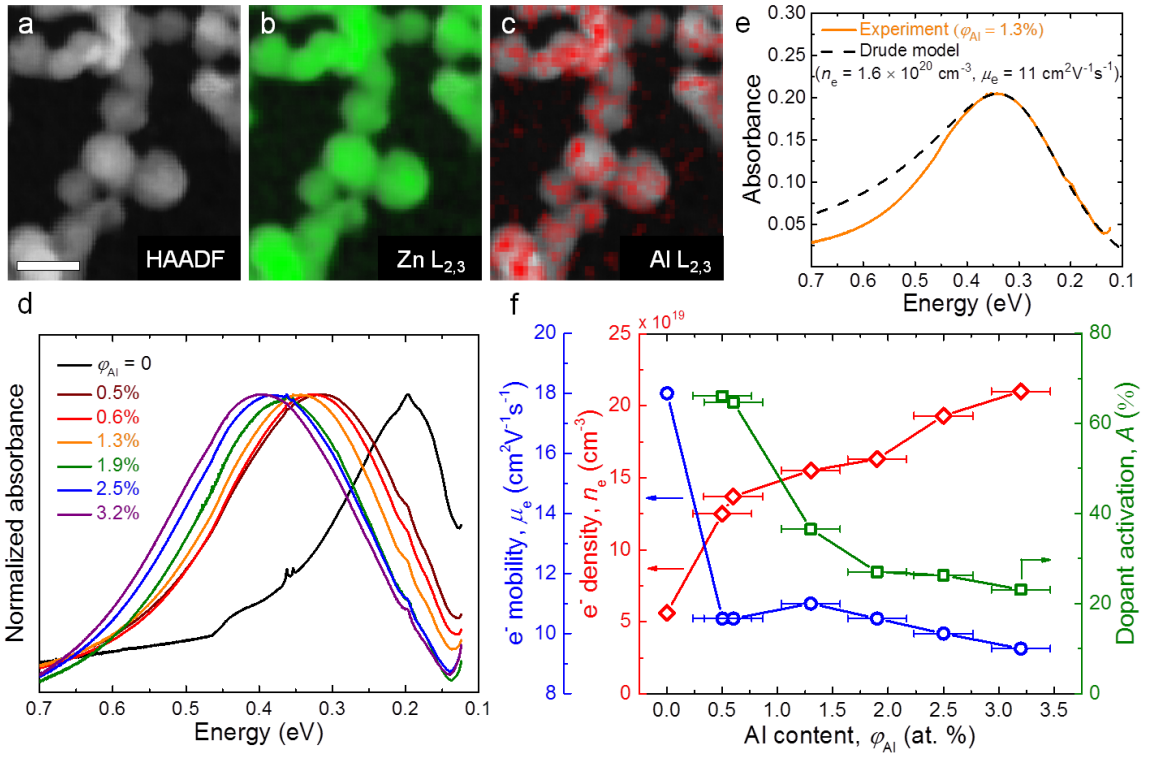

Figure 2.1: TEM and FTIR of AZO NCs. (a) HAADF-STEM image of AZO NCs with φ_{Al} = 1.3%. The scale bar is 10 nm (b–c) Spectrum images of Zn and Al $L_{2,3}$ edges overlayed on the HAADF-STEM image. HAADF-STEM and EELS maps are acquired simultaneously. (d) FTIR absorption spectra of NCs with φ_{Al} ranging from 0 to 3.2% and diameters between ~7 and 9.5 nm. (NC diameter gradually decreases from 9.5 to ~7 nm with increasing φ_{Al}). In this size range, both the broadening and the blueshift of the LSPR peak with increasing φ_{Al} are due primarily to Al doping – the former to decreased μ_e (ionized impurity scattering) and the latter to increased n_e. The strong dependence of linewidth (μ_e) on φ_{Al} is characteristic of high local doping levels in the NC cores. (e) A representative fit (dashed black line) of an LSPR absorption feature (solid orange line) using the Drude model and Mie theory. The discrepancy between model and experiment on the high energy side is also consistent with high local doping levels in the NC cores. (f) Electron densities, n_e (red diamonds), and electron mobilities, μ_e (blue circles), extracted from fits, and dopant activation fractions, A (green squares), calculated using Equation 2.1.

Additional evidence of high local doping levels in the NC cores is provided by the dopant activation fractions (A) – the number of additional free electrons per Al atom in the sample – which we calculate assuming constant oxygen vacancy concentration:

$$A(\varphi_{\mathrm{Al}}) = \frac{n_e(\varphi_{\mathrm{Al}}) - n_e(\varphi_{\mathrm{Al}} = 0)}{n_{\mathrm{Al}}(\varphi_{\mathrm{Al}})} \,. \tag{2.1}$$

In solution-synthesized NCs, *A* is often low; for example, in solution-synthesized ITO NCs, *A* values of 9-17% have been reported.[57] Recently, careful selection of In and Sn precursors based on relative reactivities has led to *A* values as high as 71%.[43] However, recent work by the same group on AZO NCs with φ_{Al} = 1.8 and 2.5% has resulted in *A* values of 2 and 5%, respectively; this significant inefficiency was attributed to segregation of Al atoms to the NC surfaces, where compensation by electron acceptors is more likely than donation to the conduction band.[45] In contrast, the plasma-synthesized AZO NCs reported here exhibit *A* greater than 20% for all φ_{Al} between 0.5 and 3.2%, with a maximum *A* of 66% for φ_{Al} = 0.5% (Figure 2.1f).

To further modulate the LSPR energy, NC size can be used as an additional handle, provided that heavy doping is maintained as NC size is reduced. Using photodoping to maintain a constant n_e of 1.4×10^{20} cm^{-3}, Schimpf *et al*. showed that reducing NC diameter from 12 to 3.5 nm blueshifted the LSPR energy from ~0.25 to ~0.5 eV, which they attributed to the coupling of collective plasmonic excitations to single-electron intraband transitions whose energies increase with quantum confinement.[51] A similar blueshift has been observed in metal (Ag) nanoparticles,[59–63] but to our knowledge, there are no reports of experimental demonstrations of this confinement effect in vacancy- or impurity-doped semiconductor NCs.

As mentioned previously, NC size is slightly reduced when φ_{Al} is increased. To explore a wider range of NC sizes and to resolve the effects of doping and size reduction on the LSPR energy, we introduce an independent handle on NC size: we vary the width of the rectangular slit orifice separating the synthesis and the deposition regions while maintaining constant precursor mass flow rates. Increasing the slit width reduces the gas pressure (from 14.5 to 0.9 Torr) as well as the residence time of the gas and the particles in the synthesis region (from ~50 to ~3 ms). These reductions in pressure and residence time decrease the total number of collisions between reactive species and NCs during synthesis and thus truncate NC growth. Using slit widths ranging from 0.5 to 3.5 mm, vacancy-doped (φ_{Al} = 0) NC size can be varied from 12.6 to 4.1 nm, and Al-doped (φ_{Al} =

1.3%) NC size can be varied from 11.3 to 3.6 nm (NC sizes determined from XRD peak width using the Scherrer formula, see Figure S2.2 in the Supporting Information). Film thickness and porosity, however, remain constant, and, as usual, we use ALD to infill the films with Al_2O_3 in order to remove and seal out electron-trapping OH groups.

Figure 2.2a displays the IR spectra of vacancy-doped (φ_{Al} = 0, doped only by oxygen vacancies) and Al-doped (φ_{Al} = 1.3% and oxygen vacancies presumably still present) NCs produced using four orifice widths, which reveal the effect of quantum confinement on the LSPR energy. For φ_{Al} = 0, as NC diameter is reduced from 12.6 to 4.1 nm, the LSPR energy blueshifts from 0.20 to 0.31 eV, and for φ_{Al} = 1.3%, as NC diameter is reduced from 11.3 to 3.6 nm, the LSPR energy blueshifts from 0.35 to 0.50 eV; in both cases, the blueshift is accompanied by line broadening. Both the blueshifts as well as the broadenings are similar in magnitude to those observed by Schimpf *et al*. for similarly-sized photodoped ZnO NCs[51].

Fitting a plot of LSPR energy vs. NC size (Figure 2.2b) confirms that the LSPR blueshifts are due to quantum confinement. Dependence of the LSPR energy on NC size can be described using a Lorentz oscillator model in which quantum confinement modifies both the driving and restoring forces[51,63]. For the purposes of this study, however, we favor an approach which has emerged from a recent density-functional-theoretic study that consolidates size dependences of the LSPR in an intuitive, albeit phenomenological, single formula. Specifically, Zhang *et al*.[64] used density functional theory to calculate the LSPR energies of 4-nm-diameter CdSe NCs and 5-nm CuS and CuSe NCs with free carrier (hole) densities ranging from 0 to ~10^{22} cm^{-3} and subsequently introduced a simple phenomenological formula for the LSPR energy of an NC of radius *r*:

$$\omega_{observed}{}^2 = \omega_{classical}{}^2 + \left(\frac{a\hbar^2}{m_e^* r^2}\right)^2 \tag{2.2}$$

where $\omega_{observed}$ is the observed LSPR energy, $\omega_{classical}$ is the corresponding material-dependent classical LSPR energy (observed for $r \rightarrow \infty$), m_e^* is the electron effective mass (overall inertial mass of an oscillating electron), and *a* is a proportionality constant. Using Equation 2.2 to fit the data in Figure 2.2b, we find *a* to be 3.8 and 4.4 for vacancy-

doped and Al-doped ZnO NCs, respectively, in good agreement with the value used to fit the theoretical CdSe data ($a \approx 4$). Using the classical Drude model to convert $\omega_{classical}$ to n_e, we obtain n_e values of 5.9×10^{19} and 1.7×10^{20} cm^{-3} for vacancy-doped and Al-doped ZnO NCs, respectively, and the Burstein-Moss shifts apparent in the corresponding ultraviolet-visible (UV-vis) spectra (Figure S2.2 in the Supporting Information) confirm that n_e is in fact consistently higher in the Al-doped NCs. Although we cannot completely rule out the possibility that, with decreasing NC size, n_e increases slightly and contributes to LSPR blueshifts, the good agreement of our data with Zhang's theoretical results as well as Schimpf's experimental results indicates that quantum confinement is the primary contributor.

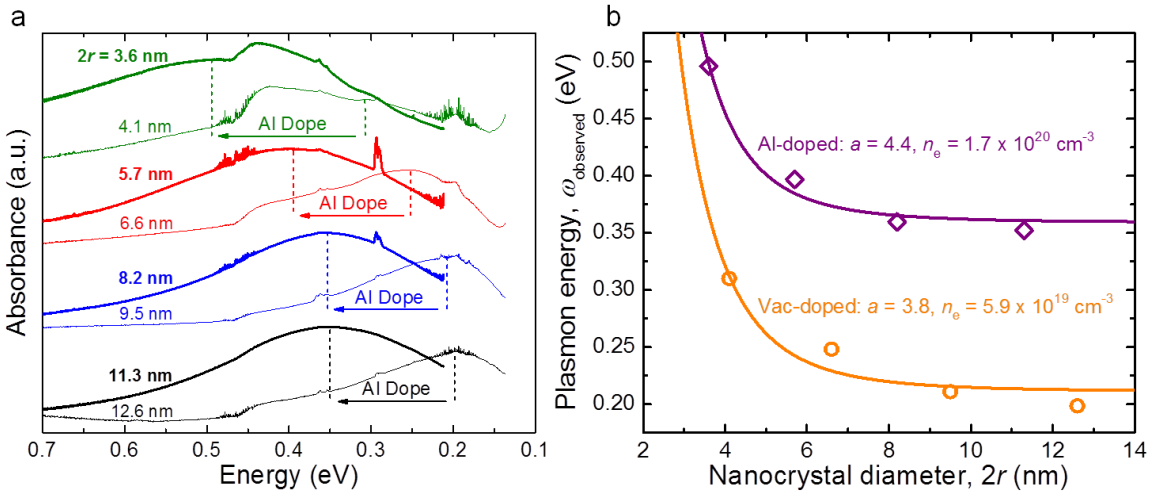

Figure 2.2: Effect of quantum confinement on the LSPR. (a) FTIR spectra of vacancy-doped NCs ($\varphi_{Al} = 0$) with diameters ranging from 12.6 to 4.1 nm (thin lines) and Al-doped NCs ($\varphi_{Al} = 1.3\%$) with diameters ranging from 11.3 to 3.6 nm (thick lines). Spectra are paired by slit orifice size used during synthesis (*e.g.*, the black spectra correspond to the largest NCs which were produced with the thinnest orifice), and for a given orifice size, Al-doped NCs are slightly smaller (*e.g.*, 11.3 vs. 12.6 nm) due to the incidental effect of Al doping on NC size. Comparing spectra of different colors, the blueshifts and broadenings of the LSPRs with decreasing NC size are due to quantum confinement. Comparing spectra of the same color, this size effect alone cannot account for the blueshifts, *i.e.* Al doping increases n_e. The absorption feature emerging around 0.44 eV indicates the presence of OH groups on the film surface. This vibrational feature becomes more pronounced as LSPR absorption diminishes and broadens with decreasing NC size. (b) LSPR energy vs. NC diameter for $\varphi_{Al} = 0$ (orange circles) and $\varphi_{Al} = 1.3\%$ (purple diamonds) with fits from equation 2.2.

These results are significant not only as an experimental demonstration of a quantum confinement effect on the LSPR energy of impurity-doped NCs, but also as evidence of effective impurity doping over a wide range of NC sizes. In fact, we suspect that the lack

of reports on this quantum confinement effect is due partially to difficulty, in colloidal synthesis, of attaining high doping levels in very small NCs. To our knowledge, the smallest previously reported AZO NCs exhibiting LSPRs were ~5 nm in diameter;[25] moreover, by tracking IR absorbance and elemental composition throughout NC growth, the authors of that study demonstrated that Al was initially excluded and that resulting NCs contained undoped cores ~2.7 nm in diameter. Our IR spectra of NCs of varied size suggest strongly that AZO NCs synthesized in the nonthermal plasma do not contain similar undoped cores. If they did, then as we decreased AZO NC radius from 11.3 to 3.6 nm, we would expect the volume fraction inaccessible to dopants to increase from ~9% to ~65% (assuming a 2.7-nm undoped core and that Al atoms on the surface are mostly electronically inactive, as discussed earlier), resulting in a drastic reduction in the spatially averaged doping level. However, we observe no such trend, which suggests that plasma-synthesized AZO NCs are doped uniformly: the local doping level is high not only beneath the outermost surface layers as discussed earlier, but also remains high deep within the cores, near the NC centers.

To explain the absence of undoped cores and the successful doping of small NCs, we propose a simple kinetic model of NC doping in the low-pressure nonthermal plasma. The proposed model is closely related to that proposed by Norris *et al*., [52,53] who argued that kinetics, rather than equilibrium thermodynamics, must be used to understand the mechanism of NC doping during colloidal synthesis. This argument is based on the observation that impurity diffusion rates within an NC are very low at typical growth temperatures, and consequently chemical equilibrium between the solid NC and surrounding liquid nutrient cannot be established. The same should be true in the nonthermal plasma provided that plasma power is low enough to maintain sufficiently low NC temperatures.[65] To test this hypothesis, we annealed a film of AZO NCs (φ_{Al} = 1.3%) under an Ar atmosphere at 625 ^{o}C for 1 hour, so that the diffusion length of Al in the ZnO lattice[66] was long compared to the NC radius. After annealing, the LSPR is redshifted to approximately the value typically observed for φ_{Al} = 0 (Figure S2.3 in the Supporting Information), indicating that the Al dopants are metastable and that the doped NCs are in fact the product of a non-equilibrium synthesis. Although the term “non-

equilibrium plasma" typically refers to the lack of thermal equilibrium among electrons, ions, and the neutral gas, evidently here it also describes the synthesis chemistry.

We consider, however, an important difference between colloidal synthesis and plasma synthesis in order to explain radial distributions of dopants in NCs: the former does not occur as far from chemical equilibrium as the latter. The nutrient species in colloidal synthesis are sufficiently stable in solution that the atomistic events leading to nucleation and growth are frequently reversed (dopant and host atoms may return to solution), so that there is a two-way exchange of atoms between the solution and the NC surfaces. Consequently, chemical potential differences between dopant and host atoms incorporated in NCs can significantly influence incorporation rates. Gamelin *et al*. have demonstrated that, since dopants incorporated in the NCs have higher chemical potential than the host atoms (*e.g.*, due to lattice strain[67]), host-atom incorporation can be heavily favored over dopant incorporation, particularly during nucleation and the early stages of growth, resulting in low local doping levels near the centers of solution-synthesized NCs[68–70]. In contrast, the active growth species in plasma synthesis are highly reactive gas-phase ions and radicals with such high chemical potentials that, at sufficiently low temperature, atomistic events leading to nucleation and growth are essentially irreversible (hence ~12-nm NCs can form in ~50 ms), and chemical potential differences between incorporated dopant and host atoms are irrelevant (figure 2.3a). Additionally, the irreversible NC growth in the plasma is facilitated by the distinctively high reactivities of ligand-free NC surfaces composed of under-coordinated atoms. The schematic in Figure 2.3b compares doping kinetics in the plasma and in solution: in the plasma, dopants are irreversibly incorporated throughout nucleation and growth. The resulting dopant distributions are radially uniform, so that doping level is high even if growth is truncated early.

Our model of non-equilibrium-plasma NC synthesis is supported also by the presence of a defect in the plasma-synthesized AZO NCs which is not observed in solution-synthesized AZO NCs. Extracting lattice parameters from XRD patterns of NCs with φ_{Al} ranging from 0 to 3.2%, we find that Al incorporation results in lattice expansion (Figure 2.4 and Figure S2.4 in the Supporting Information). In contrast, a similar study of

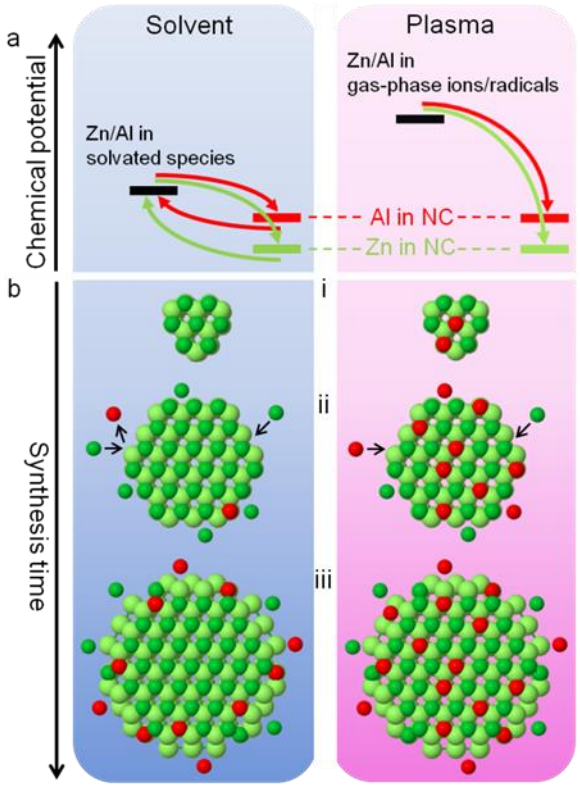

Figure 2.3: Schematic representations of AZO NC doping in a solvent and in the plasma. Zn, O, and Al atoms are dark green, light green, and red, respectively. (a) A key difference between these environments is that the solvated nutrient species in colloidal synthesis have much lower chemical potential than the gas-phase radicals and ions in plasma synthesis. Consequently, only in solution are atomistic events leading to nucleation and growth frequently reversed, and the higher chemical potential of dopants in NCs (dopants induce more lattice strain than host atoms) can translate to dopant exclusion. (b.i) During nucleation: in solution, doped nuclei, which are relatively unstable, succumb to solvation forces (*i.e.* critical nucleus size is larger for nuclei containing dopants); in the plasma, doped nuclei persist regardless of strain. (b.ii) During early growth: in solution, dopant incorporation is outcompeted by host-material incorporation; in the plasma, dopants are incorporated essentially whenever they collide with growing NCs. (b.iii) During late growth: in solution, substantial dopant incorporation finally occurs when competing host atoms are sufficiently depleted; in the plasma, dopant incorporation continues as in early growth.

solution-synthesized AZO NCs by Buonsanti *et al*. revealed lattice *contraction*. They attributed the contraction to the increasing population of substitutional Al: the ionic radii of Al and Zn are 0.53 Å and 0.74 Å, respectively.[25] This qualitative discrepancy indicates that our NCs contain a lattice-expanding defect much less prevalent in the solution-synthesized NCs, if not completely absent. We tentatively identify the defect as $Al_2^{3+}O_i^{2-}$, *i.e.* two adjacent substitutional Al cations complexed with an interstitial O anion, because its diamagnetism is consistent with electron paramagnetic resonance (EPR) spectra

(Figure S2.5 in the Supporting Information). This structure has been proposed to explain lattice expansion in AZO films synthesized by RF magnetron sputtering,[71] and its analog has been hypothesized to occur in sputtered Ga-doped ZnO.[72] The precise identity of this lattice-expanding defect, however, is not essential to our argument; in any case its abundance in our NCs serves as additional evidence of fundamentally different impurity incorporation kinetics.

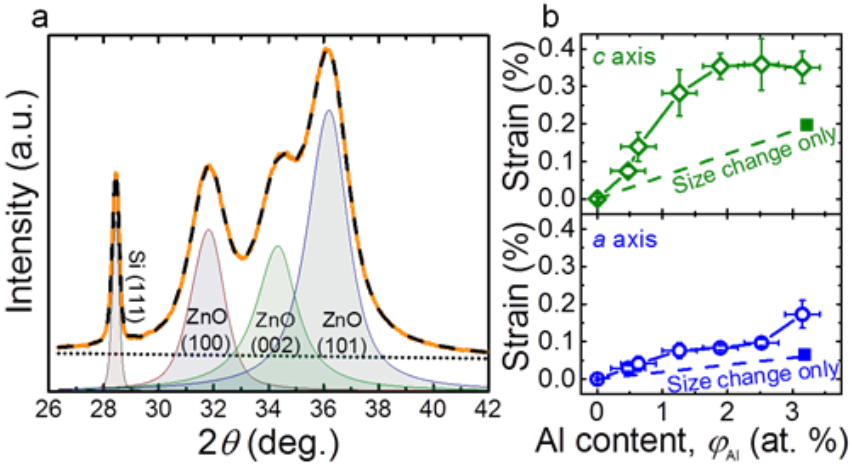

Figure 2.4: Evidence of lattice-expanding defect in the AZO NCs. (a) Representative XRD pattern (solid orange line, φ_{Al} = 0.6%) and overall fit (dashed black line) used to determine hexagonal lattice parameters *a* and *c*. The dotted black line is the linear background fit. Each AZO NC sample is mixed with microcrystalline Si powder to obtain a reference peak in the pattern, which is used to eliminate diffractometer alignment errors. (b) Lattice parameters *a* (blue circles) and *c* (green diamonds) extracted from fits of the ZnO (100), (002), (101), and (110) peaks plotted against φ_{Al}. To deconvolute the effects of doping and decreasing NC size (diameter shrinks from 9.5 to ~7 nm as φ_{Al} is increased from 0 to 3.2%), we also determined *a* and *c* of ZnO NCs with diameter similar to that of the smallest AZO NCs (6.6 nm) and found *a* and *c* strains to be merely ~0.06% and ~0.20%, respectively (represented by the solid squares). Thus we conclude that Al doping introduces a lattice-expanding defect.

Although the unique synthesis kinetics in the non-equilibrium plasma result in high local doping levels near the NC centers, a substantial portion of Al atoms do reside on NC surfaces, as indicated by STEM-EELS elemental maps. Electrical resistivity measurements and chemical etching experiments reveal that these Al atoms are oxidized. Following procedures described in ref. 39 (wherein only vacancy-doped ZnO was studied), we deposited films with φ_{Al} ranging from 0 to 3.2% on glass substrates, coated them with Al_2O_3 using ALD, and then deposited Al electrodes by thermal evaporation for four-point-probe current-voltage measurements. For φ_{Al} = 0, the resistivity is ~2 Ω cm,

similar to that reported in ref. 39, and much lower (more than eight orders of magnitude) than that typically measured in a film composed of NCs covered in insulating ligands.[73] However, as shown in Figure 2.5, resistivity increases by nearly an order of magnitude as φ_{Al} is increased to 3.2%. We hypothesized that this counterintuitive rise in resistivity upon increasing φ_{Al} is due to higher charge-transport resistance across NC-NC interfaces, and we attributed this increased resistance to oxidized surface-bound Al and/or Al_2O_3 clusters (see Figure 2.1c) formed on the NCs during synthesis. (While the Al_2O_3 grown on the NC surfaces using ALD *after* film deposition removes traps and reduces resistance, the Al_2O_3 formed *during* NC synthesis and pinched between adjacent NCs increases resistance.) To test this hypothesis, we introduced a selective chemical etching step between NC deposition and ALD coating: we soaked the films in a sodium carbonate/bicarbonate solution at pH 10 where ZnO is stable but Al_2O_3 dissolves. In an etched NC film (φ_{Al} = 1.9%), NC size (from XRD) was not reduced, but Al content (from energy dispersive X-ray spectroscopy) was reduced by ~40%, indicating that oxidized Al does reside on NC surfaces and is selectively removed by etching. Furthermore, in all etched films, resistivity is significantly lower (by a factor of three to seven) compared to that of unetched films, confirming our hypothesis. Indeed, even after etching, the highest resistance to charge transport in these films is still at the NC-NC boundaries. Using n_e and μ_e values extracted from IR measurements (Figure 2.1f), we estimate that the intraparticle resistivity is ~7×10^{-3} Ω cm for φ_{Al} = 0 and ~3×10^{-3} Ω cm for φ_{Al} = 3.2%, significantly lower than the film resistivities measured electrically (1-2 Ω cm). Thus, the initially counterintuitive rise in resistivity upon increasing φ_{Al} is not surprising: enhancement of the dominant resistance source (interparticle resistance) by Al_2O_3 pinched between NCs outweighs the resistance reduction due to doping.

Oxidation of dopant atoms prior to incorporation in NCs is an inherent competitive reaction path which must be addressed in further development of plasma synthesis of doped metal oxide NCs. The kinetic processes which enable the survival of doped nuclei also permit the persistence of small clusters of oxidized dopants. One approach to explore is downstream injection of additional dopant precursor to replenish the supply of unoxidized dopant atoms.

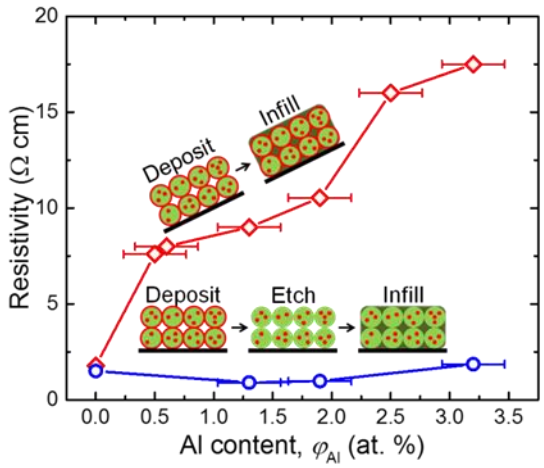

Figure 2.5: Electrical resistivity of films comprising AZO NCs vs. φ_{Al} with and without selective chemical etching to remove Al_2O_3 on NC surfaces. The increase in resistivity of films produced without an etching step (red diamonds) is attributed to Al_2O_3 formed during synthesis which can reside at particle-particle interfaces, forming an insulating barrier which impedes charge transport (unlike the Al_2O_3 from ALD which cannot form between intimately connected particles). Resistivities of films produced with an etching step (blue circles) are significantly lower than those of films that are not etched, but an improvement with doping is still lacking. This could be due to incomplete removal of Al_2O_3 or to a cancelling effect of the NC size reduction (9.5 to ~7 nm) accompanying doping (*e.g.*, more grain boundary scattering).

2.3 Conclusion

We have demonstrated that nonthermal plasma synthesis is a promising route toward addressing several challenges in doping metal oxide NCs. The key advantage of the plasma synthesis approach is the unique NC nucleation and growth kinetics which arise from irreversible interactions among highly reactive gas-phase ions and radicals and ligand-free NC surfaces. Exploiting these thoroughly non-equilibrium conditions, we have synthesized uniformly doped AZO NCs with high dopant activation fractions and high local doping levels in their central cores. Hence we have been able to maintain high doping levels while reducing NC size, experimentally demonstrating for the first time a quantum confinement effect on the LSPR energy in vacancy- and impurity-doped semiconductor NCs. We have also detected electronically inactive defects and surface-bound oxidized dopants, revealing challenges presented by plasma synthesis kinetics which should be considered as this synthesis approach is expanded to produce other doped metal oxide NCs and nanocrystalline thin films.

2.4 Experimental methods

AZO NC synthesis and deposition. A detailed description of ZnO NC synthesis and deposition accompanied by a schematic of the synthesis/deposition system is provided in ref. 39; to synthesize AZO NCs, TMA is injected into the same reactor port as DEZ. Briefly, in a typical synthesis, the DEZ and TMA are injected into an Ar/O_2 plasma (270 SCCM of Ar, 30 SCCM of O_2) in a cylindrical pyrex reaction chamber with a ~30-cm length and 0.75-in inner diameter. The DEZ and TMA are delivered as vapors via bubblers using Ar as the carrier gas. To control the DEZ and TMA feed rates, the carrier gas feed rates are held constant (20 SCCM through the DEZ bubbler and 3 SCCM through the TMA bubbler), and the bubbler pressures are controlled with metering valves: the DEZ bubbler pressure is held at 80 Torr while the TMA bubbler pressure is varied from 800 to 120 Torr to produce NCs with φ_{Al} ranging from 0.5 to 3.2%. The aerosol containing AZO NCs formed in the reaction chamber is accelerated through a rectangular slit orifice into a second chamber evacuated to 1.4×10^{-3} Torr using a Leybold Turbovac 1000c turbo pump. In this lower-pressure chamber, the NCs form a particle beam with thin rectangular cross section defined by the slit and deposit via inertial impaction onto various substrates (glass, Si, and NaCl) mounted to a pushrod, which linearly oscillates at a frequency of 1 Hz perpendicularly to the particle beam to produce rectangular thin films. A deposition time of 30 s produces films approximately 500 nm in thickness. To vary NC size, four different slit orifices are used: all are 15 mm long with widths ranging from 0.5 to 3.5 mm so that the pressure in the reaction chamber ranges from 14.5 to 0.9 Torr. The plasma is generated by applying a radio-frequency (13.56 MHz) voltage to a pair of copper ring electrodes encircling the Ar/O_2 injection port. A custom impedance matching network is used to attain a forward power of 100 W and a reflected power $\leq$ 2 W.

Atomic layer deposition. For FTIR, UV-vis, and electrical resistivity measurements, AZO NCs are coated in Al_2O_3 using a Cambridge Nanotech/Ultratech Savannah S200 ALD reactor. The ALD process is carried out at 180 ^oC and 0.5 Torr. One deposition cycle consists of four steps: (1) a 0.1-s H_2O pulse, (2) a 30-s nitrogen purge, (3) 0.1-s

TMA pulse, and (4) a 30-s nitrogen purge; 70 cycles are completed for a 7.7-nm coating. Prior to these cycles, the AZO NCs are allowed to outgas for 2,000 s under 20-SCCM nitrogen flow.

Spectroscopy. Film thicknesses and porosities are determined from spectroscopic ellipsometry: AZO NCs are deposited onto Si wafers and measured using a J.A. Woolam M44 spectrometer, and spectra between 450 and 750 nm are fitted using the Bruggeman effective medium approximation. Unless otherwise stated, films characterized in this work are 500 ± 50 nm thick with 65 ± 5% porosity (ZnO volume fractions of ~35%). For FTIR spectroscopy, AZO NCs are deposited onto IR-transparent polished NaCl plates and coated with 7.7 nm of Al_2O_3 by ALD, and measurements are performed using a Bruker Alpha IR spectrometer in transmission mode. The AZO NC films are exposed to air both before and after ALD, but measurements are performed under a nitrogen atmosphere. For large NCs (diameter ≥ 7 nm), LSPR absorption features are fitted using Mie theory with the classical Drude dielectric function, assuming frequency-independent damping (for details, see ref. 39). For UV-vis spectroscopy, AZO NCs are deposited onto Corning Eagle XG glass substrates and coated with 7.7 nm of Al_2O_3 by ALD (unless stated otherwise) and then measured in air using an Agilent Cary 5000 spectrophotometer in transmission mode. Bandgaps are determined from Tauc plots for a direct bandgap semiconductor ($(\alpha h\nu)^2$ vs. $h\nu$). For EPR spectroscopy, thick (~3 μm) AZO NC films are deposited onto Si wafers and then scraped into suprasil quartz tubes. Measurements are performed in air using a a Bruker Continuous Wave Elexsys E500 EPR spectrometer. For inductively coupled plasma mass spectroscopy, thick (~3 μm) AZO NC films are deposited onto Si wafers and then digested in nitric acid. A Yittrium internal standard is added (40 ppb), and then the solution is analyzed using a Thermo Scientific XSERIES 2 ICP-MS equipped with an ESI PC3 Peltier-cooled spray chamber, SC-FAST injection loop, and SC-4 autosampler. All measurements are performed in standard mode (no collision gas).

X-ray diffraction. XRD measurements are performed using a Bruker D8 Discover diffractometer equipped with a beryllium area detector (angular resolution = 0.02°) and a

cobalt Kα source; the collected patterns are mathematically converted to copper-Kα patterns. For typical XRD measurements used to determine NC size, AZO NCs are directly deposited by inertial impaction onto Si wafers and not coated by ALD. Average NC sizes are calculated using the Scherrer equation, assuming spherical particles.[74] For more precise XRD measurements used to determine lattice parameters, a mixture of AZO NCs and microcrystalline Si powder (~10% Si by mass) is sonicated in ethanol and then dropcast onto Si wafers; the resulting Si (111) peak in the diffraction pattern is used as a reference to correct for alignment discrepancies. Lattice parameters are determined as follows. First, each sample is measured three times with the X-ray beam probing a different portion of the sample each time to minimize the influence of any spatial inhomogeneities in the AZO/Si mixture. Then XRD patterns are fitted with pseudo-Voigt profiles using MDI Jade. The best fits are achieved by splitting each pattern in two and using a linear background for the low-angle half ($<42^{o}$) and a parabolic background for the high-angle half. The fits are linearly shifted so that all Si (111) peaks align. Using these aligned fits, the hexagonal lattice parameter *a* is extracted from the locations of the ZnO (100) and (110) peaks, and then this *a* value is used in conjunction with the locations of the ZnO (002) and (101) peaks to determine the lattice parameter *c*. The ZnO (102) peak is neglected due to its strong overlap with the Si (220) peak. For each sample, the reported *a* and *c* values are averages of the triplicate measurements, and the error bars represent the standard deviations. For lattice spacings up to 3.2 Å, the beryllium area detector's angular resolution (0.02^{o}) translates to uncertainties up to ±0.0009 Å, or ±0.03% in strain units. Error bars exceeding this magnitude are likely due to residual random alignment errors.

Transmission electron microscopy. AZO NCs are deposited by inertial impaction directly onto carbon-coated gold TEM grids (ultrathin carbon / holey support). STEM-EELS data are acquired on an aberration-corrected FEI Titan G2 60-300 (S)TEM equipped with a Gatan Enfinium ER EEL spectrometer, operating at 60 keV, 30 mrad convergence angle, 75 pA beam current, and a 25.9 mrad EELS aperture. Spectrum images are acquired by scanning the beam across clusters of NCs with ~7 Å steps with a

60 ms pixel dwell time in a 60 x 60 pixel grid while simultaneously collecting HAADF signal and EEL spectra at 15-527 eV (Al L-edge), and 700-1212 eV (Zn L-edge) with an energy dispersion of 0.25 eV. To mitigate damage to the specimen, 64 x 64 sub-pixel scanning is implemented to evenly distribute the dose over the NCs. Background signals are subtracted using a power-law fitting function. The Al $L_{2,3}$ (72-88 eV, avoiding the Zn M edge at 88 eV) and Zn $L_{2,3}$ (1020-1212 eV) edges at each pixel are integrated for each pixel and a 3 pixel Gaussian blur is applied to the final spectrum images to reduce noise. For verification of NC sizes, lower-resolution micrographs are obtained using an FEI Tecnai T12 TEM.

Electrical resistivity measurements and selective etching of oxidized Al. AZO NCs are deposited onto 1×1-cm Corning Eagle XG glass substrates and coated with 7.7 nm of Al_2O_3 by ALD. For four-point measurements, four parallel 500-nm-thick Al line electrodes are deposited onto the film by thermal evaporation with a spacing of 2 mm between adjacent lines. Using a Janis Research Cryomicroprobe Station connected to an Agilent 4155C semiconductor parameter analyzer, current is controlled between the outer electrodes and voltage is measured between the inner electrodes. These measurements are performed in air at room temperature. To remove oxidized Al residing on NC surfaces, chemical etching is performed between NC deposition and ALD coating. Films are soaked in a sodium carbonate/bicarbonate solution at pH 10 for 1 hour and then dried in air at 100 ^{o}C .

2.5 Acknowledgements

This work was supported primarily by the National Science Foundation through the University of Minnesota MRSEC under Award Number DMR-1420013 and partially by BASF Corporation. Parts of this work were carried out in the College of Science and Engineering Characterization Facility, University of Minnesota, which has received capital equipment funding from the NSF through the UMN MRSEC program under Award Number DMR-1420013. Parts of this work were carried out in the College of Science and Engineering Minnesota Nanocenter, University of Minnesota, which

receives partial support from the NSF through the NNIN program. We thank Rick Knurr for ICP-MS measurements. We thank Dr. Javier Garcia Barriocanal, Professor Alexander Govorov, Professor Michael Manno, and Professor Elijah Thimsen for valuable discussions.

3. Photodoping and photonic sintering: approaching the insulator-metal transition*

3.1 Introduction

Understanding and controlling charge transport across semiconductor nanocrystal (NC) networks has enabled NC-based devices such as solar cells,[75,76] thermoelectric generators,[77,78] and field-effect transistors.[6,79] The NCs are typically covered with and separated by ligands, whose composition and length can be varied to tune carrier mobility across several orders of magnitude.[7–9] Alternatively, NCs have been brought into direct contact by removing these ligands[10,12,13,80] or by using gas-phase synthesis and deposition,[37,38,81,82] and mobility has been tuned by varying the interparticle contact area.[10,12,81,83] Elimination of ligands promises particularly high mobility, and envisioned applications of this approach prompt a fundamental question: what are the necessary conditions for metallic transport?

An insulator-metal transition (IMT) criterion for direct-contact NC networks (DCNNs),

$$(n\rho^3)_c \approx 0.3g, \tag{1.6}$$

was proposed,[18] where (for an n-type semiconductor) n is the free electron density, ρ is the contact radius between adjacent NCs, and g is the degeneracy of the conduction band minima (for ZnO, g = 1). This derives from the requirement at the IMT that the interparticle contact conductance, G_i, is equal to the quantum conductance, $e^2/\pi\hbar$,[84,85] which is satisfied when the free electron Fermi wavelength, $k_F^{-1} = (g/3\pi^2 n)^{1/3}$, is comparable to ρ. As shown in Figure 3.1a, when $\rho \approx 1$ nm, Equation 1.6 predicts that the critical value of n is on the order of 10^{20} cm^{-3}, which for 10-nm-diameter NCs corresponds to ~50 free electrons per NC. Hence seven electron shells are occupied and $\epsilon_F = \hbar^2 k_F^2/2m^*$ is a good approximation of the highest occupied shell energy.[18]

Experimental efforts to achieve metallic transport in DCNNs and to verify Equation 1.6 have yielded promising yet inconclusive results. Chen *et al.*[18] measured the

* Reproduced with permission from Greenberg, B. L.; Robinson, Z. L.; Reich, K. V; Gorynski, C.; Voigt, B. N.; Francis, L. F.; Shklovskii, B. I.; Aydil, E. S.; Kortshagen, U. R. *Nano Lett.* **2017**, *17*, 4634. Copyright 2017 American Chemical Society.

conductivity of thin films of plasma-synthesized P-doped Si NCs. Increasing n so that so that $n\rho^3$ reached approximately half the predicted critical value resulted in electron localization length, ξ, greater than the NC diameter, d, as expected near the IMT. More recently, higher $n\rho^3$ values were achieved in networks of plasma-synthesized ZnO NCs.[81] While n was held constant, ρ was increased via atomic layer deposition (ALD) of additional ZnO onto the NC surfaces, yielding $n\rho^3$ greater than the predicted critical value. Some evidence of an IMT was given: the most conductive sample exhibited $\xi > d$, $G_i > e^2/\pi\hbar$, and n independent of temperature down to 100 K. The temperature coefficient of conductivity, however, remained positive, and n was not measured below 100 K.

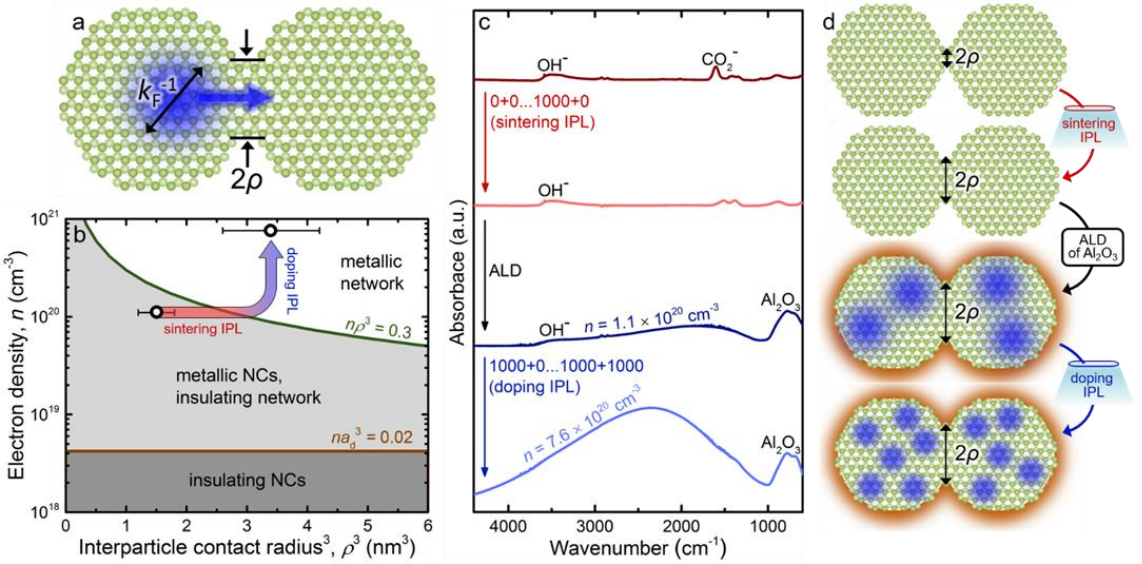

Figure 3.1: IMTs and IPL-based treatment strategy. (a) Schematic of two NCs with contact radius ρ and Fermi wavelength k_F^{-1}. Equation 1.6 derives from the expectation that metallic charge transport occurs for $\rho > 2k_F^{-1}$. (b) Theoretical charge transport phase diagram of a ZnO NC network. The brown line represents the Mott criterion for the bulk IMT, where $a_d \approx 1.5$ nm is the donor Bohr radius in ZnO,[86] and the green line represents the criterion for the NC network IMT (Equation 1.6). The data points and arrow illustrate the path taken in this work, which ends in the region where metallic transport is expected. (c) FTIR absorption spectra of ZnO NC networks at various treatment stages. Sequentially, the NCs are deposited (dark red), sintered by IPL (light red), coated with Al_2O_3 by ALD (dark blue), and finally photodoped by IPL (light blue). The spectra shown here correspond to maximally treated samples (1000 flashes each of sintering and doping IPL). Sample names are of the form "x+y", where x is the number of sintering IPL flashes and y is the number of doping IPL flashes. (d) Corresponding schematics of treatment stages. Sintering IPL removes surface carboxylates and increases ρ; then ALD removes surface hydroxyls, thereby freeing electrons (while further increasing ρ); then doping IPL removes remaining hydroxyls, thereby increasing n and decreasing k_F^{-1}.

These results reveal a need for further study of not only the applicability of Equation 1.6 but also of the critical behavior of electrical properties near the IMT in DCNNs. Proximity to the IMT has been difficult to evaluate, because knowledge of the signals of the transition in DCNNs has been relatively limited. For bulk semiconductors, it is well known that the IMT is often a continuous quantum phase transition with a critical region in which conductivity attains a power-law dependence on temperature, and ξ and the dielectric constant, ε, diverge as powers of the tuning parameter that drives the transition.[87–89] To our knowledge, for DCNNs, such a transition has not been demonstrated and such dependencies have not been established.

In this work we test Equation 1.6 and examine in detail the near-IMT transport behavior of DCNNs by taking a new approach to manipulating $n\rho^3$. We develop a technique for independently tuning both ρ and n in a ZnO DCNN while maintaining constant d and network composition, so that we can isolate the dependencies of electrical properties on $n\rho^3$ throughout the critical range. This approach is distinct from impurity doping, which introduces impurity phases that may impede transport,[18,90] and from the ZnO ALD method which significantly increases d and ZnO volume fraction in addition to ρ. The ability to modulate both ρ and n without changing d is useful not only for this study but also for pursuing the goal of "confined but connected" NCs which promise wide tunability of optical as well as electrical properties.[13,80] Our technique is based on xenon-flashlamp intense pulsed light annealing (IPL), which has the additional advantages of roll-to-roll processing compatibility and applicability to a wide variety of materials,[91–95] including ZnO.[96,97] Applying IPL to a ZnO DCNN with d = 10 nm, we increase ρ from 1.1 to 1.5 nm (ρ^3 from 1.5 to 3.4 nm^3) and then increase n from 1.1 to 7.6 $\times$ 10^{20} cm^{-3} in order to tune $n\rho^3$ from 0.17 to 2.6, according to estimates of ρ and n based on ellipsometry and Fourier Transform infrared (FTIR) spectroscopy, respectively. For large $n\rho^3$, the dependence of conductivity on temperature transitions from a stretched exponential form to a power law, which suggests that the IMT critical point, $(n\rho^3)_c$, lies near the top of our measured range. Indeed, assuming $n\rho^3_c \approx 2.6$, we find that for $n\rho^3$ near $(n\rho^3)_c$, both ξ and ε diverge as $[(n\rho^3)_c - n\rho^3]^{-1}$, and conductivity exhibits scaling behavior consistent with arrival at the critical region of a continuous quantum phase transition.

These results provide clear measures of proximity to the IMT, and they suggest that for nonideal DCNNs such as ours and those studied by Chen *et al.*[18] and Lanigan and Thimsen[81], the criteria for crossing to the metallic side may in fact be more stringent than Equation 1.6.

3.1 Results and discussion

We produce ZnO DCNNs by nonthermal plasma synthesis integrated with inertial impact deposition, as described previously.[82] Briefly, diethylzinc and oxygen gas are injected into a low-pressure (5 Torr) radio-frequency argon plasma to form ZnO NCs with d = 10 nm. At the outlet of the plasma chamber, the NCs pass through a slit orifice and enter a lower-pressure (10 mTorr) deposition chamber, forming a two-dimensional supersonic particle beam. We translate substrates perpendicularly to the beam to create 1 × 1 cm ZnO DCNN films with thickness, t, of 300 ± 20 nm and ZnO volume fraction, ϕ, of 33 ± 2 %. The NCs in these films are ligand-free and in direct contact, and their surfaces are terminated in hydroxyl and carboxylate groups. The hydroxyl groups are electron traps, so we remove them by infilling the films' pores with Al_2O_3 by ALD,[82] which yields air-stable n on the order of 10^{20} cm^{-3} (see Note 3.2 in the Supporting Information for further discussion). The NCs are not intentionally doped, and the high n is likely due to oxygen vacancies,[98,99] although we cannot rule out other donors such as hydrogen[100] and interstitial zinc.[101]

To develop a strategy for independently tuning ρ and n while maintaining constant d and network composition, we consider the following. First, we can target ρ by encouraging the NC network to enter – but not surpass – the initial stage of sintering. During this initial stage, grains minimize surface energy by forming necks, but otherwise grains retain their shape, and substantial grain growth does not occur[102–104] (see Figure S3.1 in the Supporting Information). This can be accomplished by adding an annealing step before the ALD infilling which thermally activates solid state diffusion of NC atoms toward the interparticle contacts. Then, to modulate n, we can manipulate the composition of the film after ALD. Specifically, we can exploit the fact that after the NC network is infilled with Al_2O_3, the film still contains some electron-trapping hydroxyl

groups due to incomplete removal and/or introduction of new hydroxyls during the ALD process.[105] Reducing the concentration of these residual traps should increase *n*.

We realize this strategy by introducing IPL both before and after the ALD step. In both cases, we apply IPL under ambient conditions at a surface power density of 12 kW/cm^2 with a 660 ms period and a 1 ms flash duration. The ZnO NCs strongly absorb the UV portion of the xenon flashlamp spectrum. In general, absorption of a UV photon with energy greater than the band gap of ZnO (3.3–3.4 eV) alters the surface chemistry of ZnO by a two-step process: the photon generates an electron-hole pair, and then the hole oxidizes an electronegative and/or negatively charged surface species, resulting in desorption.[96,106–108] The remaining photogenerated electron can persist as a free charge carrier or it can be trapped upon readsorption of the desorbed species or adsorption of another oxidant. When we apply IPL before ALD, these processes induce sintering: electron and hole relaxation to the band edges and non-radiative electron-hole recombination supply thermal energy, and photochemical removal of stabilizing surface species facilitates formation of new Zn-O bonds. We will show shortly that removal of surface carboxylates is particularly important. However, while ρ increases, *n* remains constant due to adsorption of ambient gases. In contrast, when we apply IPL after ALD, the Al_2O_3 infill suppresses sintering so that ρ remains constant. Meanwhile hydroxyl groups are removed, and the Al_2O_3 infill protects the photogenerated electrons from oxidizing gases so that *n* increases.

Figures 3.1b, 3.1c, and 3.1d show our treatment sequence and summarize its effects on ρ, *n*, and NC surface chemistry. We combine IPL before ALD ("sintering IPL") and IPL after ALD ("doping IPL") to produce two data series: (1) a sintering series (varied ρ, constant *n*) in which the number of sintering IPL flashes is varied from 0 to 1000 and (2) a doping series (varied *n*, constant ρ) in which all samples are pretreated with 1000 flashes of sintering IPL, and then the number of doping IPL flashes is varied from 1 to 1000. Sample names are of the form "*x* + *y*", where *x* is the number of sintering IPL flashes, and *y* is the number of doping IPL flashes. Neither sintering IPL nor doping IPL significantly alters *d* or film microstructure, as indicated by X-ray diffraction (XRD)

patterns and scanning electron micrographs (SEM) (Figure S3.2 in the Supporting Information).

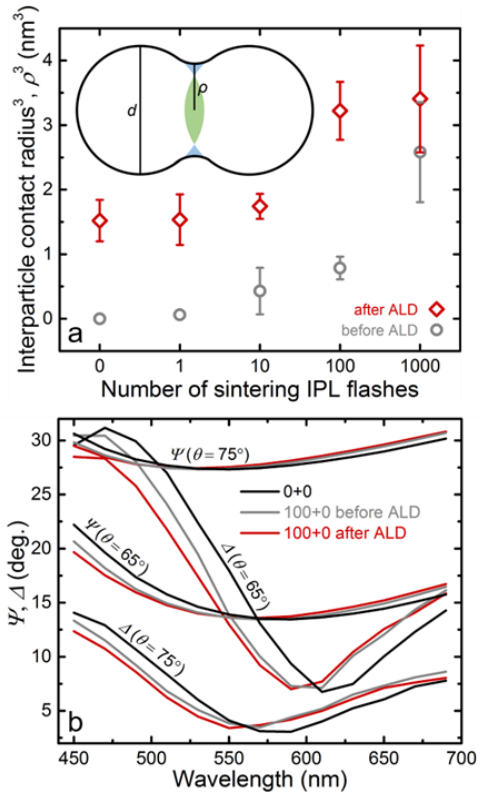

Figure 3.2: Evolution of ρ with sintering IPL. (a) ρ calculated using the geometrical model described in Note 3.1 in the Supporting Information. Error bars represent the 95% confidence intervals based on ellipsometry precision (see Figure S3.3 in the Supporting Information). The "after ALD" values (red diamonds) are obtained by thermally annealing the samples after IPL to simulate the additional sintering that occurs during ALD. Since conductivity measurements are conducted after ALD, all ρ values reported and used in this work are the "after ALD" values, unless specified otherwise. (b) Representative ellipsometry data used to determine ZnO volume fraction, ϕ, which is the primary input in the geometrical model used to calculate ρ. Θ is the angle of incidence. Ψ and Δ are measured before any treatment (black), then after sintering IPL (in this case 100 flashes, gray), and then after thermal annealing to simulate ALD (red).

Figure 3.2a shows the increase in ρ^3 with the number of sintering IPL flashes. To detect changes in ρ we measure film thickness, t, and ZnO volume fraction, ϕ, by spectroscopic ellipsometry, using the Bruggeman effective medium approximation. We perform the measurements before ALD, so that there is no Al_2O_3 coating and no significant contribution of free electrons to the dielectric function ($n \approx 0$). This approach was applied to similar ZnO NC networks previously and was shown to yield t and ϕ values in good agreement with scanning electron microscopy and Rutherford

backscattering data.[82] Representative spectra are shown in Figure 3.2b, and a representative fit and complete plots of t and ϕ are shown in Figure S3.3 in the Supporting Information. During sintering, the ZnO NC film slightly shrinks and densifies: 1000 flashes of sintering IPL decreases t by ~6% and increases ϕ by ~6%. These modest changes are consistent with remaining in the initial stage of sintering rather than proceeding to the intermediate stage (characterized by more substantial densification and changes in grain morphology).[104] We convert changes in ϕ to changes in ρ using a simple geometrical model described in Note 3.1 in the Supporting Information. In this model, we treat ρ as homogeneous throughout the network, and we must make an assumption about the starting value of ρ in an unsintered network, ρ_0. We assume $\rho_0 = 0$. In reality, an unsintered network likely contains a mix of interfacial and point contacts, so that our model may lead to conservative estimates of ρ. However, we expect sintering to improve the accuracy of the homogeneity assumption, because surface area minimization should entail reduction of ρ dispersion.

Since all conductivity measurements are performed after the ALD infilling step, it is important to estimate ρ after ALD. The ALD temperature is 180 °C, so some additional sintering may occur, increasing the final value of ρ. Figure 3.2b shows ρ^3 both before and after ALD. To obtain ρ before ALD, we conduct ellipsometry measurements immediately after sintering IPL, and we find that ρ^3 increases from 0 to 2.6 ± 0.8 nm^3 as we increase the number of sintering IPL flashes from 0 to 1000. Then, to obtain ρ after ALD, we heat the samples under N_2 at 180 °C for 33 minutes in order to mimic the temperature history of ALD-treated samples without actually depositing Al_2O_3, since an Al_2O_3 infill would compromise ellipsometry data fitting. This heating does in fact induce additional sintering (without grain growth) and reveals that ρ after ALD is approximately 0.8 to 1.5 nm larger than ρ before ALD: after heating, ρ^3 ranges from 1.5 ± 0.3 nm^3 (0 sintering IPL flashes) to 3.4 ± 0.8 nm^3 (1000 sintering IPL flashes). We use these post-ALD ρ^3 estimates to determine $n\rho^3$.

Post-ALD ρ appears to depend on carboxylate removal during sintering IPL, which is evident in the Fourier transform infrared (FTIR) spectra (Figure 3.3a). The absorption feature at 1600 cm^{-1}, which we attribute to surface carboxylates,[109–112] vanishes as we

increase the number of sintering IPL flashes. This removal of carboxylates is likely due to oxidation by UV-photogenerated holes, as illustrated in Figure 3.3a. The importance of carboxylate removal was revealed by a control experiment: with a low-intensity Xe lamp, we illuminated a sample with a total photon dose equivalent to 100 flashes of sintering IPL but at a much lower fluence, so that carboxylate removal was the only observed effect and no sintering occurred during illumination (see Figure S3.4 in the Supporting Information). We found that pre-ALD ρ^3 was unchanged, but that post-ALD ρ^3 was higher than that of a non-illuminated sample and equal to (within 3% of) that of a sample treated with 100 flashes of sintering IPL. (Also, the same was true of electrical conductivity.) This surprising result suggests that carboxylate removal is in fact the most important effect of sintering IPL, because it determines the degree of additional sintering during ALD and thus the final value of ρ^3. A more detailed explanation of the role of carboxylates in sintering is proposed in Figure S3.5 in the Supporting Information.

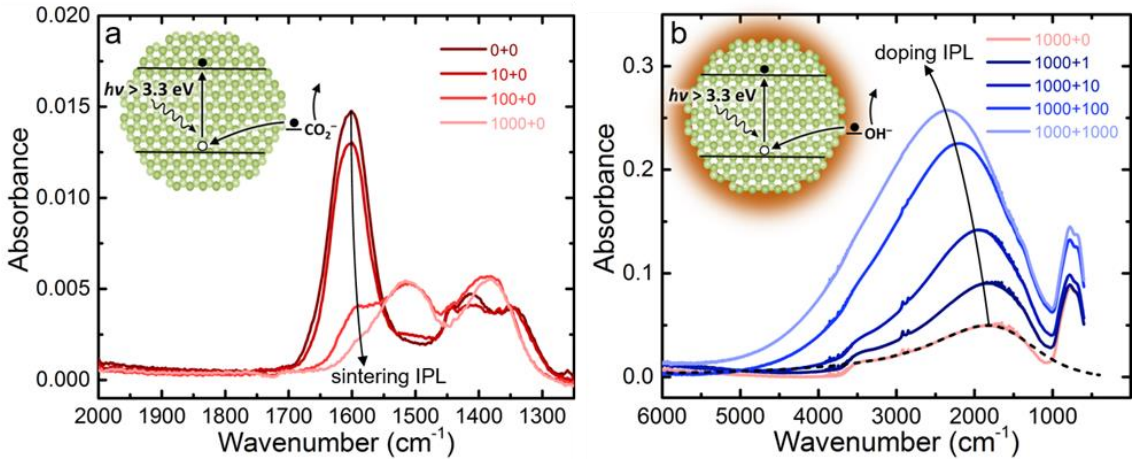

Figure 3.3: FTIR absorption spectra evolution with IPL dose. Sample names are of the form "*x*+*y*", where *x* is the number of sintering IPL flashes and *y* is the number of doping IPL flashes. (a) Sintering series: spectra after sintering IPL, collected before ALD. Surface carboxylates (1600 cm^{-1}) desorb after oxidization by photogenerated holes, which likely facilitates the increase in ρ. (b) Doping series: spectra after 1000 flashes of sintering IPL plus flashes of doping IPL, collected after ALD. Hydroxyl groups (~3500 cm^{-1}) are removed via oxidation by photogenerated holes, and *n* increases from 1.1 to 7.6 × 10^{20} cm^{-3}. The broad feature that intensifies and blueshifts from ~1800 to ~2400 cm^{-1} is due to the LSPR. The dashed black line shows the fit of the "1000+0" spectrum from Equation 3.2.

Figure 3.3b shows the FTIR spectra of the doping series (acquired after ALD), which reveal hydroxyl removal and the resultant increase in *n*. The absorption feature at ~3500

cm^{-1} that vanishes with doping IPL is due to hydroxyl groups.[82,113] As mentioned earlier, hydroxyls may be present on the ZnO NC surfaces due to incomplete removal by ALD, or they may be introduced during ALD. A hydroxyl originating from ALD and residing in the Al_2O_3 is likely to act as a trap if its distance from an NC surface is less than the decay length of the electron wavefunction in Al_2O_3. As shown in the schematic in Figure 3.3b, we attribute removal of hydroxyls on or near the ZnO NC surfaces to oxidation by photogenerated holes (see figure S3.4 and Note 3.2 in the Supporting Information for additional data and discussion). The broad and intense absorption features centered near ~2000 cm^{-1} in Figure 3.3b are due to localized surface plasmon resonance (LSPR). That they blueshift and intensify with doping IPL confirms that hydroxyl removal is accompanied by rising *n*.

We quantify *n* by fitting the LSPR absorption features. We favor this approach over Hall effect measurements (see Figure S3.6 in the Supporting Information), which produce results that are difficult to interpret in a consistent manner for a diverse set of samples exhibiting hopping conduction[114,115] and approaching the IMT. Beginning with the last sample of the sintering series, "1000+0" (1000 sintering IPL flashes, 0 doping IPL flashes), we estimate the film's dielectric function using the Maxwell Garnett effective medium approximation (MG EMA). The MG EMA, which does not account for interparticle conduction, has previously been shown to produce good fits of high-*n* films of In_2O_3:Sn NCs exhibiting hopping transport, and has been found to outperform the Bruggeman EMA[116] (whereas the Bruggeman EMA was shown to produce accurate fits of ellipsometry data from films of ZnO NCs with $n \approx 0$,[82] in which the dielectric function is determined by bound electrons). In the MG EMA, the overall effective dielectric function of the film, ε, is given by

$$\frac{\varepsilon - \varepsilon_m}{\varepsilon + 2\varepsilon_m} = \phi \frac{\varepsilon_{NC}(\omega) - \varepsilon_m}{\varepsilon_{NC}(\omega) + 2\varepsilon_m}, \tag{3.1}$$

where ϕ is the NC volume fraction, ε_m is the dielectric constant of the medium in which the NCs are embedded (Al_2O_3, ε_m = 2.6 at high frequency[117]), and $\varepsilon_{NC}(\omega)$ is the frequency-dependent dielectric function of the NCs given by the Drude equation, $\varepsilon_{NC}(\omega) = \varepsilon_\infty - \omega_p^2/(\omega^2 + i\omega\Gamma)$, where ε_∞ is the high-frequency dielectric constant (3.7 for ZnO[117]),

Γ is the carrier relaxation frequency, and ω_p is the plasma frequency. We approximate Γ as a constant $\Gamma = e/\mu_l m^*$, and ω_p is given by $\omega_p^2 = ne/\varepsilon_0 m^*$, where e is the elementary charge, μ_l is the local electron mobility within an NC (which we use as a fitting parameter), m^* is the electron effective mass ($0.3m_e$ for ZnO[117]), and ε_0 is the permittivity of free space. A fit of the "1000+0" spectrum to the MG EMA absorption obtained from the imaginary part of ε, shown in Figure 3.3b, gives $n = 1.1 \times 10^{20}$ cm^{-3} (and $\mu_l = 21$ cm^{2}V^{-1}s^{-1}, in agreement with the value previously reported for plasma-synthesized ZnO NCs[82]). For samples approaching the IMT, however, it is less clear how to select or formulate an appropriate EMA and whether the same EMA should be used as transport behavior evolves. Therefore, for the doping series, rather than attempting to model interparticle interactions, we treat the network as a single absorber and determine n from the area under the LSPR absorption feature, which is proportional to n.[118] Using $n = 1.1 \times 10^{20}$ cm^{-3} as a baseline, we find from the increased area that n rises to a maximum value of 7.6×10^{20} cm^{-3} after 1000 flashes of doping IPL. This is similar to the maximum n attained in bulk impurity-doped ZnO[33,119] and in ZnO NCs photodoped using borohydride hole quenchers[120] (~10^{21} cm^{-3} and ~6 x 10^{20} cm^{-3}, respectively) and translates to a maximum $n\rho^3$ of 2.6.

Both sintering IPL and doping IPL increase the electrical conductivity of the ZnO NC network, σ, according to four-point measurements in the Van der Pauw configuration performed after ALD at 300 K (Figure 3.4a). Without any IPL, $\sigma = 3.8 \times 10^{-2}$ Ω^{-1}cm^{-1}. 1000 flashes of sintering IPL increases σ by two orders of magnitude, so that the "1000+0" sample has $\sigma = 3.7$ Ω^{-1}cm^{-1}. Then 1000 subsequent flashes of doping IPL increases σ by an additional factor of five, so that the "1000+1000" sample has $\sigma = 1.8 \times 10^1$ Ω^{-1}cm^{-1}. This is merely a factor of ten less than σ of typical dense microcrystalline ZnO thin films without intentional doping,[33] and is the highest σ we achieved in our ZnO NC networks by IPL, i.e. additional doping and sintering IPL flashes yielded insignificant benefit. That a combination of sintering and doping IPL is necessary for attaining this value was confirmed by control experiments in which samples were treated with 2000 flashes of either sintering or doping IPL alone (see Table S3.1 in the Supporting Information). Figure 3.4b demonstrates that n and network electron mobility, μ, are

independently tunable by doping and sintering IPL, respectively, where n is determined from the LSPR fits and $\mu = \sigma/en$. Sintering IPL does not significantly change the LSPR (see Figure S3.7 in the Supporting Information), which indicates that n remains constant, and that the increase in σ is due entirely to enhancement of μ. In contrast, doping IPL increases n while μ remains nearly constant, which is consistent with our expectation that doping IPL does not increase ρ, the primary determinant of μ. Although the Al_2O_3 infill precludes measuring ρ of the doping series samples by ellipsometry, we can now justifiably assume that ρ is constant when calculating the corresponding values of $n\rho^3$.

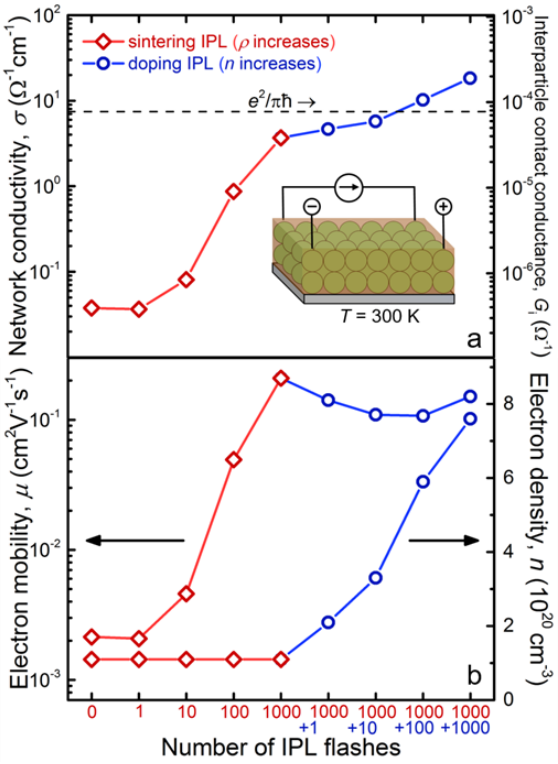

Figure 3.4: Room-temperature σ, μ, and n vs. number of IPL flashes. Red diamonds indicate treatment with sintering IPL only (sintering series), and blue circles indicate treatment with doping IPL after 1000 flashes of sintering IPL (doping series). (a) Left axis: σ from the Van der Pauw method. Right axis: G_i, from Equation 3.3. (b) Right axis: n from LSPR fits. Left axis: $\mu = \sigma/en$.

We can use σ of the ZnO NC network to estimate the interparticle contact conductance, G_i, (right axis of Figure 3.4a).[81] We treat the NC network as a random resistor network and neglect the small contribution of intraparticle resistance, i.e. we assume that the resistance of the network is due to interparticle contact resistance only, a

reasonable approximation for a network with μ much lower than that of bulk ZnO. In this case, according to the three-dimensional nodes and links model,[15]

$$G_{\mathrm{i}} = \frac{\sigma d}{(\phi - \phi_0)^{1.9}}, \tag{3.2}$$

where ϕ_0 is the percolation threshold (the minimum ZnO volume fraction at which percolation occurs), which was found to be 5% for our ZnO NC networks.[81] From Equation 3.2, we estimate G_{i} = 1.9 × 10^{-4} Ω^{-1} for the "1000+1000" sample, which is greater than the quantum conductance, $e^2/\pi\hbar$ = 7.7 × 10^{-5} Ω^{-1}, suggesting proximity to the IMT.

Having established that $n\rho^3$ surpasses the predicted critical value of ~0.3, and that G_{i} exceeds $e^2/\pi\hbar$, we proceed to examine the temperature dependence of σ near the IMT. Figure 3.5a demonstrates that for less conductive samples, log σ appears linear in $T^{-1/2}$, which is consistent with the Efros-Shklovskii variable range hopping (ESVRH) law,

$$\sigma = \sigma_0 \exp\left[-(T_{\mathrm{ES}}/T)^{1/2}\right], \tag{3.3}$$

with T_{ES} given by

$$T_{\mathrm{ES}} = \frac{Ce^2}{\varepsilon k_{\mathrm{B}} \xi}, \tag{3.4}$$

where e is the elementary charge, k_{B} is the Boltzmann constant, ε is the dielectric constant of the NC network, ξ is the electron localization length, and $C \approx 9.6$[14] is a numerical coefficient. ESVRH is confirmed by a Zabrodskii plot of the logarithmic derivative W = d[ln(σ)]/d[ln(T)] against T on a logarithmic scale[114,121] (Figure S3.8 in the Supporting Information), in which the dynamic range of conductivity is ~10^4. This analysis reveals, however, that the "1000+1000" sample does not exhibit ESVRH, and that signs of deviation from ESVRH emerge in the "1000+100" sample. Indeed, as $n\rho^3$ increases, T_{ES} (extracted from the slope of log σ vs. $T^{-1/2}$) declines to values at which hopping is expected to give way to metallic transport (Figure 3.5b). In an insulating NC network, we expect ε to be less than that of bulk ZnO (~9) and ξ to be less than d (10 nm), which translates to $T_{\mathrm{ES}} \gtrapprox$ 2000 K (a theoretical estimate of ξ from $n\rho^3$ is given in Note 3.3 in the Supporting Information). This inequality is satisfied for $n\rho^3 \approx 0.2$, whereas for large $n\rho^3$, T_{ES} falls to 40 K before becoming indeterminate.

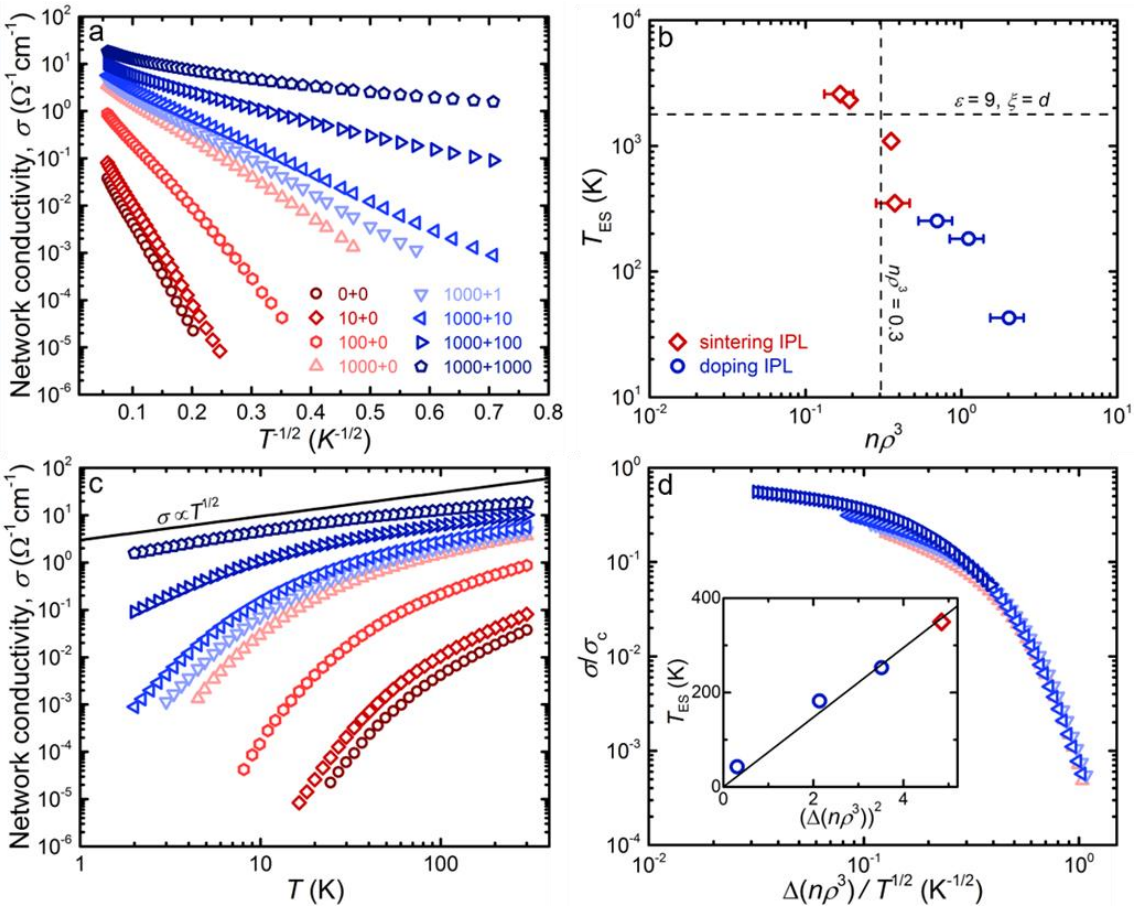

Figure 3.5: Temperature dependence of σ. Sample names are of the form "*x*+*y*", where *x* is the number of sintering IPL flashes and *y* is the number of doping IPL flashes. (a) Semilog plot of σ vs. $T^{-1/2}$. Zabrodskii analysis of these data (Figure S3.8 in the Supporting Information) indicates ESVRH for all but the most conductive sample ("1000+1000"). (b) Log-log plot of T_{ES} vs. $n\rho^3$. T_{ES} is extracted from the slope of log σ vs. $T^{-1/2}$ using Equations 3.3 and 3.4. Error bars represent the 95% confidence intervals based on the precision of ρ measurement (See Figure S3.3 in the Supporting Information) (c) Log-log plot of σ vs. T showing the approach to the power-law behavior expected at the IMT. Th black line shows the slope corresponding to $\sigma \sim T^{1/2}$. (d) Log-log plot of σ/σ_c vs. $\Delta(n\rho^3)/T^{1/2}$ of the four most conductive samples showing the scaling behavior expected near the IMT (see Equation 3.5). Inset: corresponding T_{ES} vs. $[\Delta(n\rho^3)]^2$.

The temperature dependence of σ in our most conductive sample is consistent with a continuous quantum IMT. In such transitions in bulk semiconductors, stretched exponential behavior is supplanted by a power law at the IMT at low temperature.[88,89] This shift can be explained by the condition that the critical conductivity at the IMT is $\sigma_c = e^2/\pi\hbar L_\varphi$, where L_φ is the electron phase relaxation length. The temperature dependence of L_φ is determined by the electron-electron interaction energy,[122] which at the IMT is inversely proportional to a power, z, of distance. It has been shown that z =

2,[123,124] which leads to $L_\varphi \sim T^{-1/2}$ and thus $\sigma_c \sim T^{1/2}$. Figure 3.5c shows that our most conductive sample, "1000+1000" ($n\rho^3$ = 2.6), exhibits a temperature dependence of σ close to this power law. This is supported by the Zabrodskii plot in Figure S3.8, which shows that W at low temperature is nearly constant and approaches 1/2, suggesting that the distance from the critical point is nonzero but small enough that we may hypothesize that $(n\rho^3)_c \approx 2.6$.

The scaling behavior of σ (Figure 3.5d) further supports arrival at the critical region of a continuous quantum IMT and allows us to determine the critical indices of the transition. Near an IMT of this type, if $n\rho^3$ is the tuning parameter that drives the transition,[125,126] then ξ should diverge as $[\Delta(n\rho^3)]^{-\nu}$, where $\Delta(n\rho^3) = (n\rho^3)_c - n\rho^3$, and ν can be determined empirically. Also, σ should scale with ξ/L_φ so that

$$\sigma = \sigma_c f\left[\Delta(n\rho^3)/T^{1/\nu z}\right], \tag{3.5}$$

where $f(x)$ is the scaling function. Typically the function $f(x)$ has two branches, so that conductivity data collapse into two curves on opposite sides of the transition.[88] With our data we can check for this behavior on the insulating side. Figure 3.5d shows that, when we take $(n\rho^3)_c = 2.6$ (i.e. "1000+1000" is the critical sample), the conductivities of the other four most conductive samples ("1000+0",…, "1000+100") follow Equation 3.5 with $\nu = 1$. Additionally, the inset of Figure 3.5d shows that for these samples, $T_{ES} \sim [\Delta(n\rho^3)]^2$. Hence we conclude that near the IMT both ξ and ε diverge as $[\Delta(n\rho^3)]^{-1}$.

The samples adhering to Equation 3.5 are precisely those treated with 1000 flashes of sintering IPL. Apparent deviation from Equation 3.5 in samples not fully sintered could be explained simply by greater distance from the critical point, but it is worth noting that in these samples, scaling may be difficult to detect due to error in our estimates of $\Delta(n\rho^3)$. As mentioned earlier, contact radius dispersion in these samples may reduce the accuracy of our geometrical model. If sintering does in fact improve model accuracy, then a certain number of sintering IPL flashes may be necessary for detecting scaling, regardless of distance from the critical point.

Finally, we evaluate the applicability of $(n\rho^3)_c \approx 0.3$ (Equation 1.6) to our DCNNs. Figures 3.5c and 3.5d are consistent with a significantly higher critical value, $(n\rho^3)_c \approx 2.6$,

and Figure S3.8 suggests this is a conservative estimate, as discussed earlier. Furthermore, we must of course treat this estimate as a lower bound because of our current lack of measurements of samples with higher $n\rho^3$. To understand this apparent disagreement between theory and experiment, we first consider the possibility that we have overestimated $n\rho^3$ of our samples, which would most likely be due to overestimating n, since our estimates of ρ are probably conservative, as discussed earlier. Indeed, we have indicated the difficulty of modelling interparticle interactions when extracting n from the LSPR absorption features of NC networks approaching the IMT. To obtain a lower bound on n with respect to these interactions, we can neglect interparticle effects altogether, i.e. we can model the NC network as a collection of isolated spheres embedded in Al_2O_3 using Mie theory,[23] which gives $\omega_{LSPR} \approx [ne^2/(\varepsilon_0 m^*(\varepsilon_\infty + 2\varepsilon_m))]^{1/2}/2\pi$ (where we use $\varepsilon_\infty = 3.7$ and $\varepsilon_m = 2.6$ as before). For the critical sample, this approach yields $n \approx 2 \times 10^{20}$ cm^{-3} instead of 7.6×10^{20} cm^{-3}, which translates to $(n\rho^3)_c \approx 0.7$ instead of 2.6. This lowers the disagreement with theory to at least a factor of two, which is a lower bound large enough that physical explanations are worth considering. In the model used to derive Equation 1.6, the DCNN is a cubic lattice of epitaxially connected NCs, whereas in reality our DCNNs have ZnO volume fraction $\phi \approx 33\%$ (close to tetrahedral packing) and the NCs are oriented randomly. The significance of these non-idealities is illuminated by an alternative derivation of Equation 1.6 based on the condition that $tK/\Delta = 1$ at the IMT,[126] where t is the tunneling matrix element for neighboring NCs, K is the NC network's connectivity constant, and Δ is the energy gap between consecutive electron shells. Low ϕ correspond to small K, and NC misorientation reduces t, both leading to higher $(n\rho^3)_c$. Another issue to consider is the possible presence of appreciable depletion regions near the NC surfaces, which may form when electrons are trapped by surface species such as hydroxyl groups. Penetration of these depletion regions into interparticle necks could reduce the effective contact area available for electron transport and thus raise the critical value of ρ.

3.3 Conclusion

IPL, when combined with an NC surface coating process such as ALD, is a powerful tool for tuning both n and ρ in a ZnO DCNN. This technique is clearly useful for fundamental charge transport studies, and it has the potential to play a key role in low-cost manufacturing of electronics based on ZnO NCs. Modulation of ρ with minimal impact on d should also be achievable in other UV/visible-absorbent NCs, which should enable high μ without sacrificing quantum confinement. In this work, we have used IPL to provide strong evidence of arrival at the critical region of a continuous quantum IMT and to determine the critical indices of the transition. However, even for $n\rho^3$ as high as 2.6, we have observed only the insulating side of the critical region, which suggests that satisfying Equation 1.6 may be insufficient for truly metallic behavior in our nonideal DCNNs. In future studies of the IMT, critical behavior should be examined at higher $n\rho^3$, and the importance of NC packing density, orientation, and surface depletion should be investigated.

3.4 Experimental methods

Sample preparation. NCs were synthesized and deposited using the nonthermal plasma reactor described previously.[82,90] The procedure was identical to that described in refs. 15 and 25 for ZnO with no intentional impurity doping. All samples were exposed to air upon removal from the reactor. NC networks were infilled with Al_2O_3 using a Cambridge Nanotech/Ultratech Savannah S200 ALD system and the procedure described previously.[82,90] This infilling was done before all electrical characterization and before some FTIR, XRD, and SEM measurements (specified in the figure captions). Sintering IPL and doping IPL were performed under ambient conditions using a Xenon Corp. Sinteron 2010 equipped with a 10 in. Xe U-lamp (flashlamp). The system was operated at a voltage setting of 3 kV, which translated to a surface energy density of 12 J/cm^2 per flash, according to the calibration provided by the manufacturer. The lamp's output waveform was approximately rectangular with a 660 ms period and 1 ms pulse width.

Electron transport measurements. Transport measurements were conducted on 1x1 cm samples on boro-aluminosilicate glass (Corning Eagle XG) substrates under He vapor using a Quantum Design Physical Property Measurement System (PPMS). After ALD and IPL, Al contact pads were deposited by thermal evaporation at the four corners of each square, and Au leads were attached to the Al by either wire bonding or soldering. Measurements of the temperature dependence of conductivity, σ, were performed using DC, and temperature was allowed to stabilize before each σ measurement. At the end of each run, σ was remeasured at room temperature to confirm that σ did not drift significantly over time. For the doping series, current on the order of 1 to 10 μA was sourced through two adjacent contacts, which produced an Ohmic response at all temperatures, and the voltage was measured between the other two contacts using a nanovoltmeter. This method could not be applied to the sintering series, because sample resistance neared and eventually exceeded the input impedance of the nanovoltmeter. Instead, a voltage on the order of 0.1 to 1 V was applied between two adjacent contacts, which produced an Ohmic response at all temperatures, and the current between the other two contacts was measured with an electrometer. At all temperatures, contact resistance was much lower than the NC network resistance, as confirmed by comparison of two-point and four-point measurements of the doping series. Hall measurements were performed using a DC excitation of 10 μA. Further details are provided in Figure S3.6 of the Supporting Information.

Other characterization. Fourier transform infrared (FTIR) spectra were acquired under an N_2 atmosphere from samples on polished NaCl substrates using a Bruker Alpha IR spectrometer in transmission mode. Ellipsometry spectra were acquired from samples on boro-aluminosilicate glass (Corning Eagle XG) substrates using a J.A. Woolam M44 ellipsometer. Prior to NC deposition, the backs of the glass substrates were roughened with a grinding wheel to prevent backside reflection during measurement. Spectra were fitted in WVASE using the Bruggeman effective medium approximation, assuming two components: ZnO and void. X-ray diffraction (XRD) patterns were acquired from samples on glass and Si substrates using a Bruker D8 Discover diffractometer equipped

with a Be area detector and a Co Kα source. The collected patterns were mathematically converted to Cu Kα patterns. NC diameter, *d*, was determined using the Scherrer equation with a geometrical correction factor of 4/3 to account for the NCs' spheroidal morphology.[127] Scanning electron microscopy (SEM) was performed on samples on glass substrates at an accelerating voltage of 5 keV. To minimize charging, the samples were sputter coated with 5 Å of Pt.

3.5 Acknowledgements

This work was supported primarily by the National Science Foundation through the University of Minnesota MRSEC under Award Number DMR-1420013. Parts of this work were carried out in the College of Science and Engineering Characterization Facility, University of Minnesota, which has received capital equipment funding from the NSF through the UMN MRSEC program under Award Number DMR-1420013. Parts of this work were carried out in the College of Science and Engineering Minnesota Nanocenter, University of Minnesota, which receives partial support from the NSF through the NNIN program. We thank Tim Peterson for assistance with electron transport measurements, Bryce Williams for assistance with intense pulsed light annealing, Tom Fielitz for assistance with ellipsometry, and Professor Alexander Govorov for helpful discussions.

4. Crossing the insulator-metal transition

4.1 Introduction

In the previous chapter, we observed σ scaling and near-power-law behavior suggesting proximity to the IMT, but the IMT was not completely crossed. Because the maximum $n\rho^3$ attained appeared to be at least 0.7, it seems likely that $(n\rho^3)_c$ is greater than predicted by Equation 1.6. However, without observing a complete IMT, we cannot accurately determine the true value of $(n\rho^3)_c$. Indeed, the question of whether metallic transport is even possible in these ZnO NC networks is hitherto unanswered.

In this chapter, we further increase $n\rho^3$ in order to observe a complete IMT. We do so by combining our IPL-based strategy used in Chapter 3 with the ZnO ALD method used by Lanigan and Thimsen[81]: we increase ρ with both sintering IPL and ZnO ALD, and then we increase n with doping IPL. We determine $n\rho^3$ by two methods. In the first, we use a geometric model to estimate ρ and Hall effect measurements to estimate n; this yields $(n\rho^3)_{Hall}$. In the second, we use LSPR absorption measurements rather than the Hall effect, and we reinterpret LSPR absorption in terms of NC surface depletion; this yields $(n\rho^3)_{LSPR}$. The combination of sintering IPL, ZnO ALD, and doping IPL leads to $(n\rho^3)_{Hall}$ as high as 4.7 ($(n\rho^3)_{LSPR}$ as high as 5.8). At $(n\rho^3)_{Hall}$ = 2.2 ($(n\rho^3)_{LSPR}$ = 4.1), the dependence of σ on T follows the power law $\sigma \propto T^{1/5}$, and at higher $n\rho^3$, σ becomes independent of temperature. Measurements of this T independence down to ~50 mK indicate that the most conductive samples exhibit truly metallic electron transport and suggest that $(n\rho^3)_c$ is in fact greater than 0.3, although pinpointing the criterion experimentally remains challenging due to the difficulty of measuring ρ precisely.

4.2 Results and discussion

Using the synthesis/deposition procedure described in Chapter 3, we produce ZnO NC networks with d = 10 nm, t = 300 nm, ϕ = 33%, and $\rho_0 \approx 0$. Our process for enhancing $n\rho^3$ is illustrated in Figure 4.1a. All samples are treated with 1000 flashes of sintering IPL followed by 8 cycles of ZnO ALD. As shown by Lanigan and Thimsen, ρ after ZnO ALD can be estimated accurately using a simple geometric model that treats the ZnO-coated

ZnO NCs as spheres enveloped in partial spherical shells.[81] We use a slightly modified version of their model to account for sintering IPL, which increases ρ prior to ALD:

$$\rho = \sqrt{{\rho_{\mathrm{IPL}}}^2 + {t_{\mathrm{ALD}}}^2 + d t_{\mathrm{ALD}}}, \tag{4.1}$$

where ρ_{IPL} is the value of ρ after sintering IPL but before ALD, and t_{ALD} is the nominal thickness of the ALD-grown ZnO layer based on the ALD growth rate on a flat substrate, which in our case is 0.17 nm/cycle so that t_{ALD} = 1.4 nm. For 1000 IPL flashes (which gives ρ_{IPL} = 1.5 nm, as shown in Chapter 3) and 8 ALD cycles, Equation 4.1 gives ρ = 4.1 nm. Note that d increases to ~13 nm ($d_0 + 2t_{\mathrm{ALD}}$), and that ϕ also increases considerably; according to a simple spherical-pore model,[39] ϕ = 0.68 after 8 cycles of ZnO ALD. HAADF-STEM and EDX spectrum images of a FIB-milled lamella of a fully treated sample (Figure 4.1b) appear reasonably consistent with our geometric estimates of ρ, d, and ϕ. After ZnO ALD, the NC networks are infilled with 70 cycles of Al_2O_3 to remove OH groups and seal the films as usual. Finally, the samples are treated with doping IPL, and the sample set for transport measurements is generated by varying the number of doping IPL flashes from 100 to 1000.

Figure 4.4a shows the evolution of the ZnO NC network FTIR spectrum with doping IPL. As in Chapter 3, doping IPL removes residual OH groups, and the LSPR absorption feature intensifies and slightly blueshifts. According to Hall effect measurements, n (n_{Hall}) increases from 2.2 to 6.9 × 10^{19} cm^{-3} as the number of doping IPL flashes is increased from 100 to 1000. An estimate of n from fitting an LSPR absorption feature (n_{LSPR}) will be discussed later. Using n_{Hall} and ρ = 4.1 nm, we obtain $(n\rho^3)_{\mathrm{Hall}}$, which ranges from 1.5 to 4.7.

Figure 4.2a. shows the corresponding evolution of the T dependence of σ between 300 K and 50 mK, which demonstrates a complete IMT. For $(n\rho^3)_{\mathrm{Hall}} < 2.2$, σ has a relatively strong temperature dependence, and $d[\log(\sigma)]/d[\log(T)] > 0$ while $d^2[\log(\sigma)]/d[\log(T)]^2 < 0$, revealing that σ extrapolates to zero in the limit $T \rightarrow 0$ K. In contrast, for $(n\rho^3)_{\mathrm{Hall}} > 2.2$, curvature is positive on a log-log scale, suggesting that the temperature dependence vanishes and $\sigma > 0$ at 0 K. Indeed, σ of the most conductive sample ($(n\rho^3)_{\mathrm{Hall}}$ = 4.7) is constant between 50 mK and 1.2 K, aside from fluctuations on

the order of the measurement precision (~0.1%). Furthermore, the first derivative of $\sigma(T)$ becomes negative at high T for this sample (inset of Figure 4.2a), suggesting a crossover to the phonon scattering regime expected in metals. At 300 K, $\sigma \approx 10^2\ \Omega^{-1}\text{cm}^{-1}$, on par with the highest σ obtained in bulk ZnO films without impurity doping.[33]

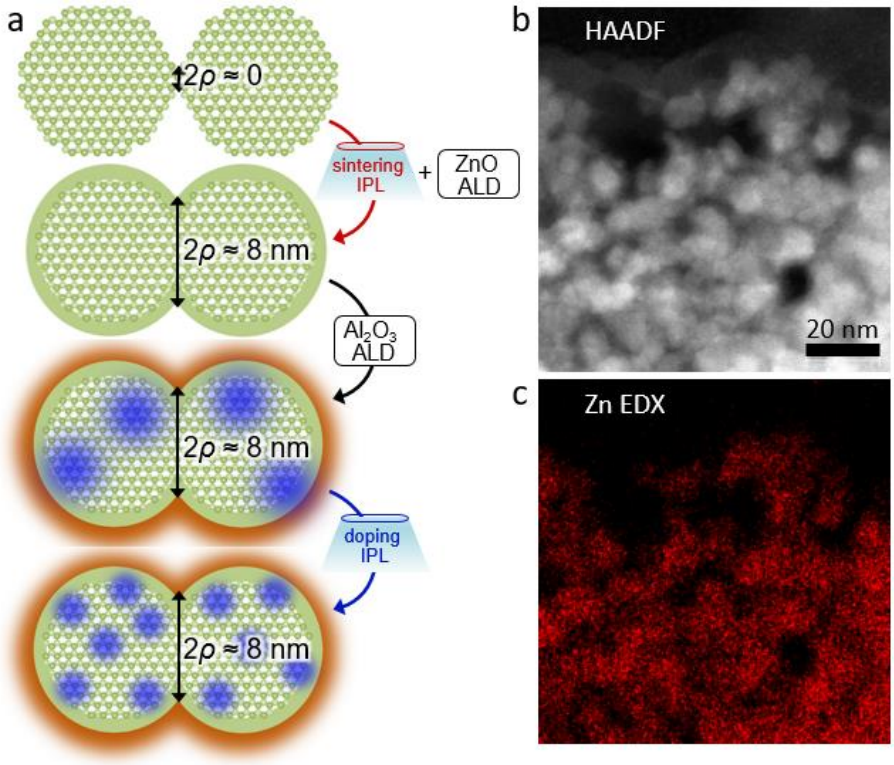

Figure 4.1: Strategy for crossing the IMT. (a) Schematic of treatment stages, which are the same as those in Chapter 3 (see Figure 3.1) but with the addition of ZnO ALD in the first stage. For all samples, the number of sintering IPL flashes is fixed at 1000 and the number of ZnO ALD cycles is fixed at 8. The number of doping IPL flashes is varied from 100 to 1000. (b) HAADF-STEM image of a FIB-milled lamella of a fully treated film. The lamella thickness is approximately 20-30 nm (two to three NC layers). (c) A map of Zn EDX counts aids the eye in discerning ZnO NCs, which are difficult to distinguish from the Al_2O_3 infill in the HAADF image.

The power law observed between the insulating and metallic regimes suggests a continuous quantum IMT with a critical point near $(n\rho^3)_{\text{Hall}} = 2.2$. Interestingly, it appears that the exponent is ~1/5, in contradiction with the results of Chapter 3, which suggest an exponent of ½. In Figure 4.2b, we test the hypothesis that $\sigma(T,\Delta(n\rho^3))$ can be described by Equation 3.5 with $(n\rho^3)_c = 2.2$ and $vz = 5$. (Although such large vz is unconventional and currently unexplained, it is not experimentally unprecedented: in correlated materials, $vz \approx 5$[128] and $vz \approx 6$[129] have been observed.) On the insulating side of the IMT, σ clearly

does exhibit this scaling behavior. On the metallic side, evidence of this scaling is slightly less convincing due to the outlying data of the sample with $(n\rho^3)_{Hall} = 4.3$ and lack of data at lower values of $\Delta(n\rho^3)/T^{1/5}$. Deviation from the scaling curve may simply be due to measurement error; near-perfect alignment with the scaling curve would occur if n_{Hall} of this sample were merely ~20% lower. Measurements of additional samples with similar σ will reveal whether this is the case. Nevertheless, we presently have sufficient evidence of a continuous quantum IMT to motivate detailed analysis of electronic behavior and the value of $n\rho^3$ near the apparent critical point, which is the focus of the remainder of this chapter.

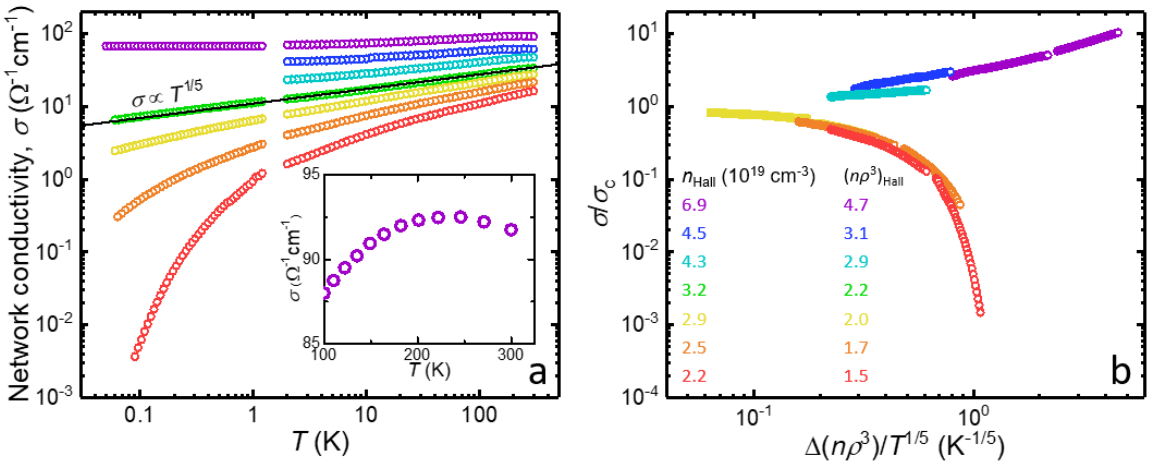

Figure 4.2: Electron transport at the IMT. (a) Log-log plot of σ vs. T. The black line shows the slope corresponding to $\sigma \sim T^{1/5}$. Inset: high-T σ of the most conductive sample. (b) Log-log plot of σ/σ_c vs. $\Delta(n\rho^3)/T^{1/2}$ showing the expected scaling on both sides of the IMT.

To verify whether $n\rho^3_c \approx 2.2$, we obtain an alternative estimate from fitting the LSPR absorption features. To maximize accuracy, we now consider more closely the interesting manner in which the LSPR feature evolves. As shown in Figure 4.4a as well as Figure 3.3b, the LSPR feature intensifies substantially upon doping IPL, while the blueshift is relatively minor. Comparing the gray and purple spectra in Figure 4.4a, the area under the absorption feature increases by a factor of ~4, while the frequency shifts from ~1500 to ~2000 cm^{-3}. If we take the area to be directly proportional to n as in Chapter 3, then typical absorption models predict that such intensification should be accompanied by a much larger blueshift: if other parameters remain constant, then the LSPR frequency

should shift by a factor of $n^{1/2}$, i.e. from ~1500 to ~3000 cm^{-3}. In Chapter 3, we attributed this blueshift suppression to increasing ε and evolving interparticle coupling near the IMT. We now test this hypothesis by studying the LSPR far from the IMT.

To obtain a sample far from the IMT, we eschewed IPL and ALD so that $\rho = \rho_0 \approx 0$. To modulate the LSPR without inducing sintering, we incrementally irradiated the as-deposited ZnO NC network with a relatively low-intensity UV lamp (~50 mW/cm^2 centered at 365 nm) under an N_2 atmosphere (<0.1 ppm O_2 and H_2O). Increasing the irradiation time exponentially, we acquired an FTIR spectrum and measured σ under N_2 after each increment to obtain the results shown in Figure 4.3. As shown in Figure 4.3a, no LSPR is evident prior to irradiation, but an LSPR absorption feature does appear after the first UV dose (a 200 ms exposure). Surprisingly, as we increase the total exposure time from 200 ms to 400 s, the LSPR feature evolution is qualitatively the same as that observed near the IMT. In this case, the area under the feature increases by a factor of ~10, while the frequency increases by merely ~20%. Meanwhile, σ increases by a factor of ~1000, as shown in Figure 4.3c.

Figure 4.3b depicts an alternative explanation of this LSPR behavior based on NC surface depletion rather than changes expected only near the IMT (such as a dramatic increase in ε). This explanation is inspired by a model developed by zum Felde, Haase, and Weller (ZHW)[130] to describe the LSPRs of electrochemically doped SnO_2:Sb NCs. Using a porous network of SnO_2:Sb NCs as the working electrode in an electrochemical cell, they performed in situ impedance and IR absorption spectroscopy as they varied the electrode potential. They found that shifting the electrode potential in the negative direction increased σ and caused the LSPR absorption feature to intensify with virtually no blueshift. They proposed that this LSPR behavior implied that the total number of free electrons, N, increased while their density, n, remained constant (indeed, impedance spectroscopy suggested that the increase in σ was due exclusively to an increase in μ). In their view, each NC initially had a wide depletion layer at its surface, and shifting the potential in the NC core in the negative direction reduced the potential drop across this depletion layer and thereby reduced its width, w. This hypothetical decrease in w

corresponded to an increase in the undepleted volume, *V*, which accounted for the proposed increase in *N* at constant *n*.

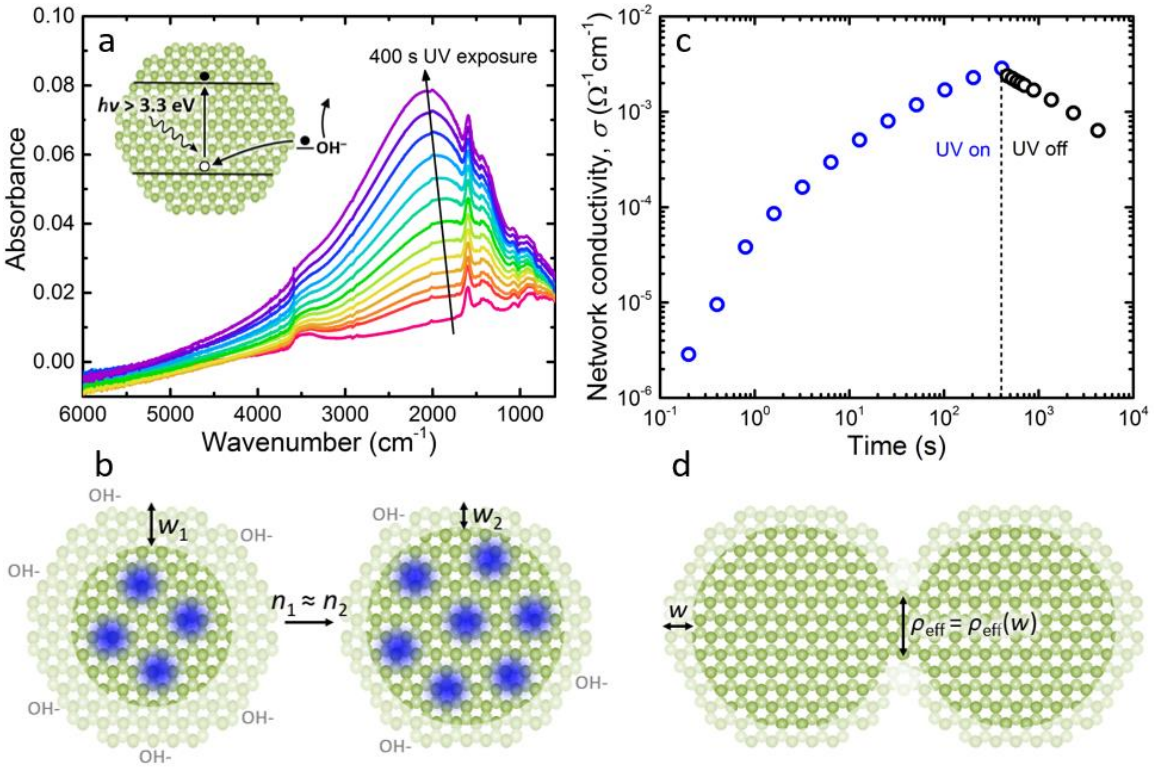

Figure 4.3: Results of low-intensity UV irradiation experiments far from the IMT and NC schematics illustrating the hypothesized influence of surface depletion. (a) FTIR spectrum evolution with UV dose. As in the case of doping IPL near the IMT (Figure 4.2.a), the blueshift of the LSPR is small compared with the intensification. (b) This behavior can be explained by a depletion layer at the NC surface which decreases in width under illumination due to charge transfer from the surface to the core. If the undepleted volume and number of free electrons increase nearly proportionally, then *n* remains nearly constant. (c) Corresponding evolution of *σ* revealing remarkable sensitivity of *σ* to UV exposure. Whereas the area under the LSPR absorption feature increases by only a factor of ~10, *σ* increases by a factor of ~1000. (d) This sensitivity could be explained by an effective interparticle contact radius determined by the surface depletion width.

The model illustrated in Figure 4.3c is analogous to that of ZHW. We propose that a lightly photodoped ZnO NC may have a wide surface depletion layer due to negative charge trapped at the NC surface by remaining OH groups. Additional photodoping could effectively transfer negative charge from the surface to the core, reducing *w* and increasing the undepleted volume so that *n* remains nearly constant. This could explain not only the nearly constant LSPR frequency but also the remarkable sensitivity of *σ* to UV exposure. As illustrated in Figure 4.3d, surface depletion layers could penetrate

interparticle necks, creating an effective ρ for electron transport, ρ_{eff}, smaller than the ρ defined by the ZnO lattice. We know from Chapter 3 that μ is strongly dependent on ρ, and so it is conceivable that an increase in ρ_{eff} due to a decrease in w could result a dramatic enhancement of μ.

Supposing that this depletion model also describes the effects of doping IPL near the IMT (Figure 4.4a), we obtain $(n\rho^3)_{LSPR}$ by making the following assumptions:

(1) Doping IPL increases $(n\rho^3)_{LSPR}$ by increasing ρ_{eff}, while n remains constant.

(2) At the maximum photodoping level, $\rho_{eff} = \rho = 4.1$ nm.

(3) Near $\rho_{eff} = \rho$, $\rho_{eff}^3 \propto V \propto N \propto$ area under the LSPR absorption feature.

(4) At a sufficiently low photodoping level, w is sufficiently large that $\rho_{eff} \approx 0$ and the NC network can be approximated as a collection of electronically isolated pockets of high n embedded in depleted ZnO.

Based on assumptions 1-3, we obtain ρ_{eff} for each sample from the areas under the LSPR absorption features in Figure 4.4a (excluding the gray spectrum); this yields ρ_{eff} ranging from 3.2 to 4.1 nm. Then based on assumption 4, we obtain n_{LSPR} by using Mie theory to fit the LSPR of a lightly photodoped sample (gray spectrum, $\sigma \approx 6\ \Omega^{-1}cm^{-1}$), letting $\varepsilon_m = \varepsilon_{ZnO} = 3.7$. This Mie fit, shown in Figure 4.4a, yields $n = 8.6 \times 10^{19}$ cm^{-3}. Finally, $(n\rho^3)_{LSPR}$ is the product of n_{LSPR} and ρ_{eff}^3, which ranges from 2.9 to 5.8.

Figure 4.4b compares $(n\rho^3)_{LSPR}$ to $(n\rho^3)_{Hall}$. The level of agreement between these two quantities is best understood through comparing their maximum values, where the two estimates of ρ converge ($\rho_{eff} = \rho = 4.1$ nm), and the only difference lies in n. At this point, we find that the ratio of $(n\rho^3)_{LSPR}$ to $(n\rho^3)_{Hall}$, i.e. the ratio of n_{LSPR} to n_{Hall}, is approximately $4/\pi$. According to a theoretical study of the Hall effect in granular metals,[131] this is in fact the expected ratio of the true value of n to n_{Hall} in a cubic lattice of NCs with no Coulomb interactions. The study showed that this ratio is simply that of the cross-sectional areas of the lattice cell and the NC, which is $4/\pi$ for cubically-packed spheres. Given that this an appropriate model of our NC network, which has $\phi = 0.68$ and likely has negligible Coulomb interactions at high T, our observation of this ratio suggests that our approaches to determining n are in fact reasonable, at least at high n.

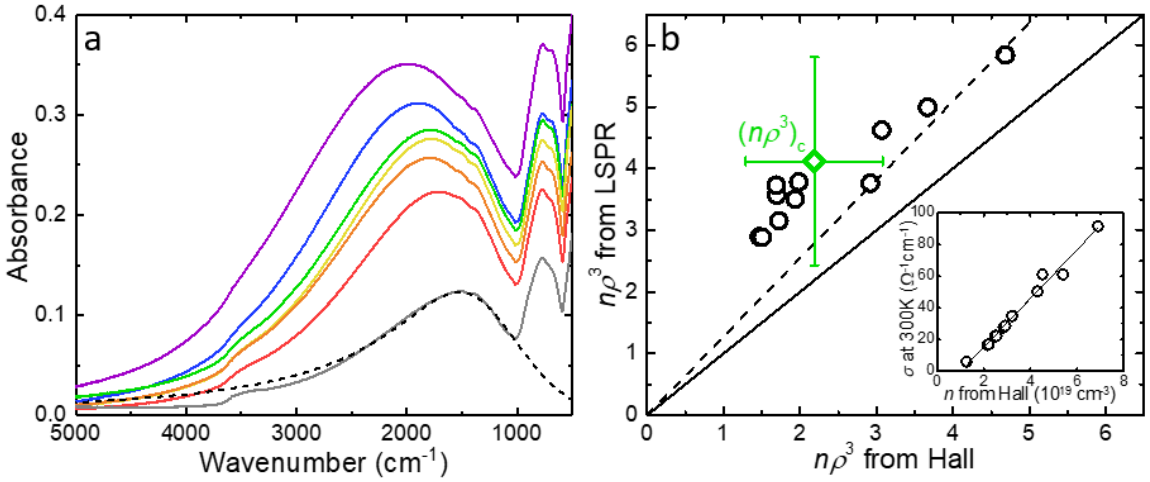

Figure 4.4: LSPR and $n\rho^3$ near the IMT. (a) FTIR spectrum evolution with doping IPL dose. The OH feature around 3500 cm^{-1} diminishes and the LSPR absorption feature intensifies and slightly blueshifts. The gray spectrum corresponds to a sample far from the IMT and is fitted to determine n_{LSPR} (dashed black line): the NCs are assumed to have wide surface depletion layers so that the LSPR is due to electronically isolated pockets of high n in the NC cores. Mie theory is used to model the network as an ensemble of noninteracting conductive ZnO spheres embedded in depleted ZnO. (b) $n\rho^3_{LSPR}$ of all samples based on this single Mie fit vs. $n\rho^3_{Hall}$. The green diamond corresponds to the sample at the IMT critical point (green spectrum in (a)). The error bars represent an uncertainty in ρ of ± 0.5 nm. The solid and dashed lines have slopes 1 and 4/π, respectively; the latter is the ratio of n within an NC to n_{Hall} predicted by Kharitonov & Efetov.[131] Inset: σ at 300 K vs. n_{Hall}.

The green diamond in Figure 4.4b corresponds to the critical sample, which has $(n\rho^3)_{Hall}$ = 2.2 and $(n\rho^3)_{LSPR}$ = 4.1. These two estimates of $(n\rho^3)_c$ are obtained from fundamentally different measurements and models, and their relative accuracy is open to debate. For higher $n\rho^3$, good agreement between $(n\rho^3)_{Hall}$ and $(n\rho^3)_{LSPR}$ can be obtained simply by multiplying the former by $4/\pi$. However, it appears that $(n\rho^3)_c$ may lie in a regime where the two estimates cannot be reconciled by this correction factor, which is unsurprising considering that the factor was derived for metallic networks. An argument could be made for favoring $(n\rho^3)_{LSPR}$ in this regime based on the success of our depletion model; this model not only explains the LSPR blueshift suppression but also yields an estimate of n in agreement with the maximum Hall value. At the same time it is worth noting that the disagreement between $(n\rho^3)_{Hall}$ and $(n\rho^3)_{LSPR}$ may be small compared to the uncertainty in ρ^3. Recall that in both cases, our ρ estimate is based on a simple geometrical model, and that currently available TEM images can do no more than suggest accuracy within ~1-2 nm. Assuming that the uncertainty in ρ is ± 0.5 nm, the uncertainty in $(n\rho^3)_c$ is ± 40%, as shown by the error bars in figure 4.4b.

4.3 Conclusion

Using a combination of sintering IPL, doping IPL, and ZnO ALD, we have driven $n\rho^3$ beyond the critical value and induced a complete IMT. At large $n\rho^3$, we have observed truly metallic behavior: σ is T-independent at low T and has a negative T coefficient at high T. At 300 K, we have obtained σ as high as ~10^2 Ω^{-1}cm^{-1}, revealing that a ZnO NC network can in fact match σ of an undoped bulk ZnO film. These encouraging results lend plausibility to the vision of technologically relevant highly conductive NC films, perhaps of AZO or ITO. It could be worthwhile to revisit the challenge of impurity doping in the plasma; if the formation of insulating phases could be prevented and if somehow n could be increased well above 10^{20} Ω^{-1}cm^{-1}, then perhaps even higher σ could be attained.

In an attempt to estimate $n\rho^3$ more accurately, we have reinterpreted LSPR absorption in terms of NC surface depletion and explored the possibility that photodoping effectively increases ρ rather than n. Assuming that the uncertainty in ρ is ± 0.5 nm, this interpretation yields $(n\rho^3)_c = 4.1 \pm 1.7$, while a more conventional approach based on Hall measurements yields $(n\rho^3)_c = 2.2 \pm 0.9$. In either case it appears likely that $(n\rho^3)_c$ is in fact greater than 0.3 and that an adjustment to Equation 1.6 should be considered for these ZnO NC networks. The atypical power law at the IMT, $\sigma \propto T^{1/5}$, also merits further investigation.

4.4 Experimental methods

Two previously undescribed characterization techniques were introduced in this chapter.

Electron transport measurements. Samples were cooled to ~50 mK in an Oxford Triton 200 dilution refrigerator. Four-point conductivity measurements were performed using a custom IVVI rack with a Keithley 2000 DC voltmeter and Stanford Research Systems SR830 lock-in amplifier operated at 13 Hz. Silver paint was used to mount the samples to a copper stage. Because the undersides of the sample substrates were incidentally coated with conductive ZnO during ALD, an electrically insulating interlayer was needed to prevent a short through the silver paint. Therefore, thin (0.5 mm) pieces of

sapphire were attached the bottoms of the substrates with a thermally conductive adhesive prior to sample mounting.

Transmission electron microscopy. Cross-sectional STEM specimens were prepared using a focused ion beam (FEI Helios NanoLab G4) using 30 kV Ga ions, followed by progressively lower voltage ion milling (down to 1 kV) to remove damaged layers from the specimen surfaces. Scanning transmission electron microscopy-energy dispersive X-ray (STEM-EDX) data was obtained in an aberration-corrected FEI-Titan G2 60-300 STEM equipped with a Super-X EDX, operated at 60 or 200 kV with a 25 mrad convergence angle, 125 pA beam current, and a 68 mrad high-angle annular dark field (HAADF) detector inner angle. EDX spectrum images were acquired with frame-by-frame drift correction through the Bruker ESPRIT 1.9 software with a dwell time of 3 μs/pixel.

5. Technological potential

5.1 Introduction

Thus far we have used the ZnO NC network as a platform for basic science, and we have suggested that our insights into increasing σ will perhaps be most useful when applied to inherently more conductive materials such as ITO. Nevertheless, as discussed in Chapter 1 (Section 1.4), insulating or moderately conductive ZnO NC networks may have roles to play in certain emerging NC technologies. In this chapter, we explore the applicability of our plasma-synthesized ZnO NCs in a few of these technologies and consider whether our understanding of doping and charge transport can lead to performance enhancements. We also investigate the feasibilities of attaining high σ without ALD and of developing a scalable atmospheric-pressure synthesis process, both of which could be important steps toward low-cost manufacturing.

5.2 Plasmonic nanocomposites of zinc oxide and titanium nitride

TiN nanostructures have recently gained considerable attention due to their combination of potentially tunable near-IR and/or visible LSPR with relatively high thermal and chemical stability.[132–138] One intriguing application is hot-electron energy conversion. In general, excitation of individual electrons is one of several plasmon decay pathways, and the energy imparted to these electrons can be captured if they are injected into a semiconductor prior to their relaxation.[48] Typical devices based on this concept employ a noble metal as the plasmonic absorber, but TiN is an emerging alternative. For example, photocatalytic water splitting has been achieved by transferring hot electrons from TiN NCs into TiO_2 nanowires.[139]

Here we show that a ZnO NC network can serve as a scaffold for growing TiN nanostructures by plasma-enhanced ALD (PEALD). We grow TiN on our typical ZnO films on SiO_2 substrates (d = 10 nm, t = 300 nm, ϕ = 33%) using a commercial PEALD reactor (Cambridge UltraTech Fiji 200 Gen 2). In a typical deposition, the film is heated to 270 °C under N_2 flow at 25 Torr, and TiN is grown by alternating pulses of tetrakis(dimethylamido)titanium (TDMAT) and N radicals. The latter are supplied by a

remote RF inductively coupled plasma (ICP). The TDMAT and plasma pulse durations are 30 and 40 s, respectively, and the purge time between pulses is 30 s.

Figure 5.1 shows the results of a 55 cycle TiN deposition on a typical ZnO NC network. Whereas an uncoated ZnO network is transparent at wavelengths between ~400 and 2500 nm, the TiN network shows strong plasmonic absorption with a peak near 1000 nm, as shown in Figure 5.1a. For comparison, the absorption spectrum of the same 55 cycle coating on a smooth glass substrate is also shown. The much stronger absorption of the ZnO/TiN composite suggests that a significantly greater quantity of TiN is deposited due to the high surface area of the ZnO NC network (although enhanced intrinsic absorptivity may also be a factor). Indeed, a HAADF-STEM image (Figure 5.1b) and EDX/EELS elemental maps (Figure 5.1c,d) reveal that TiN infills the network, and that near the surface of the network, ZnO NCs are enveloped in TiN shells. However, Figure 5.1c,d,e shows that the deposited TiN quantity steadily diminishes with increased distance from the surface of the film. This is unsurprising for a remote-plasma based deposition process; infill depth is expected to be limited by N radical combination and thus should be less than that achieved by conventional ALD (Figure 1.7). In fact, the deposition of any TiN beneath the first few layers of ZnO NCs is remarkable and perhaps facilitated by unexpected growth mechanisms. TiN deposition (or lack thereof) should be studied in the absence of N_2 flow to determine whether N growth species are supplied by TDMAT.

Regardless of the TiN growth mechanism, this ZnO/TiN nanocomposite may be well-suited for hot electron collection. Recently, an interface between TiN and insulating ZnO was shown to form an Ohmic contact that allowed for self-powered (zero-bias) photodetection based on hot electron injection from TiN into ZnO.[140] Perhaps the high-area omnidirectional interface in our ZnO/TiN nanocomposite could enable high-efficiency photodetection over a wide angular range, provided that relatively low n is maintained in the ZnO to minimize electron-hole recombination. Sintering IPL and/or ZnO ALD could be used to maximize μ and facilitate transport of photoexcited electrons across the NC network without increasing n.

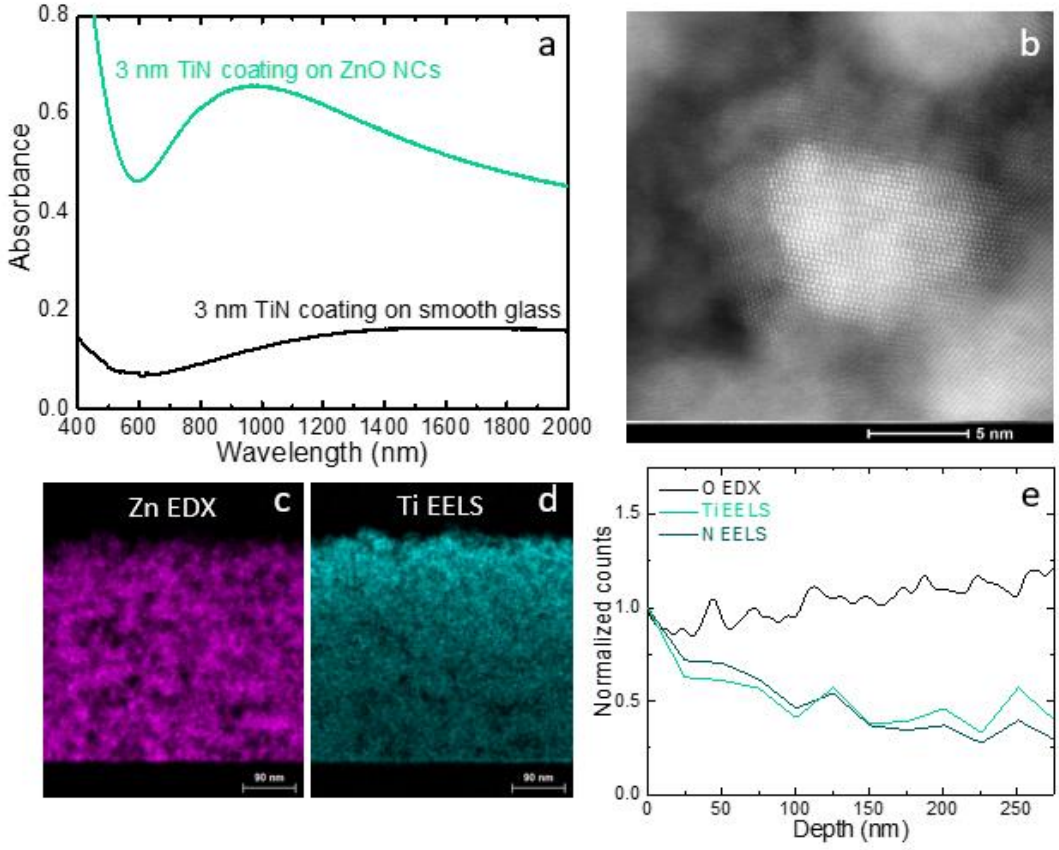

Figure 5.1: ZnO/TiN nanocomposite. (a) UV-vis-NIR absorption spectra of a 55 cycle TiN coating on a ZnO NC network (turquoise) and a smooth glass substrate (black). (b) HAADF-STEM image of a FIB-milled lamella approximately 20-30 nm (two to three NC layers) in thickness. The image was acquired at a depth of ~20-30 nm from the film surface. (C) EDX map of Zn counts. (d) EELS map of Ti counts. (e) Corresponding plot of EDX/EELS counts vs. depth. Counts are normalized by dividing raw counts by Zn counts at each depth and then rescaling the counts curves so that their value is one at a depth of zero.

5.2 Thermopower and thermal conductivity

As mentioned Chapter 1, it is generally accepted that thermoelectric materials must have $\sigma \geq 10^2\ \Omega^{-1}\text{cm}^{-1}$ in order to be usable in reasonably high-efficiency thermoelectric generators. Having reached this milestone in Chapter 4, we now examine the thermopower and thermal conductivity of variously treated ZnO NC networks to assess their potential for high thermoelectric performance and/or fundamental studies of the Seebeck effect in highly conductive NC networks. We evaluate performance using the standard figure of merit, $ZT = \alpha^2\sigma T/\kappa$, where α is the Seebeck coefficient and κ is the thermal conductivity. Previously, $ZT > 0.1$ at 300 K[141] and $ZT > 0.4$ at 1000 K[142] have

been reported for nanostructured AZO films. While these values are too low for general thermoelectric power generation, a combination of moderate *ZT* near 300 K, visible transparency, and mechanical flexibility may be valuable for niche applications.[143]

For preliminary evaluation, we measured the thermoelectric properties of our ZnO NC networks at room temperature only. We determined α by applying lateral temperature gradients across typical films on SiO_2 substrates and measuring the open circuit voltage, and we determined κ by time-domain thermoreflectance (TDTR) measurements of typical films coated with 100 nm Al transducer layers by thermal evaporation. To obtain samples with $\sigma \approx 10^2\ \Omega^{-1}cm^{-1}$, we used a treatment procedure different from that described in Chapter 4. Rather than photodope, we Al-doped the ZnO infill by periodically replacing DEZ pulses with TMA pulses (1 TMA pulse in every 20 cycles). We also completely infilled with AZO rather than using a combination of ZnO and Al_2O_3 as in Chapter 4. This approach yielded $\sigma = 6.3 \times 10^1\ \Omega^{-1}cm^{-1}$, and annealing the NCs for one hour at 300 °C under H_2 prior to ALD yielded $\sigma = 1.1 \times 10^2\ \Omega^{-1}cm^{-1}$. For comparison, we also measured α and κ of three samples described in Chapter 3: a sample treated with Al_2O_3 ALD only ("0+0"), a sample treated with 1000 flashes of sintering IPL before ALD ("1000+0"), and a sample treated with 1000 flashes of sintering IPL and 1000 flashes of doping IPL ("1000+1000").

The thermoelectric properties of these samples are given in Table 5.1. The highest *ZT* value, 1.7×10^{-3}, is that of the unannealed AZO-infilled sample (sample 1), which has a fairly low α of -46 μV/K. Replacing the AZO infill with Al_2O_3 increases α to -90 μV/K (sample 3), but the corresponding drop in σ leads to $ZT < 10^{-5}$. Sintering IPL and doping IPL do improve *ZT* (samples 4 and 5), but it appears that $ZT > 10^{-3}$ is possible only with an AZO infill (or perhaps a ZnO infill), and that *ZT* on par with the highest values in the ZnO literature is unobtainable with the treatment methods explored in this thesis.

The values of κ, however, are promising. Al_2O_3-infilled samples have $\kappa = 1.4\ Wm^{-1}K^{-1}$, on par with the lowest values reported in the thermoelectric ZnO literature,[141,142,144] and lower κ is attainable by reducing the number of ALD cycles from 70 to 10: sample 6 has $\kappa = 0.4$. Perhaps κ could be further reduced by eliminating the ALD coating altogether, although this leads to mechanical softness which complicates

TDTR measurements and may limit technological applicability. Regardless, κ = 0.4 is remarkably low for a ceramic, and sample 6's combination of low κ, high hardness and mechanical stability, high melting point, and visible transparency make it an attractive thermal barrier material.

Table 5.1: Thermoelectric properties of ZnO NC networks. κ of sample 5 has not yet been measured but is expected to be the same as that of samples 3 and 4 due to the negligibility of the free electron contribution to κ predicted by the Wiedemann-Franz law.

Sample	ALD infill	NC treatment	σ (Ω^{-1}cm^{-1})	α (μV/K)	κ (Wm^{-1}K^{-1})	ZT
1	100 cyc. ZnO:Al	none	6.3×10^{1}	-46	2.3	1.7×10^{-3}
2	100 cyc. ZnO:Al	300 °C thermal anneal	1.1×10^{2}	-29	3.7	7.5×10^{-4}
3	70 cyc. Al_2O_3	none	3.8×10^{-2}	-90	1.4	6.6×10^{-6}
4	70 cyc. Al_2O_3	1000 flashes sintering IPL	3.7×10^{0}	-49	1.4	1.9×10^{-4}
5	70 cyc. Al_2O_3	1000 flashes sintering IPL + 1000 flashes doping IPL	1.8×10^{1}	-39	[1.4]	[5.9×10^{-4}]
6	10 cyc. Al_2O_3	none	< 10^{-6}	--	0.4	--

5.3 Reducing roughness and porosity with hydraulic compaction

Minimizing visible light scattering in ZnO NC networks is potentially beneficial in certain hot-electron energy conversion and thermal insulation applications, and invariably critical in photovoltaics. Given that in the visible spectrum, ZnO is non-absorbent and both the NC and pore diameters are much smaller than λ, the primary source of scattering apart from refraction is likely to be film surface roughness. It is apparent in Figures 1.7 and 5.2c that the as-deposited film surfaces can have feature sizes exceeding $\lambda/8$ for all visible λ, and that visible Rayleigh surface scattering is expected.

Figure 5.2a depicts a simple remedy for surface roughness: we use a hydraulic press to apply pressure on the order of 10^2 MPa to the ZnO NC network surface. The ZnO NC networks used in this study initially have $\phi \approx 0.35$ and $t \approx 450$ nm. Figure 5.2b shows that the film can be nearly completely compacted at a pressure of ~5 × 10^2 MPa, i.e. that ϕ approaches ~0.64, the limit for randomly packed spheres. Correspondingly, t decreases to ~250 nm. Figure 5.3c,d shows that even at a milder compaction pressure of 1.8 × 10^2 MPa, surface roughness decreases substantially as the film is compressed. The difference is clearly visible by eye even at a near-normal viewing angle.

This straightforward approach to minimizing visible light scattering should be compatible with most devices employing ZnO NCs, since the compressive strengths of most metals, semiconductors, and dielectrics exceed ~200 MPa. Importantly, σ of the ZnO NC network is typically nearly unaffected by compaction at the lower end of the investigated pressure range, although occasionally we observe a small decrease in σ likely due to scratching that can occur during manual application of the steel die to the sample surface. Also, the porosity tuning afforded by this compaction process may lead to new applications. Combining hydraulic compaction with manipulation of deposition pressure,[81] we can now access any value of ϕ between ~0.1 and 0.6, enabling, for example, wide and precise modulation of the network's refractive index.

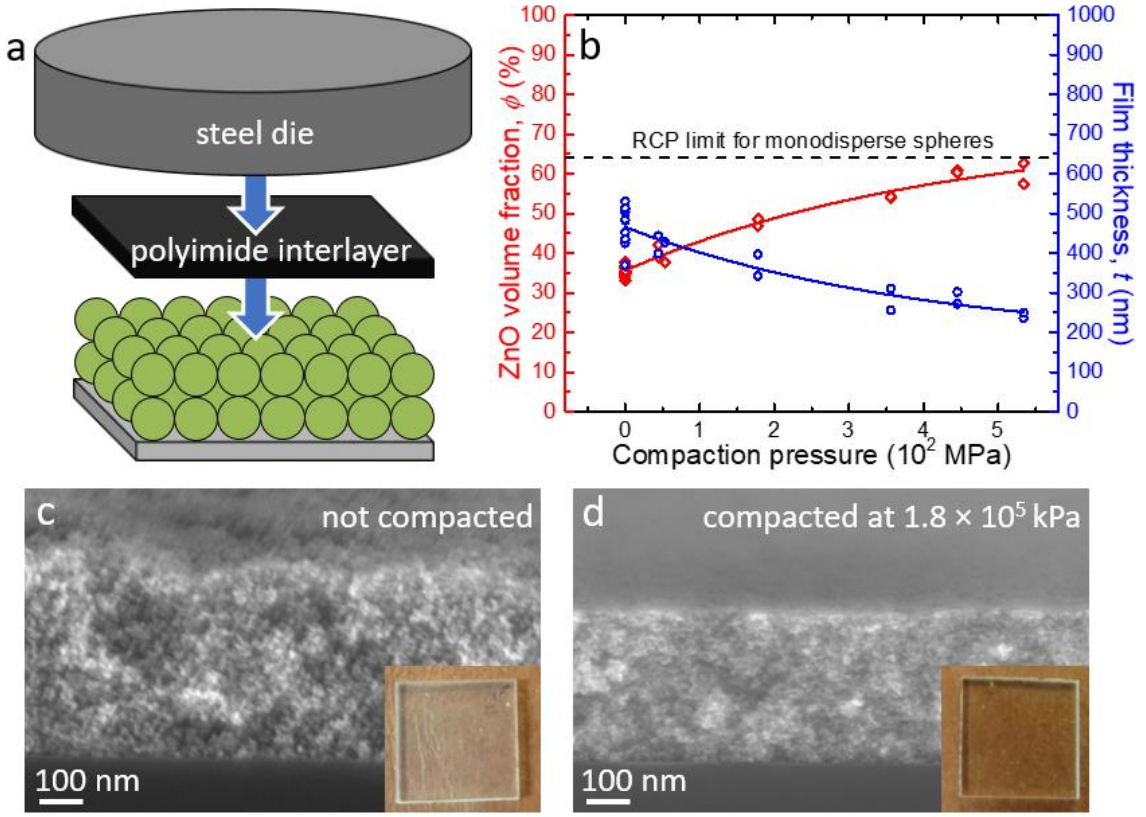

Figure 5.2: Hydraulic compaction of ZnO NC networks. (a) Compaction schematic. (b) ZnO volume fraction, φ, and film thickness, t, vs. compaction pressure. (c,d) Cross-sectional SEM images and plan-view photographs of an NC network before and after compaction.

5.4 Attaining high air-stable conductivity without atomic layer deposition

Low-cost, high-throughput roll-to-roll manufacturing requires rapid NC deposition and treatment. In our ZnO NC network fabrication process, the rate-limiting step is ALD. A ZnO film with t = 300 nm is deposited in 30 s, a 1000-flash IPL treatment is completed in 11 minutes, and a 70-cycle Al_2O_3 ALD coating requires 70 minutes (excluding prebake time). Since the IPL flash duration is 1 ms, expediting sintering and photodoping is a matter of shortening the interval between flashes or developing a process based on continuous illumination, perhaps employing a UV laser. Expediting ALD is less straightforward. Although considerable progress has been made on roll-to-roll-compatible ALD techniques such as spatial ALD,[145,146] uniformly infilling nanopores by these methods has been elusive.[147] ALD infilling on a time scale comparable to that of the NC deposition currently appears infeasible due to the inevitably slow diffusion of ALD precursors in a nanoporous solid,[148] especially at the low temperatures necessitated by flexible substrates.

In principle, high air-stable σ is attainable in our ZnO NC networks by any coating process that (1) removes surface OH groups, and (2) prevents subsequent oxidation. An Al_2O_3 infill satisfies the first requirement via the reaction of TMA with OH and fulfills the second when the coating is sufficiently thick. Thimsen *et al.* showed that an Al_2O_3 coating thickness greater than 7 nm is necessary for maximizing air-stable σ.[39] Figure 5.3a shows that this requirement cannot by circumvented by photodoping: reducing the Al_2O_3 thickness decreases the maximum σ obtainable by UV exposure as well as the photoconductivity lifetime. However, if OH groups are removed by UV irradiation rather than the coating process, then the need for coating the internal surfaces of the film is obviated.

The results shown in Figure 5.3b,c reveal that the Al_2O_3 infill can likely be replaced by a combination of photochemical OH removal and rapid film sealing with ethylene-vinyl acetate (EVA). Highly impermeable to water and oxygen, EVA is commonly used in food packaging as well as solar cell encapsulation.[149] We deposited a typical ZnO NC network on a NaCl substrate and removed OH groups by irradiating the film with a low-

intensity UV lamp (~50 mW/cm^2 centered at 365 nm) for 120 s, resulting in the typical LSPR. We then sealed the film with EVA by compressing an EVA bead (18 wt. % vinyl acetate) between the film and an additional NaCl plate at 300 °C. (This temperature was selected to facilitate manual application of the melted EVA; a process temperature ≤180 °C should be easily attainable with the proper lamination equipment). The resultant EVA coating had a thickness on the order of 100 μm. After a 60 s air exposure, the LSPR of an uncoated film is eliminated (Figure 5.3b), whereas the LSPR absorption intensity of an EVA-coated film is undiminished (Figure 5.3c), indicating that *n* is stable.

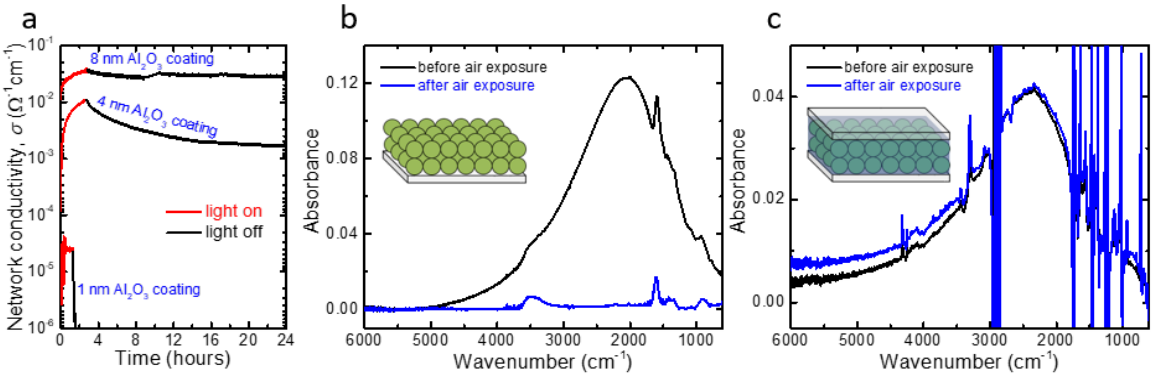

Figure 5.3:Strategy for achieving high air-stable *σ* without ALD. (a) Photoconductivity rise and decay of ZnO NC networks with varied Al_2O_3 coating thickness. (b,c) FTIR absorption spectra of an uncoated film (b) and an EVA-coated film (c) before and after a 60 s air exposure. The narrow and intense features in (c) are due to EVA.

5.5 Synthesis at atmospheric pressure[*]

In any industrial process based on plasma synthesis, raising the synthesis pressure can significantly reduce capital and operating expense. Currently, most atmospheric-pressure glow plasmas for NC synthesis are micro-plasmas: miniature reactors with characteristic lengths less than 1 mm. While the small size ensures a nonthermal plasma (gas temperature, T_g << electron temperature, T_e), it limits the nanoparticle production rate and yield. The main challenges in the development of a large-volume atmospheric-pressure glow discharge (APGD) include maintaining nonthermality and discharge uniformity over a large volume. Since Kanazawa *et al*. developed the first stable APGD in the

[*] Reproduced in part with permission from Bilik, N.; Greenberg, B. L.; Yang, J.; Aydil, E. S.; Kortshagen, U. R. *J. Appl. Phys.* **2016**, *119*, 243302. Copyright 2016 American Institute of Physics.

1970s,[150] various reactor designs and ignition techniques have been explored to achieve uniformity in APGDs with characteristic lengths ranging from a few mm up to a few cm.[151–162] For the purpose of NC synthesis, the APGD's large volume and uniformity should enable rapid and controllable production. Here we present an APGD reactor for ZnO NC synthesis. The reactor is an RF dielectric barrier glow discharge with a characteristic length of 2.4 mm and a reactor volume approximately 10 times larger than that of a microplasma. The applied power typically ranges from 25W to 45W; this is comparable to the applied power used in a microplasma for photoluminescent Si NC synthesis.[163]

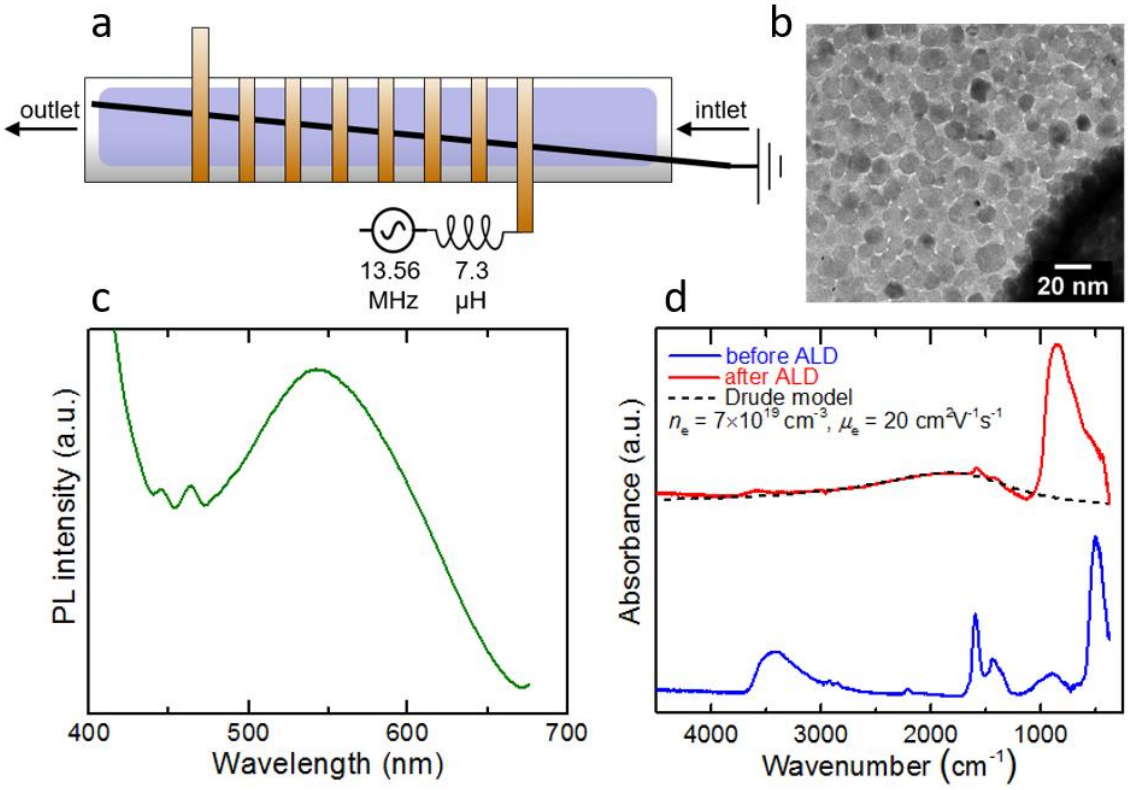

Figure 5.4: APGD synthesis of ZnO NCs. (a) Reactor schematic. (b) TEM of typical ZnO NCs. (c) PL spectrum of 4-10 nm NCs. (c) FTIR absorption spectra of 11-13 nm NCs before and after infilling with 7.7 nm of Al_2O_3 by ALD. The dashed black line is the fit of the LSPR obtained from Mie theory.

Figure 5.4a shows a schematic of the APGD reactor. The reactor has a concentric cylinder geometry. The outer copper electrode is a coil wrapped around a quartz tube functioning as the dielectric barrier, and the inner electrode is a grounded tungsten wire. While the helical electrode design resembles an induction coil, the discharge is

capacitively coupled, as one end of the coil is floating. The capacitive nature is confirmed by the reactor's current-voltage waveform, in which the current leads the voltage by 60–75°. The quartz tube has an outer diameter of 7 mm and a thickness of 1 mm; the coil is 55 mm in length. A discharge is generated between the electrodes using a 13.56 MHz RF source and a 3–23 SLM He or Ar flow. This discharge appears diffuse when viewed by eye, though at large power densities and low gas flow rates, localized filament formation is visible in Ar-O discharges. As shown in Figure 5.4a, the center tungsten electrode is slanted so that the reactor gap spacing is nonuniform with an average gap spacing of 2.4 mm. This nonuniform gap spacing ensures discharge uniformity by encouraging the production of a pre-ionization electron population, similar to that of the double-discharge excitation gas laser developed by Laflamme.[160] The discharge is initiated locally in a region where the gap spacing is minimal, and then it expands to fill the entire volume as the electrode voltage is increased, resulting in discharge uniformity over a large volume. This uniformity could be due to the initial discharge supplying free electrons and thereby suppressing streamer formation and the glow-to-arc transition.[164] ZnO NCs are synthesized by injecting O_2 and DEZ into the plasma, and the NCs are collected under ambient conditions on Si substrates mounted approximately 2 mm from the reactor outlet. A TEM image of typical NCs is shown in Figure 5.4b. The maximum NC production rate of this reactor is ~400 μg/min, ~100 times higher than a typical rate achieved in microplasma-based synthesis.[163]

Figure 5.4c,d shows the optical properties of the ZnO NCs. 4–10 nm NCs dispersed in ethanol and illuminated by a 350 nm excitation source exhibit a luminescence peak at ~550nm (Figure 5.4c), possibly due to the OH groups on the NC surfaces. In ZnO NCs, surface OH groups are known to provide intermediary states through which holes migrate to singly ionized oxygen vacancies, creating doubly ionized recombination centers which enable green emission;[165] a luminescence peak at ~550 nm in low-pressure-plasma-synthesized ZnO NCs was attributed to this mechanism.[166] These OH groups, however, suppress the LSPR (Figure 5.4d). Following a procedure previously applied to low-pressure-plasma-synthesized ZnO NCs,[39] we use ALD of Al_2O_3 to remove the OH groups and seal the ZnO NCs, resulting in an air-stable LSPR at ~1900 cm^{-1} in 11–13 nm

nanocrystals. Fitting the LSPR feature using Mie theory with the classical Drude dielectric function, we find the free electron density (n) and the intraparticle electron mobility (μ) to be 7×10^{19} cm^{-3} and 20 $cm^2V^{-1}s^{-1}$, respectively. These values are similar to those of the ZnO NCs synthesized in a low-pressure plasma, and the high n is likely due to the oxygen vacancies evidenced by the green PL.

References

(1) Dabbousi, B. O.; Mikulec, F. V; Heine, J. R.; Mattoussi, H.; Ober, R.; Jensen, K. F.; Bawendi, M. G. *J. Phys. Chem B* **1997**, *101*, 9463.

(2) Pi, X. D.; Liptak, R. W.; Nowak, J. D.; Wells, N. P.; Carter, C. B.; Campbell, S. A.; Kortshagen, U. *Nanotechnology* **2008**, *19*, 245603.

(3) Ning, Z.; Voznyy, O.; Pan, J.; Hoogland, S.; Adinolfi, V.; Xu, J.; Li, M.; Kirmani, A. R.; Sun, J.; Minor, J.; Kemp, K. W.; Dong, H.; Rollny, L.; Labelle, A.; Carey, G.; Sutherland, B.; Hill, I.; Amassian, A.; Liu, H.; Tang, J.; Bakr, O. M.; Sargent, E. H. *Nat. Mater.* **2014**, *13*, 822.

(4) Ellingson, R. J.; Beard, M. C.; Johnson, J. C.; Yu, P.; Micic, O. I.; Nozik, A. J.; Shabaev, A.; Efros, A. L. *Nano Lett.* **2005**, *5*, 865–871.

(5) Urban, J. J. *Nat. Nanotechnol.* **2015**, *10*, 997–1001.

(6) Choi, J.-H.; Wang, H.; Oh, S. J.; Paik, T.; Sung, P.; Sung, J.; Ye, X.; Zhao, T.; Diroll, B. T.; Murray, C. B.; Kagan, C. R. *Science* **2016**, *352*, 205–208.

(7) Choi, J. H.; Fafarman, A. T.; Oh, S. J.; Ko, D. K.; Kim, D. K.; Diroll, B. T. *Nano Lett* **2012**, *12*, 2631–2638.

(8) Liu, Y.; Gibbs, M.; Puthussery, J.; Gaik, S.; Ihly, R.; Hillhouse, H. W.; Law, M. *Nano Lett.* **2010**, *10*, 1960–1969.

(9) Law, M.; Luther, J. M.; Song, Q.; Hughes, B. K.; Perkins, C. L.; Nozik, A. J. *J. Am. Chem. Soc.* **2008**, *130*, 5974–5985.

(10) Li, H.; Zhitomirsky, D.; Dave, S.; Grossman, J. C. *ACS Nano* **2016**, *10*, 606–614.

(11) Treml, B. E.; Savitzky, B. H.; Tirmzi, A. M.; Dasilva, J. C.; Kourkoutis, L. F.; Hanrath, T. *ACS Appl. Mater. Interfaces* **2017**, *9*, 13500–13507.

(12) Sandeep, C. S. S.; Azpiroz, J. M.; Evers, W. H.; Boehme, S. C.; Moreels, I.; Kinge, S.; Siebbeles, L. D. A.; Infante, I.; Houtepen, A. J. *ACS Nano* **2014**, *8*, 11499–11511.

(13) Baumgardner, W. J.; Whitham, K.; Hanrath, T. *Nano Lett.* **2013**, *13*, 3225–3231.

(14) Skinner, B.; Chen, T.; Shklovskii, B. I. *Phys. Rev. B* **2012**, *85*, 205316.

(15) Shklovskii, B. I.; Efros, A. L. *Electronic Properties of Doped Semiconductors*; Springer-Verlag: Berlin; New York, 1984.

(16) Efros, A. L.; Shklovskii, B. I. *J. Phys. C* **1975**, *8*, 49–51.

(17) Chen, T. Electrical Transport in Thin Films of Doped Silicon Nanocrystals, Ph.D. Dissertation, University of Minnesota, Minneapolis, MN, 2015.

(18) Chen, T.; Reich, K. V; Kramer, N. J.; Fu, H.; Kortshagen, U. R.; Shklovskii, B. I. *Nat. Mater.* **2016**, *15*, 299–303.

(19) Knight, M. W.; King, N. S.; Liu, L.; Everitt, H. O.; Nordlander, P. *ACS Nano* **2014**, *8*, 834–840.

(20) Link, S.; El-sayed, M. A. *J. Phys. Chem B* **1999**, *103*, 4212–4217.

(21) Manthiram, K.; Alivisatos, A. P. *J. Am. Chem. Soc.* **2012**, *8*, 8–11.

(22) Kanehara, M.; Koike, H.; Yoshinaga, T.; Teranishi, T. *J. Am. Chem. Soc.* **2009**, *131*, 17736–17737.

(23) Luther, J. M.; Jain, P. K.; Ewers, T.; Alivisatos, A. P. *Nat. Mater.* **2011**, *10*, 361–366.

(24) Gordon, T. R.; Paik, T.; Klein, D. R.; Naik, G. V.; Caglayan, H.; Boltasseva, A.; Murray, C. B. *Nano Lett.* **2013**, *13*, 2857–2863.

(25) Buonsanti, R.; Llordes, A.; Aloni, S.; Helms, B. A.; Milliron, D. J. *Nano Lett.* **2011**, *11*, 4706–4710.

(26) Rowe, D. J.; Jeong, J. S.; Mkhoyan, K. A.; Kortshagen, U. R. *Nano Lett.* **2013**, *13*, 1317–1322.

(27) Kreibig, U.; Vollmer, M. *Optical properties of metal clusters*; Springer, 1995.

(28) Bohren, C. F.; Huffman, D. R. In *Absoprtion and Scattering of Light by Small Particles*; Wiley and Sons, 1983; pp 130–157.

(29) Agrawal, A.; Johns, R. W.; Milliron, D. J. *Annu. Rev. Mater. Res.* **2017**, *47*, 1.

(30) Willets, K. A.; Duyne, R. P. Van. *Annu. Rev. Phys. Chem.* **2007**, No. 58, 267.

(31) Wang, Y.; Runnerstrom, E. L.; Milliron, D. J. *Annu. Rev. Chem. Biomol. Eng.* **2016**, *7*, 283.

(32) Kim, J.; Ong, G. K.; Wang, Y.; Leblanc, G.; Williams, T. E.; Mattox, T. M.; Helms, B. A.; Milliron, D. J. *Nano Lett.* **2015**, *15*, 5574.

(33) Ellmer, K. *J. Phys. D Appl. Phys.* **2001**, *34*, 3097–3108.

(34) Liu, D.; Kelly, T. L. *Nat. Photonics* **2013**, *8*, 133–138.

(35) Kortshagen, U. *J. Phys. D. Appl. Phys.* **2009**, *42*, 113001.

(36) Kortshagen, U. R.; Sankaran, R. M.; Pereira, R. N.; Girshick, S. L.; Wu, J. J.; Aydil, E. S. *Chem. Rev* **2016**, *116*, 11061.

(37) Rao, N. P.; Tymiak, N.; Blum, J.; Neuman, A.; Lee, H. J.; Girshick, S. L.; McMurry, P. H.; Heberlein, J. *J. Aerosol Sci.* **1998**, *29*, 707–720.

(38) Holman, Z. C.; Kortshagen, U. R. *Nanotechnology* **2010**, *21*, 335302.

(39) Thimsen, E.; Johnson, M.; Zhang, X.; Wagner, A. J.; Mkhoyan, K. A.; Kortshagen, U. R.; Aydil, E. S. *Nat. Commun.* **2014**, *5*, 5822.

(40) Rowe, D. J.; Kortshagen, U. R. *APL Mater.* **2014**, *2*, 22104.

(41) Kramer, N. J.; Schramke, K. S.; Kortshagen, U. R. *Nano Lett.* **2015**, *15*, 5597.

(42) Wang, T.; Radovanovic, P. V. *J. Phys. Chem. C* **2011**, *115*, 406–413.

(43) Lounis, S. D.; Runnerstrom, E. L.; Bergerud, A.; Nordlund, D.; Milliron, D. J. *J. Am. Chem. Soc.* **2014**, *136*, 7110–7116.

(44) Trizio, L. De; Schimpf, A. M.; Llordes, A.; Gamelin, D. R.; Simonutti, R.; Milliron, D. J. *Chem. Mater.* **2013**, *25*, 3383–3390.

(45) Schimpf, A. M.; Ochsenbein, S. T.; Buonsanti, R.; Milliron, D. J.; Gamelin, D. R. *Chem Commun.* **2012**, *48* (75), 9352–9354.

(46) Della Gaspera, E.; Bersani, M.; Cittadini, M.; Guglielmi, M.; Pagani, D.; Noriega, R.; Mehra, S.; Salleo, A.; Martucci, A. *J. Am. Chem. Soc.* **2013**, *135*, 3439–3448.

(47) Runnerstrom, E. L.; Llordés, A.; Lounis, S. D.; Milliron, D. J. *Chem. Commun.* **2014**, *50*, 10555.

(48) Clavero, C. *Nat. Photonics* **2014**, *8*, 95–103.

(49) Das, N. C. *J. Appl. Phys.* **2011**, *110*, 46101.

(50) Kundu, J.; Le, F.; Nordlander, P.; Halas, N. J. *Chem. Phys. Lett.* **2008**, *452*, 115–119.

(51) Schimpf, A. M.; Thakkar, N.; Gunthardt, C. E.; Masiello, D. J.; Gamelin, D. R. *ACS Nano* **2014**, *8*, 1065–1072.

(52) Norris, D. J.; Efros, A. L.; Erwin, S. C. *Science (80-.).* **2008**, *319*, 1776–1779.

(53) Erwin, S. C.; Zu, L.; Haftel, M. I.; Efros, A. L.; Kennedy, T. a; Norris, D. J. *Nature* **2005**, *436*, 91–94.

(54) Buonsanti, R.; Milliron, D. J. *Chem. Mater.* **2013**, *25*, 1305–1317.

(55) Vlaskin, V. A.; Barrows, C. J.; Erickson, C. S.; Gamelin, D. R. *J. Am. Chem. Soc.* **2013**, *135*, 14380.

(56) Lu, J. G.; Fujita, S.; Kawaharamura, T.; Nishinaka, H.; Kamada, Y.; Ohshima, T.; Ye, Z. Z.; Zeng, Y. J.; Zhang, Y. Z.; Zhu, L. P.; He, H. P.; Zhao, B. H. *J. Appl. Phys.* **2007**, *101*, 83705.

(57) Mendelsberg, R. J.; Garcia, G.; Li, H.; Manna, L.; Milliron, D. J. *J. Phys. Chem. C* **2012**, *116*, 12226–12231.

(58) Ghosh, S. K.; Pal, T. *Chem. Rev.* **2007**, *107*, 4797–4862.

(59) Halperin, W. P. *Rev. Mod. Phys.* **1986**, *58*, 533–606.

(60) Kreibig, U.; Genzel, L. *Surf. Sci.* **1985**, *156*, 678–700.

(61) Halas, N. J.; Lal, S.; Chang, W.; Link, S.; Nordlander, P. *Chem. Rev.* **2011**, *111*, 3913–3961.

(62) Tame, M. S.; Mcenery, K. R.; Özdemir, Ş. K.; Lee, J.; Maier, S. A.; Kim, M. S. *Nat. Phys.* **2013**, *9*, 329–340.

(63) Scholl, J. A.; Koh, A. L.; Dionne, J. A. *Nature* **2012**, *483*, 421–427.

(64) Zhang, H.; Kulkarni, V.; Prodan, E.; Nordlander, P.; Govorov, A. O. *J. Phys. Chem. C* **2014**, *118*, 16035.

(65) Kramer, N. J.; Anthony, R. J.; Mamunuru, M.; Aydil, E. S.; Kortshagen, U. R. *J. Phys. D. Appl. Phys.* **2014**, *47*, 75202.

(66) Norman, V. J. *Aust. J. Chem.* **1969**, *22*, 325–329.

(67) Vegard, L. *Zeitschrift für Phys.* **1921**, *1*, 17–26.

(68) Bryan, J. D.; Gamelin, D. R. **2005**, *54*, 47–126.

(69) Beaulac, R.; Archer, P. I.; Ochsenbein, S. T.; Gamelin, D. R. *Adv. Funct. Mater.* **2008**, *18*, 3873–3891.

(70) Schwartz, D. a; Norberg, N. S.; Nguyen, Q. P.; Parker, J. M.; Gamelin, D. R. *J. Am. Chem. Soc.* **2003**, *125*, 13205–13218.

(71) Yung, I. C.; Jenq, G. D. *Mater. Chem. Phys.* **1991**, *27*, 427–439.

(72) Roberts, N.; Warren, W. W. *Phys. Rev. B* **1998**, *57*, 5734–5741.

(73) Kovalenko, M. V.; Scheele, M.; Talapin, D. V. *Science (80-.).* **2009**, *324*, 1417.

(74) Borchert, H.; Shevchenko, E. V; Robert, A.; Mekis, I.; Kornowski, A.; Gru, G.; Weller, H. *Langmuir* **2005**, *21*, 1931–1936.

(75) Lan, X.; Voznyy, O.; Garcia De Arquer, F. P.; Liu, M.; Xu, J.; Proppe, A. H.; Walters, G.; Fan, F.; Tan, H.; Liu, M.; Yang, Z.; Hoogland, S.; Sargent, E. H. *Nano Lett.* **2016**, *16*, 4630–4634.

(76) Zhao, T.; Goodwin, E. D.; Guo, J.; Wang, H.; Diroll, B. T.; Murray, C. B.; Kagan, C. R. *ACS Nano* **2016**, *10*, 9267–9273.

(77) Ibáñez, M.; Luo, Z.; Genç, A.; Piveteau, L.; Ortega, S.; Cadavid, D.; Dobrozhan, O.; Liu, Y.; Nachtegaal, M.; Zebarjadi, M.; Arbiol, J.; Kovalenko, M. V.; Cabot, A. *Nat. Commun.* **2016**, *7*, 10766.

(78) Kovalenko, M. V.; Spokoyny, B.; Lee, J. S.; Scheele, M.; Weber, A.; Perera, S.; Landry, D.; Talapin, D. V. *J. Am. Chem. Soc.* **2010**, *132*, 6686–6695.

(79) Swisher, S. L.; Volkman, S. K.; Subramanian, V. *ACS Appl. Mater. Interfaces* **2015**, *7*, 10069–10075.

(80) Treml, B. E.; Robbins, A. B.; Whitham, K.; Smilgies, D. M.; Thompson, M. O.; Hanrath, T. *ACS Nano* **2015**, *9*, 4096–4102.

(81) Lanigan, D.; Thimsen, E. *ACS Nano* **2016**, *10*, 6744–6752.

(82) Thimsen, E.; Johnson, M.; Zhang, X.; Wagner, A. J.; Mkhoyan, K. A.; Kortshagen, U. R.; Aydil, E. S. *Nat. Commun.* **2014**, *5*, 5822.

(83) Oh, S. J.; Berry, N. E.; Choi, J. H.; Gaulding, E. A.; Lin, H.; Paik, T.; Diroll, B. T.; Muramoto, S.; Murray, C. B.; Kagan, C. R. *Nano Lett.* **2014**, *14*, 1559–1566.

(84) Beloborodov, I. S.; Lopatin, A. V.; Vinokur, V. M.; Efetov, K. B. *Rev. Mod. Phys.* **2007**, *79*, 469–518.

(85) Matveev, K. A. *Phys. Rev. B.* 1995, pp 1743–1751.

(86) Brochen, S.; Feuillet, G.; Santailler, J.; Obrecht, R.; Lafossas, M.; Ferret, P.; Chauveau, M.; Pernot, J. *J. Appl. Phys.* **2017**, *121*, 95704.

(87) Waffenschmidt, S.; Pfleiderer, C.; Löhneysen, H. V. *Phys. Rev. Lett.* **1999**, *83*, 3005–3008.

(88) Bogdanovich, S.; Sarachik, M. P.; Bhatt, R. N. *Phys. Rev. Lett.* **2001**, *87*, 129701.

(89) Dobrosavljevic, Vladimir; Trivedi, Nandini; Valles Jr., J. M. *Conductor-Insulator Quantum Phase Transitions*; Oxford University Press: Oxford, 2012.

(90) Greenberg, B. L.; Ganguly, S.; Held, J. T.; Kramer, N. J.; Mkhoyan, K. A.; Aydil, E. S.; Kortshagen, U. R. *Nano Lett.* **2015**, *15*, 8162–8169.

(91) Williams, B. A.; Smeaton, M. A.; Holgate, C. S.; Trejo, N. D.; Francis, L. F.; Aydil, E. S. *J. Vac. Sci. Technol. A* **2016**, *34*, 51204.

(92) Dharmadasa, R.; Lavery, B.; Dharmadasa, I. M.; Druffel, T. *ACS Appl. Mater. Interfaces* **2014**, *6*, 5034–5040.

(93) Perelaer, J.; Abbel, R.; Wünscher, S.; Jani, R.; Van Lammeren, T.; Schubert, U. S. *Adv. Mater.* **2012**, *24*, 2620–2625.

(94) Colorado, H. A.; Dhage, S. R.; Hahn, H. T. *Mater. Sci. Eng. B* **2011**, *176*, 1161–1168.

(95) Kim, H. S.; Dhage, S. R.; Shim, D. E.; Hahn, H. T. *Appl. Phys. A* **2009**, *97*, 791–798.

(96) Patil, S. A.; Hwang, H.-J.; Yu, M.-H.; Shrestha, N. K.; Kim, H.-S. *RSC Adv.* **2017**, *7*, 6565–6573.

(97) Della Gaspera, E.; Kennedy, D. F.; Van Embden, J.; Chesman, A. S. R.; Gengenbach, T. R.; Weber, K.; Jasieniak, J. J. *Adv. Funct. Mater.* **2015**, *25*, 7263–7271.

(98) Ephraim, J.; Lanigan, D.; Staller, C.; Milliron, D. J.; Thimsen, E. *Chem. Mater.* **2016**, *28*, 5549–5553.

(99) Elam J. W., Routkevitch D., George, S. M. *J. Electrochem. Soc.* **2003**, *150*, G339–G347.

(100) Van De Walle, C. G. *Phys. Rev. Lett.* **2000**, *85*, 1012–1015.

(101) Thomas, D. G. *J. Phys. Chem. Solids* **1957**, *3*, 229–237.

(102) *Sintering Key Papers*; Somiya, S. Moriyoshi, Y., Ed.; Elsevier Science: New York, 1990.

(103) Ashby, M. F. *Acta Metall.* **1974**, *22*, 275–289.

(104) Francis, L. F. In *Materials Processing - A Unified Approach to Processing of Metals, Ceramics and Polymers*; Elsevier: London, 2016; pp 343–414.

(105) Groner, M. D.; Fabreguette, F. H.; Elam, J. W.; George, S. M. *Chem. Mater.* **2004**, *16*, 639–645.

(106) Melnick, D. A. *J. Chem. Phys.* **1957**, *26*, 1136–1146.

(107) Doerffler, W.; Hauffe, K. *J. Catal.* **1964**, *3*, 156–170.

(108) Shapira, Y.; Cox, S. M.; Lichtman, D. *Surf. Sci.* **1976**, *54*, 43–59.

(109) Gankanda, A.; Cwiertny, D. M.; Grassian, V. H. *J. Phys. Chem. C* **2016**, *120*, 19195–19203.

(110) Schlur, L.; Carton, A.; Pourroy, G. *Chem. Commun.* **2015**, *51*, 3367–3370.

(111) Kolodziejczak-Radzimska, A.; Jesionowski, T. *Materials (Basel).* **2014**, *7*, 2833–2881.

(112) Zeleňák, V.; Vargová, Z.; Györyová, K. *Spectrochim. Acta. Mol. Biomol. Spectrosc.* **2007**, *66*, 262–272.

(113) Noei, H.; Qiu, H.; Wang, Y.; Löffler, E.; Wöll, C.; Muhler, M. *Phys. Chem. Chem. Phys.* **2008**, *10*, 7092–7097.

(114) Zhang, X.; Manno, M.; Baruth, A.; Johnson, M.; Aydil, E. S.; Leighton, C. *ACS Nano* **2013**, *7*, 2781–2789.

(115) Gal'perin, Y. M.; German, E. P.; Karpov, V. G. *Sov.Phys. JETP* **1991**, *72*, 193–200.

(116) Mendelsberg, R. J.; Garcia, G.; Milliron, D. J. *J. Appl. Phys.* **2012**, *111*, 63515.

(117) Madelung, O. *Semiconductors--Basic Data*, 2nd rev. e.; Springer: Berlin; New York, 1996.

(118) Sievers, A. J. *Opt. Commun.* **1994**, *109*, 71–74.

(119) Noh, J.-Y.; Kim, H.; Kim, Y.-S.; Park, C. H. *J. Appl. Phys.* **2013**, *113*, 153703.

(120) Schimpf, A. M.; Gunthardt, C. E.; Rinehart, J. D.; Mayer, J. M.; Gamelin, D. R. *J. Am. Chem. Soc.* **2013**, *135*, 16569–16577.

(121) Zabrodskii, A. G.; Zinov'eva, K. N. *Sov. Phys. JETP* **1984**, *59*, 425–433.

(122) Sondhi, S. L.; Girvin, S. M.; Carini, J. P.; Shahar, D. *Rev. Mod. Phys.* **1997**, *69*, 315–333.

(123) McMillan, W. L. *Phys. Rev. B* **1981**, *24*, 2739–2743.

(124) Lee, M.; Massey, J. G.; Nguyen, V. L.; Shklovskii, B. I. *Phys. Rev. B* **1999**, *60*, 1582–1591.

(125) Reich, K. V.; Shklovskii, B. I. *ACS Nano* **2016**, *10*, 10267–10274.

(126) Fu, H.; Reich, K. V.; Shklovskii, B. I. *Phys. Rev. B* **2016**, *93*, 125430.

(127) Borchert, H.; Shevchenko, E. V.; Robert, A.; Mekis, I.; Kornowski, A.; Grübel, G.; Weller, H. *Langmuir* **2005**, *21*, 1931–1936.

(128) Husmann, A. A.; Jin, D. S.; Zastavker, Y. V; Rosenbaum, T. F.; Yao, X.; Honig, J. M. *Science (80-.).* **2017**, *274*, 1874–1876.

(129) Roy, A. S.; Hoekstra, A. F. T.; Rosenbaum, T. F.; Griessen, R. *Phys. Rev. Lett.* **2002**, *89*, 276402.

(130) zum Felde, U.; Haase, M.; Weller, H. *J. Phys. Chem B* **2000**, *104*, 9388–9395.

(131) Kharitonov, M. Y.; Efetov, K. B. *Phys. Rev. Lett.* **2007**, *99*, 56803.

(132) Patsalas, P.; Logothetidis, S. *J. Appl. Phys.* **2001**, *90*, 4725.

(133) Guler, U.; Suslov, S.; Kildishev, A. V; Boltasseva, A.; Shalaev, V. M. *Nanophotonics* **2015**, *4*, 269–276.

(134) Cortie, M. B.; Giddings, J.; Dowd, A. *Nanotechnology* **2010**, *21*, 115201.

(135) Reinholdt, A.; Pecenka, R.; Pinchuk, A.; Runte, S.; Stepanov, A. L.; Weirich, T. E.; Kreibig, U. *Eur. Phys. J. D* **2004**, *31*, 69–76.

(136) Barragan, A. A.; Ilawe, N. V; Zhong, L.; Wong, B. M.; Mangolini, L. *J. Phys. Chem. C* **2017**, *121*, 2316.

(137) Quinten, M. *Appl. Phys. B* **2001**, *73*, 317–326.

(138) Guler, U.; Naik, G. V; Boltasseva, A.; Shalaev, V. M.; Kildishev, A. V. *Appl. Phys. B* **2012**, *107*, 285–291.

(139) Naldoni, A.; Guler, U.; Wang, Z.; Marelli, M.; Malara, F.; Meng, X.; Besteiro, L. V; Govorov, A. O.; Kildishev, A. V; Boltasseva, A.; Shalaev, V. M. *Adv. Opt* **2017**, *5*, 1601031.

(140) Ishii, S.; Shinde, S. L.; Jevasuwan, W.; Fukata, N.; Nagao, T. *ACS Photonics* **2016**, *3*, 1552.

(141) Loureiro, J.; Neves, N.; Barros, R.; Mateus, T.; Santos, R.; Filonovich, S.; Reparaz, S.; Sotomayor-Torres, C. M.; Wyczisk, F.; Divay, L.; Martins, R.; Ferreira, I. *J. Mater. Chem. A* **2014**, *2*, 6649–6655.

(142) Jood, P.; Mehta, R. J.; Zhang, Y.; Peleckis, G.; Wang, X.; Siegel, R. W.; Borca-Tasciuc, T.; Dou, S. X.; Ramanath, G. *Nano Lett.* **2011**, *11*, 4337–4342.

(143) Yang, C.; Souchay, D.; Kneib, M.; Bogner, M.; Wei, H. M.; Lorenz, M.; Oeckler, O.; Benstetter, G.; Fu, Y. Q.; Grundmann, M. *Nat. Commun.* **2017**, *8*, 16076.

(144) Gautam, D.; Engenhorst, M.; Schilling, C.; Schierning, G.; Schmechel, R.; Winterer, M. *J. Mater. Chem. A* **2015**, *3*, 189–197.

(145) Musselman, K. P.; Uzoma, C. F.; Miller, M. S. *Chem Mater* **2016**, *28*, 8443.

(146) Poodt, P.; Cameron, D. C.; Dickey, E.; George, S. M.; Kuznetsov, V.; Parsons, G. N.; Sundaram, G.; Vermeer, A.; Cameron, D. C.; Dickey, E.; George, S. M.; Roozeboom, F.; Sundaram, G.; Vermeer, A. *J. Vac. Sci. Technol. A* **2012**, *30*, 10802.

(147) Sharma, K.; Routkevitch, D.; Varaksa, N.; George, S. M. *J. Vac. Sci. Technol. A* **2016**, *34*, 01A146.

(148) Jin, W.; Kleijn, C. R.; Ruud van Ommen, J. *J. Vac. Sci. Technol. A* **2017**, *35*, 01B116.

(149) Czanderna, A. W.; Pern, F. J. *Sol. Energy Mater. Sol. Cells* **1996**, *43*, 101–181.

(150) Kanazawa, S.; Kogoma, M.; Moriwaki, T.; Okazaki, S. *J. Phys. Chem. Lett.* **1988**, *21*, 838.

(151) Massines, F.; Rabehi, A.; Decomps, P.; Gadri, R. Ben; Ségur, P.; Mayoux, C. *J. Appl. Phys.* **1998**, *83*, 2950.

(152) Staack, D.; Farouk, B.; Gutsol, A.; Fridman, A. *Plasma Sources Sci. Technol.* **2005**, *14*, 700.

(153) Roth, J. R.; Rahel, J.; Dai, X.; Sherman, D. M. *J. Phys. D Appl. Phys.* **2005**, *38*, 555.

(154) Beaulieu, A. J. *Appl. Phys. Lett.* **1970**, *16*, 504.

(155) Tiffany, W. B.; Targ, R.; Foster, J. D. *Appl. Phys. Lett.* **1969**, *15*, 91.

(156) Watanabe, K.; Kashiwabara, S.; Sawai, K.; Toshima, S.; Fujimoto, R. *J. Appl. Phys.* **1983**, *54*, 1228.

(157) Abramski, K. M.; Colley, A. D.; Baker, H. J.; Hall, D. A. *Appl. Phys. Lett.* **1989**, *54*, 1833.

(158) Benard, D. J.; Mcdermott, W. E.; Pchelkin, N. R.; Bousek, R. R. *Appl. Phys. Lett.* **1979**, *34*, 40.

(159) Sato, S.; Taniwaki, M. *Appl. Phys. B* **1992**, *61*, 621.

(160) Laflamme, A. K. *Rev. Sci. Instrum.* **1970**, *41*, 1578.

(161) Shi, J. J.; Liu, D. W.; Kong, M. G. *IEEE Trans. Plasma Sci.* **2007**, *35*, 137–142.

(162) Kunhardt, E. E. *IEEE Trans. Plasma Sci.* **2000**, *28*, 189–200.

(163) Nozaki, T.; Sasaki, K.; Ogino, T.; Asahi, D.; Okazaki, K. *Nanotechnology* **2007**, *18*, 235603.

(164) Palmer, A. J. *Appl. Phys. Lett.* **1974**, *25*, 138.

(165) Norberg, N. S.; Gamelin, D. R. *J. Phys. Chem B* **2005**, *109*, 20810–20816.

(166) Felbier, P.; Yang, J.; Theis, J.; Liptak, R. W.; Wagner, A.; Lorke, A.; Bacher, G.; Kortshagen, U. *Adv. Funct. Mater.* **2014**, *24*, 1988–1993.

(167) Zhang, L.; Yin, L.; Wang, C.; Qi, Y.; Xiang, D. *J. Phys. Chem. C* **2010**, *114*, 9651–9658.

(168) Kaftelen, H.; Ocakoglu, K.; Thomann, R.; Tu, S.; Weber, S.; Erdem, E. *Phys. Rev. B* **2012**, *86*, 14113.

(169) Whitaker, K. M.; Ochsenbein, S. T.; Polinger, V. Z.; Gamelin, D. R. *J. Phys. Chem. C* **2008**, *98195*, 14331–14335.

(170) Cohn, A. W.; Kittilstved, K. R.; Gamelin, D. R. *J. Am. Chem. Soc.* **2012**, *134*, 7937.

(171) Baltrusaitis, J.; Jensen, J. H.; Grassian, V. H. *J. Phys. Chem. B* **2006**, *110*, 12005–12016.

(172) Baltrusaitis, J.; Schuttlefield, J. D.; Zeitler, E.; Jensen, J. H.; Grassian, V. H. *J. Phys. Chem. C* **2007**, *111*, 14870–14880.

(173) Doremus, R. H. *J. Appl. Phys.* **2006**, *100*, 101301.

(174) Nabatame, T.; Yasuda, T.; Nishizawa, M.; Ikeda, M.; Horikawa, T.; Toriumi, A. *Jpn. J. Appl. Phys.* **2003**, *42*, 7205–7208.

Appendix A: Supporting information for chapter 2

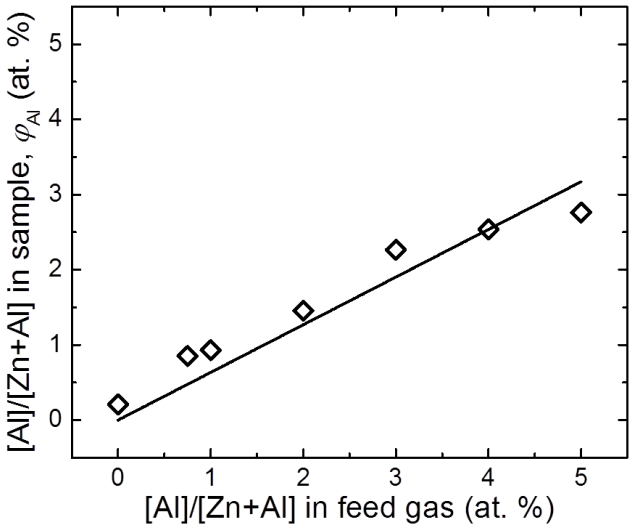

Figure S2.1: Al concentration in thick (~3 μm) films of AZO NCs, φ_{Al}, determined from ICP-MS vs. Al concentration in the feed gas. A linear fit passing through the origin gives a slope of 0.63. Because the thin (~500 nm) films discussed in Chapter 2 do not have adequate mass for direct measurement, we use y = 0.63x as a calibration curve to convert known Al content in the feed gas into φ_{Al}.

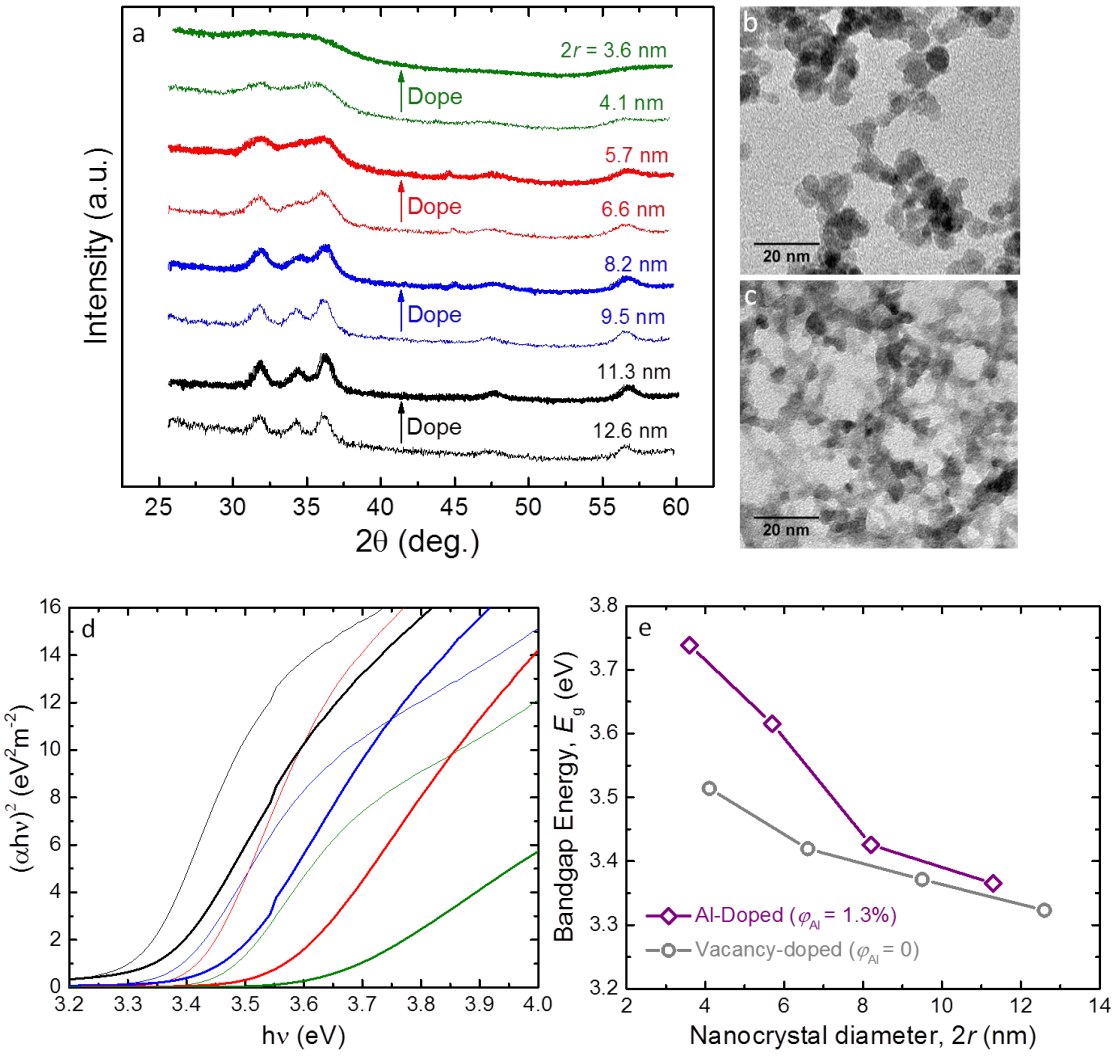

Figure S2.2: (a) XRD patterns corresponding to the FTIR spectra in Figure 2.2. (b) TEM micrographs of the 8.2 nm AZO NCs. (c) TEM micrographs of the 3.6 nm AZO NCs. (d) Tauc plots from corresponding UV-vis spectra. (d) E_g extracted from the Tauc plots vs. φ_{Al}. Blueshifts with decreasing NC diameter are due to quantum confinement. Comparing NCs with $\varphi_{Al} = 0$ to those with $\varphi_{Al} = 1.3\%$, we also observe a blueshift with Al doping due to the Burstein-Moss effect, which confirms that n_e is consistently higher in the Al-doped NCs.

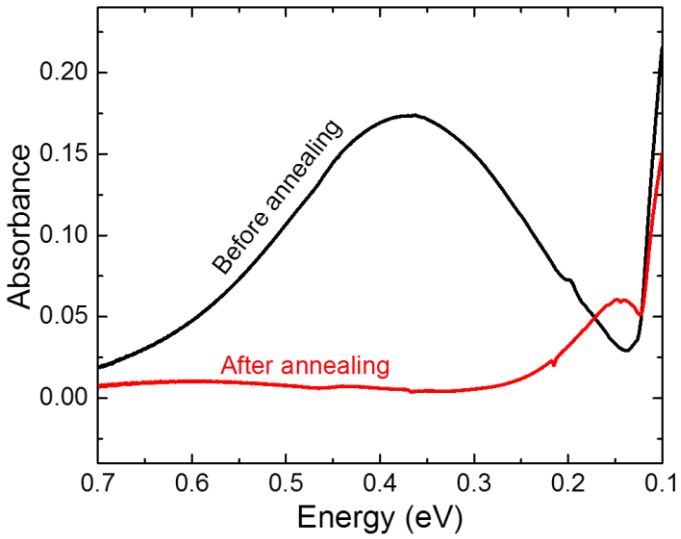

Figure S3.2: A demonstration of the metastability of Al dopants. AZO NCs with φ_{Al} = 1.3% were deposited onto NaCl substrates and, prior to ALD coating, annealed in a tube furnace under 400 SCCM Ar gas flow. The NCs were annealed in three stages: (1) temperature was ramped up over the course of ~45 minutes from room temperature to 625 ºC, (2) temperature was held at 625 ºC for 1 hour, and (3) the furnace was allowed to cool back to room temperature, which took ~3 hours. Over the course of this treatment, the diffusion length of an Al atom within the ZnO lattice is expected to be on the order of 1 to 10 nm. The annealed films exhibit a significantly redshifted LSPR, indicating that most Al dopants were metastable and diffused out of substitutional lattice sites. That this post-annealing LSPR energy is slightly below the typical value for $\varphi_{Al} = 0$ suggests that some oxygen vacancies may have been eliminated as well, but that effect alone could not account for a redshift of this magnitude.

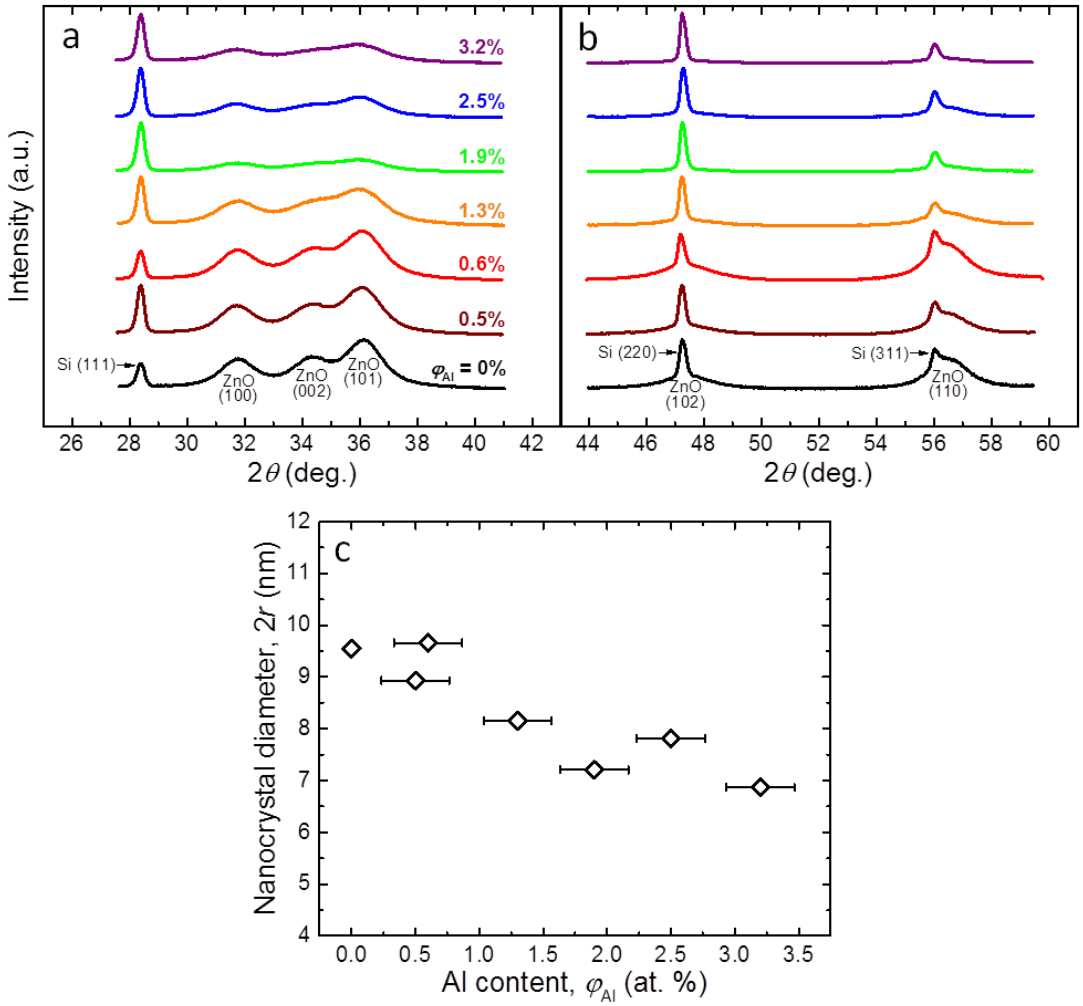

Figure S2.4: (a) Representative low-angle XRD patterns of AZO NCs mixed with Si powder used to determine the lattice parameters *a* and *c* shown in Figure 2.4b (b) Corresponding high-angle XRD patterns. In both sets of patterns, with increasing φ_{Al}, the ZnO peaks shift to smaller angles relative to the Si peaks, indicating lattice expansion. (c) NC diameter determined from ZnO XRD peak broadening vs. φ_{Al}.

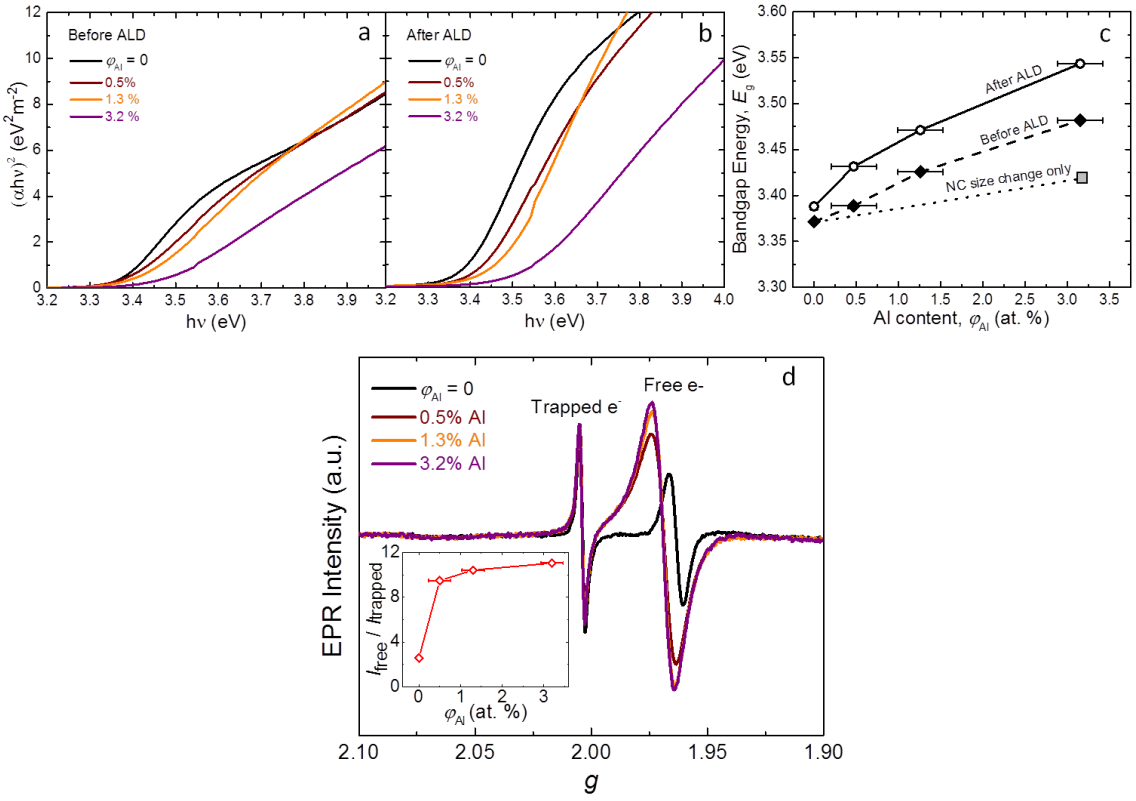

Figure S2.5: (a) Tauc plots from UV-vis spectra of AZO NCs not coated by ALD (NC diameter is 9.5 nm for φ_{Al} = 0 and decreases to ~7 nm with increasing φ_{Al}). (b) Tauc plots from UV-vis spectra of the same films after ALD coating. (c) E_g extracted from the Tauc plots vs. φ_{Al}. To deconvolute the effects of doping and decreasing NC size, we also determined E_g of uncoated ZnO NCs with diameter similar to that of the smallest AZO NCs (6.6 nm), and found that E_g blueshifted to 3.42 eV (represented by the gray square). With increasing φ_{Al}, E_g blueshifts to 3.48 eV for the uncoated NCs (solid diamonds) and to 3.54 eV for the coated NCs (open circles). Interpreting these trends in terms of the Burstein-Moss effect leads to the conclusion that n_e increases with Al doping in the uncoated NCs and increases further in the coated NCs. (d) Corresponding EPR spectra of AZO NC powders (NCs not coated by ALD) normalized to the resonance at g ≈ 2.00. Referring to previous studies of ZnO NCs,[167,168] we assign the resonance at g ≈ 2.00 to electrons trapped on oxygen vacancy sites. Referring to studies of undoped,[169] Mg-doped,[170] and Al-doped ZnO NCs, we assign the resonance which shifts upon doping from g ≈ 1.96 to g ≈ 1.97 to free conduction-band electrons; the increase in g is due to the E_g blueshift[170]. The increase in intensity of this resonance relative to that of the trapped-electron resonance determined by double integration (I_{free} / $I_{trapped}$, inset) confirms that n_e increases with Al doping even in uncoated NCs. The lack of a third resonance indicates that the lattice-expanding defect evinced by Figure 2.4 is diamagnetic.

Appendix B: Supporting information for chapter 3

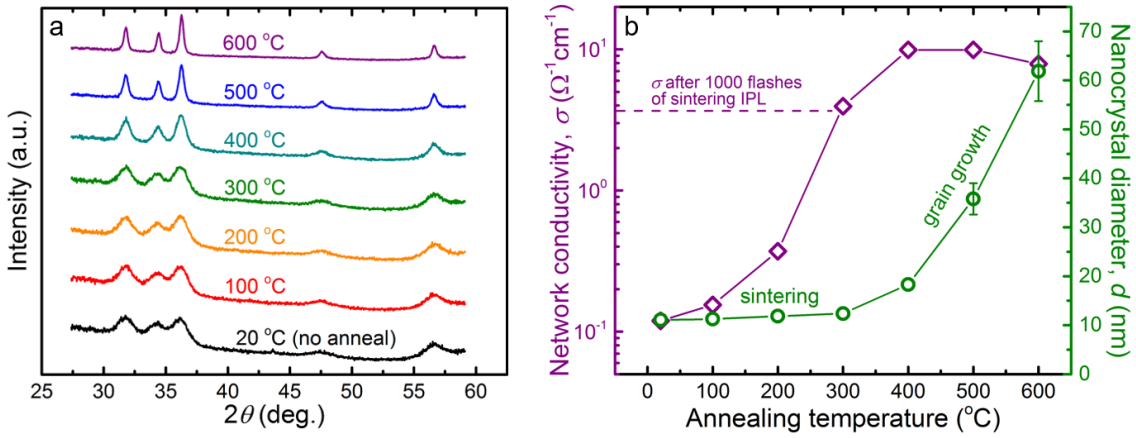

Figure S3.1: ZnO NC networks on glass substrates (for conductivity measurements) and Si substrates (for XRD) were thermally annealed to determine the temperature range in which rapid grain growth occurs. The samples were heated in air for 11 minutes (the duration of a 1000-flash IPL treatment). (a) XRD patterns show the onset of significant grain growth at 400 °C. (b) Right axis: d from the Scherrer formula for spheres.[127] Left axis: room-temperature σ from the Van der Pauw method. At 300 °C, σ increases by a factor of ~30 (and is approximately equal to that of a sample treated with 1000 flashes of sintering IPL), while d remains nearly constant. This is consistent with entering the initial stage of sintering. As discussed in Chapter 3 and shown in Figure S3.3, IPL increases film density only slightly (by ~6%), which is consistent with remaining in the initial stage rather than proceeding to the intermediate densification stage.[104]

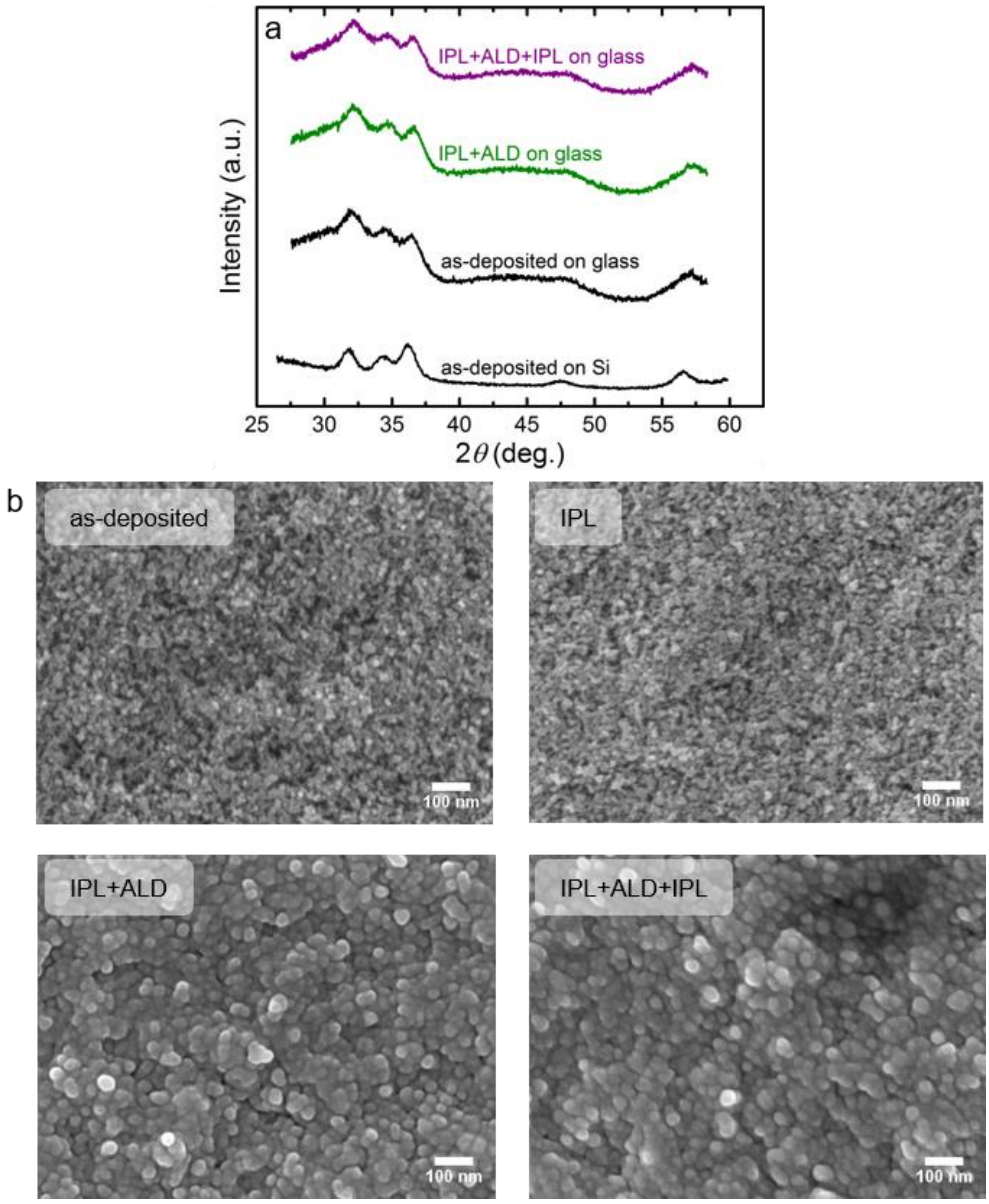

Figure S3.2: (a) XRD patterns of ZnO NCs at various treatment stages. NCs were deposited (black), then sintered by IPL and coated by ALD (green), then photodoped by IPL (purple). These treatments do not significantly change the NC diameter. Here the number of flashes was 1250 at both stages of IPL. Since thermal behavior during IPL is substrate dependent, the substrates used were the same as those of samples that undergo electrical measurements (boro-aluminosilicate glass). To reduce the background signal and facilitate peak fitting, an additional XRD pattern was acquired from as-deposited ZnO NCs on a Si substrate. This is the pattern used to determine via the Scherrer formula for spheres[127] that the average NC diameter is 9.6 ± 0.9 nm. (b) Corresponding plan-view SEM micrographs. Neither IPL before ALD nor IPL after ALD cause significant structural changes visible at this magnification. Scale bars represent 100 nm.

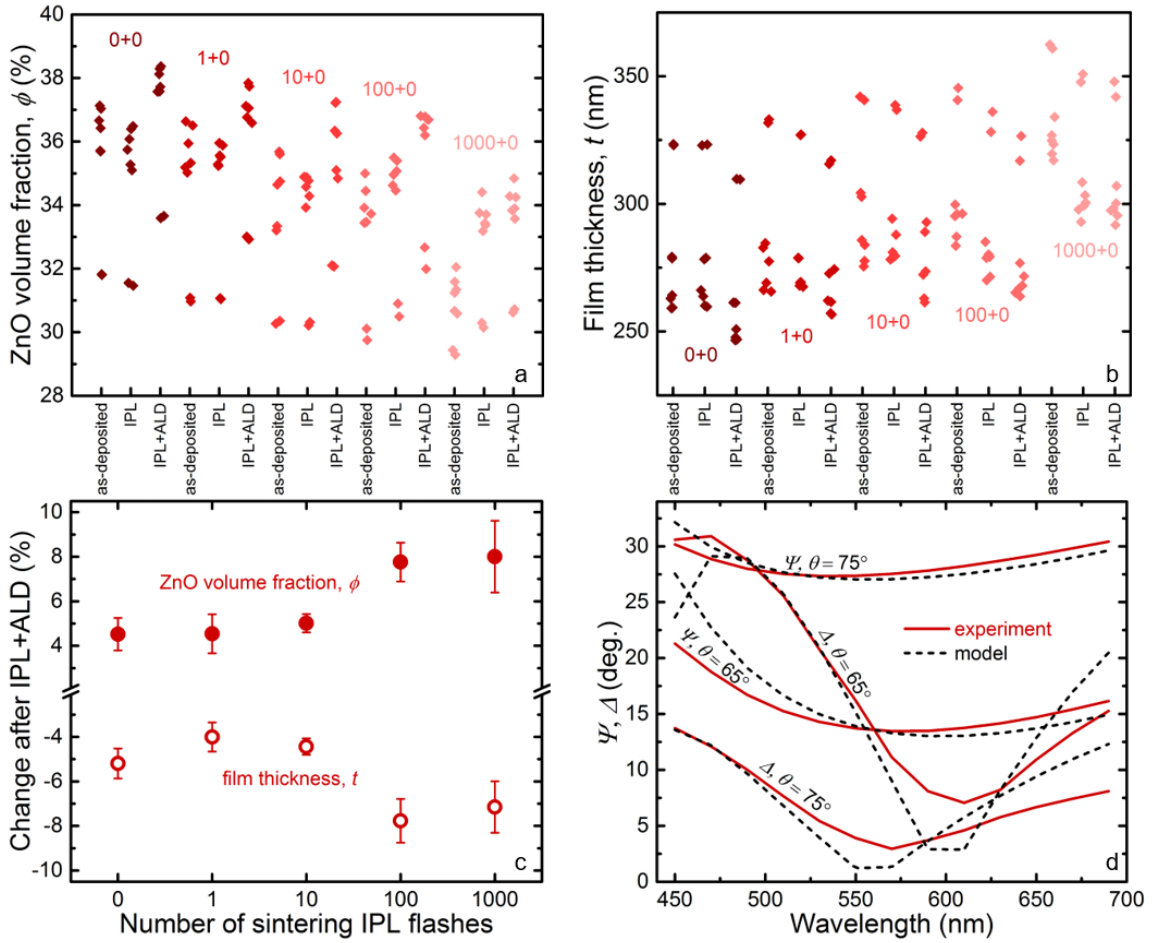

Figure S3.3: (a,b) ZnO volume fraction, ϕ, and film thickness, t, from ellipsometry at various treatment stages. The ϕ values are used to determine the ρ values shown in Figure 3.2. Five ZnO NC films were deposited simultaneously (for five different values of the number of IPL flashes) and each film was measured in eight locations at each treatment stage, so that each data column contains eight points (some points overlap). "ALD" refers to the thermal treatment described in Chapter 3 which simulates the thermal conditions of ALD without Al_2O_3 deposition. The increase in ρ due to sintering during IPL and ALD are computed using pairs of ϕ values measured at the same location of the same sample. Due to statistical fluctuations, some pairs showed a slight decline in ϕ after 10 or fewer IPL flashes; these data are not used in calculating ρ, because the geometrical model does not apply in these cases. See Note 1 for details. We note that the trends in the absolute values of ϕ and t may initially appear inconsistent with sintering (ϕ is lower and t is higher in samples treated with more flashes). In actuality, these trends, as well as scatter within each sample, are due to spatial nonuniformity of the NC deposition which produces variance in *as-deposited* ϕ corresponding to variance in NC packing rather than in ρ. To confirm that this variance in packing does not significantly impact our results, we also applied 1000 IPL flashes and "ALD" to a sample with spatially averaged as-deposited $\phi \approx 34\%$, and found that after treatment, $\rho = 1.5 \pm 0.1$ nm, equal to that of the sample which received the same treatment but had as-deposited $\phi \approx 31\%$. (c) Spatially averaged ϕ and t measured after IPL and ALD and normalized to their as-deposited values. Here sintering due to IPL and ALD is more immediately apparent. (d) Representative ellipsometry data and two-parameter fit of Ψ and Δ used to determine ϕ and t. Fits are produced using the Bruggeman effective medium approximation.

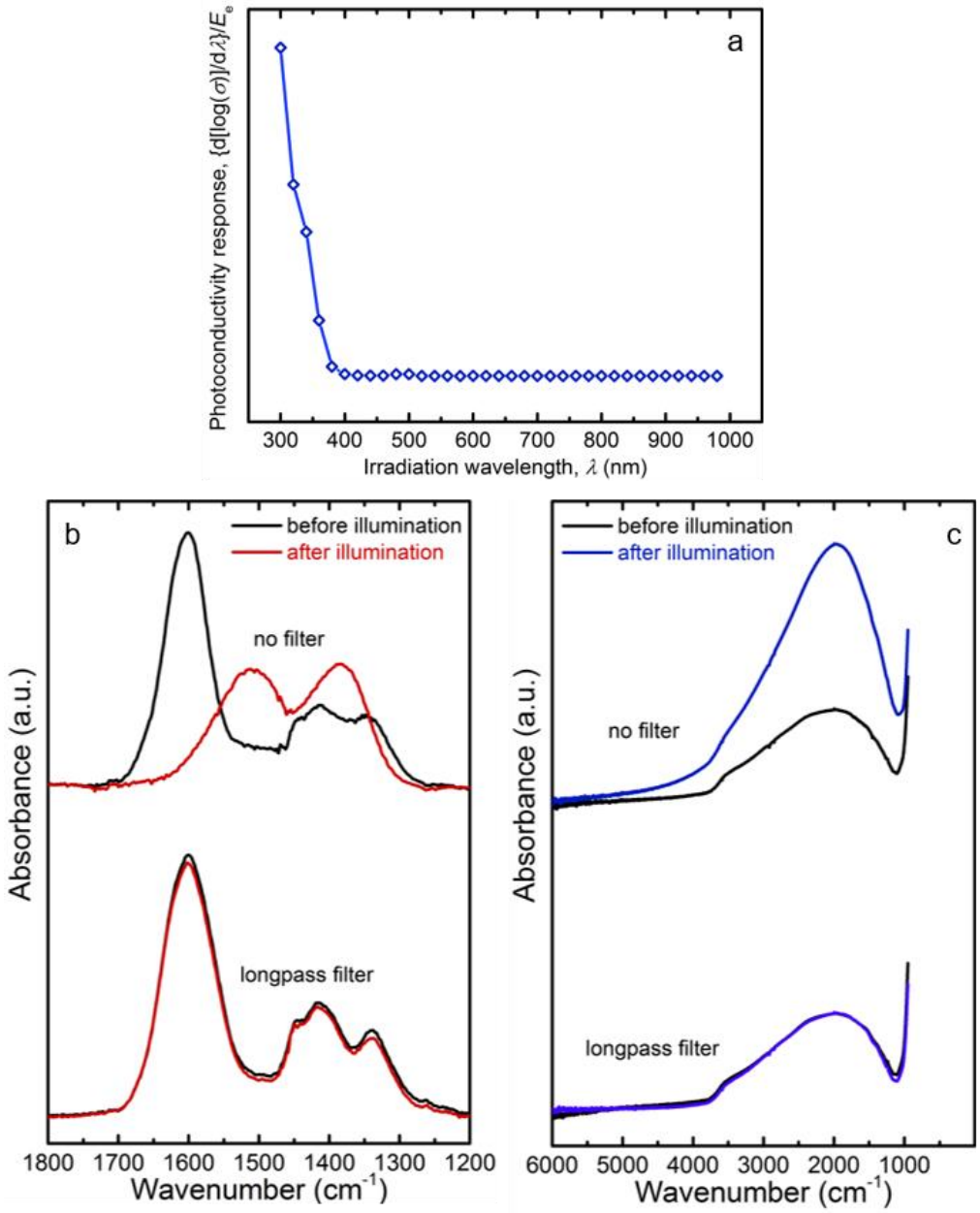

Figure S3.4: Results of low-intensity illumination experiments. ZnO NC networks were irradiated with a xenon arc lamp under ambient conditions at a spectrally integrated surface power density of approximately 200 mW/cm^2 so that they remain close to room temperature. (a) Photoconductivity spectrum of a ZnO NC network acquired after ALD treatment using monochromated lamp emission. (b,c) FTIR spectra before and after illumination, with and without a longpass filter with a cut-on wavelength of 450 nm. The total photon dose is equivalent to 100 flashes of IPL. (b) Carboxylate and related features of an as-deposited sample (no ALD or IPL). Unfiltered light has the same effect as sintering IPL (see Figure 3.3a). Longpass-filtered light has no significant effect. (c) Hydroxyl and LSPR features of samples pre-treated with 1000 flashes of sintering IPL followed by ALD to mimic the doping IPL series. Qualitatively, unfiltered light has the same effects as doping IPL, revealing that photochemical hydroxyl removal and *n* enhancement can occur near room temperature, although quantitatively these effects are diminished (see Note 2 for further discussion).

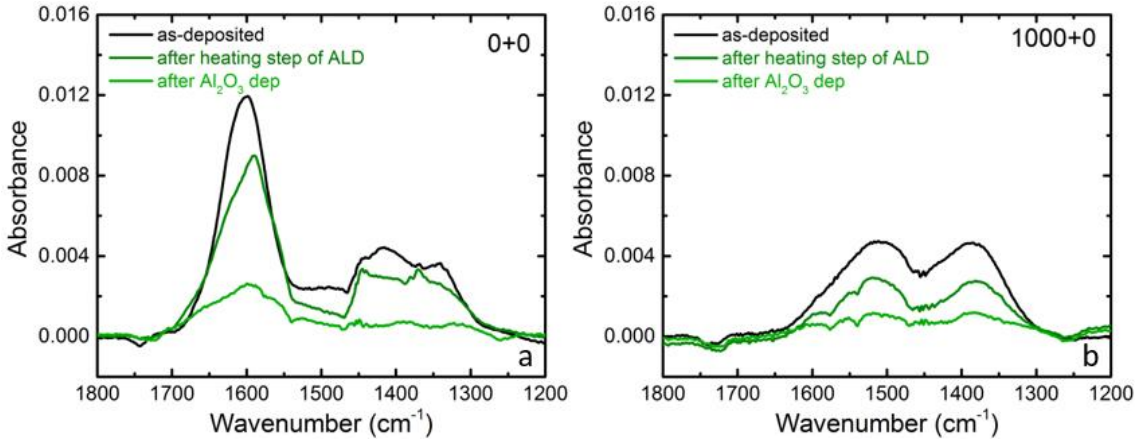

Figure S3.5: Evolution of carboxylate features in FTIR absorption spectra due to ALD. Spectra were acquired before ALD (black), then after the initial heating step of ALD which entails heating at 180 °C under N_2 for 33 minutes (dark green), and then after ALD of 7.7 nm of Al_2O_3 was completed (light green). (a) In the case of no IPL treatment ("0+0"), the as-deposited spectrum shows carboxylate features at 1600 cm^{-1} (asymmetric stretch, $\nu_{as}(COO^-)$) and between 1300 and 1500 cm^{-1} (symmetric stretch, $\nu_s(COO^-)$, among other modes). After the heating step of ALD (during which sintering occurs), the $\nu_{as}(COO^-)$ stretch is shifted to 1591 cm^{-1}, indicating a change in the form of carboxylate binding to the ZnO NC surfaces. A possible explanation of the redshift is a change from ionic monodentate bonding to a covalent bridging configuration, where a carboxylate group is bound to two Zn atoms.[112] Such a configuration could be formed by a carboxylate group binding to two adjacent ZnO NCs during sintering and thus interfering with ρ enhancement. We cannot rule out other transformations (such as ionic monodentate to covalent monodentate), but in any case, the persistence and evolution of the carboxylate features indicate that carboxylate groups play a role in surface chemistry changes during sintering. The carboxylate features also remain after the deposition step of ALD. The blueshift of the $\nu_{as}(COO^-)$ stretch during this stage could be due to another binding reconfiguration and/or interaction between carboxylates and Al_2O_3. (b) In the case of 1000 IPL flashes before ALD ("1000+0"), the carboxylate features are completely removed during IPL. We assign the features at 1512 and 1388 cm^{-1} to carbonate/water complexes, which form from reactions between CO_2 and OH groups on metal oxide surfaces.[109,171,172]

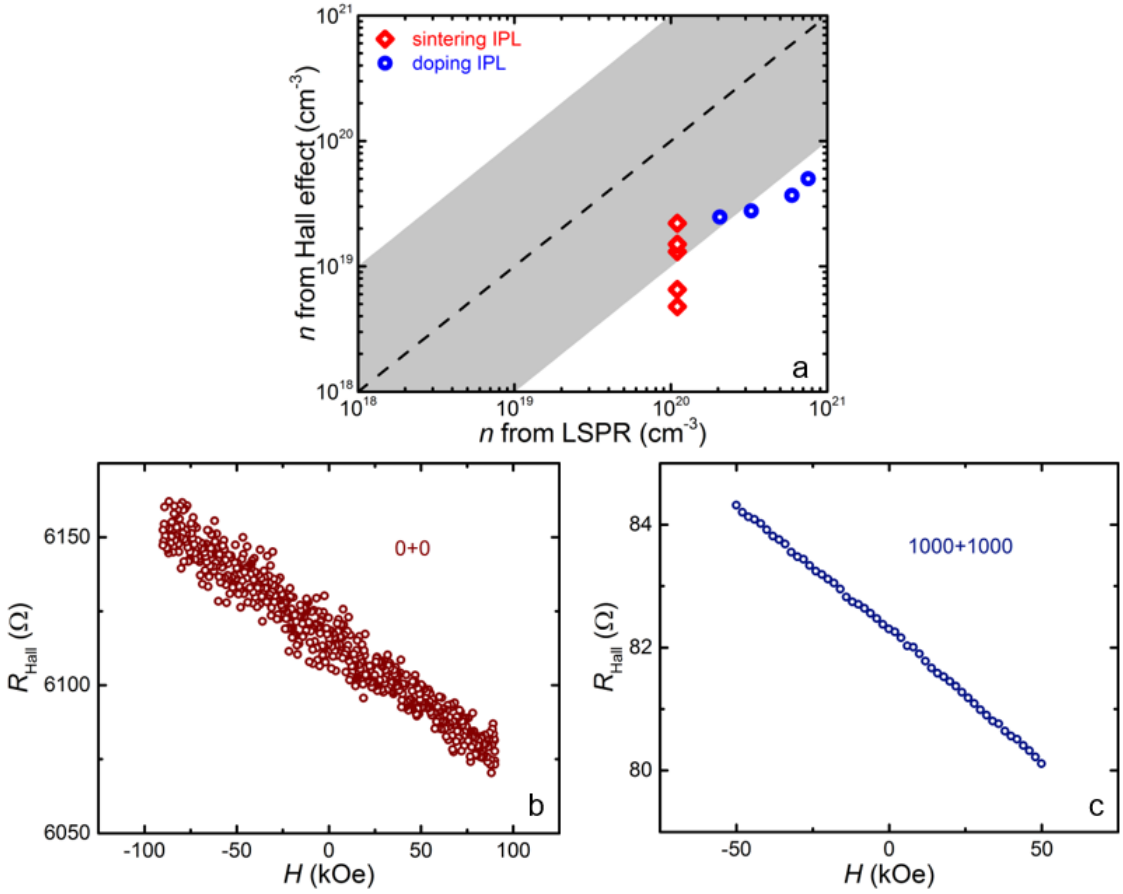

Figure S3.6: (a) *n* from Hall effect measurements vs. *n* from the LSPRs shown in figure 3.3b. The gray region represents agreement within an order of magnitude. (b,c) Hall data from the least and most conductive samples, "0+0" and "1000+1000". For resistive samples such as "0+0", R_{Hall} drifted (decreased) significantly over time at zero field in the low-pressure measurement chamber. The R_{Hall} drift rate, dR/dt, was constant, so we deconvolved dR/dt and dR/dH by sweeping the magnetic field in both directions. Each R_{Hall} value plotted in (b) is an average of the two corresponding values obtained from the two sweeps.

Table S3.1: ρ^3, n, and σ of all samples. ρ^3 is determined by ellipsometry (Figure 3.2), n is determined from the LSPR absorption features in the FTIR spectra (Figure 3.3), and σ is determined by four-point probe measurements using the Van der Pauw geometry (Figure 3.4). Also tabulated are σ of a sample treated with 2000 IPL flashes before ALD and a sample treated with 2000 IPL flashes after ALD. Comparing σ of these samples to σ of the "1000+1000" sample (which also received a total of 2000 flashes) confirms that IPL before ALD and IPL after ALD increase σ by different mechanisms (shown in Chapter 3 to be sintering and doping), and that a combination of the two treatments is necessary for maximizing σ.

sample name	IPL flashes before ALD (sintering IPL)	IPL flashes after ALD (doping IPL)	interparticle contact radius^3, ρ^3 (nm^3)	electron density, n (10^{20} cm^{-3})	network conductivity, σ (Ω^{-1}cm^{-1})
0+0	0	0	1.5 ± 0.3	1.1	3.8×10^{-2}
1+0	1	0	1.5 ± 0.4	1.1	3.7×10^{-2}
10+0	10	0	1.7 ± 0.2	1.1	8.1×10^{-2}
100+0	100	0	3.2 ± 0.4	1.1	8.7×10^{-1}
1000+0	1000	0	3.4 ± 0.8	1.1	3.7×10^{0}
1000+1	1000	1	3.4 ± 0.8	2.1	4.7×10^{0}
1000+10	1000	10	3.4 ± 0.8	3.3	5.7×10^{0}
1000+100	1000	100	3.4 ± 0.8	5.9	1.0×10^{1}
1000+1000	1000	1000	3.4 ± 0.8	7.6	1.8×10^{1}
--	2000	0	--	--	5.0×10^{0}
--	0	2000	--	--	3.6×10^{0}

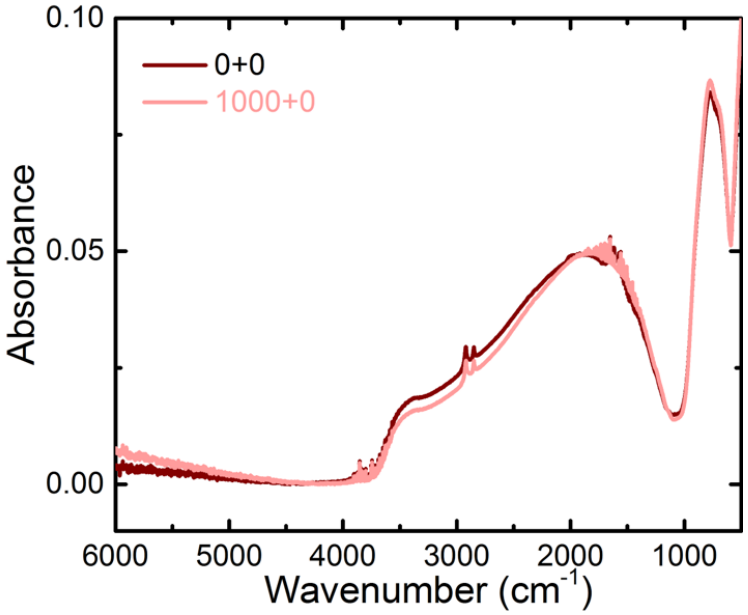

Figure S3.7: FTIR spectra, acquired after ALD, of a sample treated with 1000 flashes of sintering IPL ("1000+0") and a sample not treated with IPL ("0+0"). The sintering IPL has no significant effect on the LSPR, indicating that *n* remains constant.

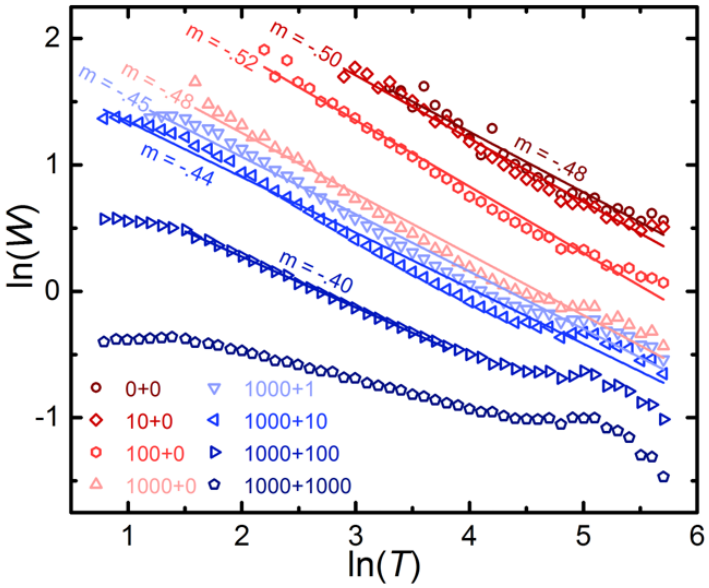

Figure S3.8: Zabrodskii plot of ln W vs. ln T, where $W = d(\ln(\sigma))/d(\ln(T))$. Slopes near 1/2 are consistent with ESVRH. The flattening at low T shown by the two most conductive samples ("1000+100" and "1000+1000") is consistent with a transition to a power law.

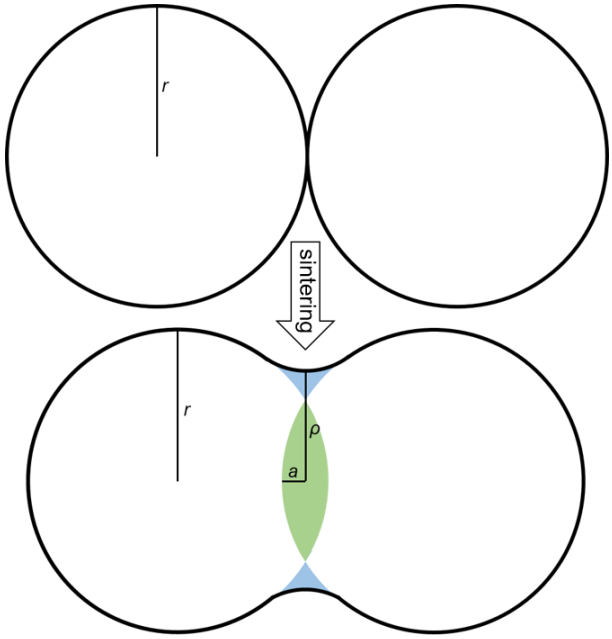

Figure S3.9: Geometrical model used to compute ρ from ϕ.

Note 3.1: Geometrical model used to compute ρ from ϕ.

ZnO volume fractions from ellipsometry, ϕ, are converted to estimates of interparticle contact radii, ρ, using a simple geometrical model. We assume $\rho_0 = 0$, and then we calculate changes in ρ from changes in ϕ. Our model begins with a network of spheres of radius r and packing fraction ϕ_0 that are connected by point contacts. Consider a pair of connected spheres within this network. The initial center-to-center distance is $2r$. During sintering, the packing fraction increases to ϕ and the center-to-center distance decreases to $2(r - a)$, where a and ϕ are related by

$$\frac{\phi}{\phi_0} \approx \left(\frac{r}{r-a}\right)^3 \tag{S3.1}$$

This reduction of center-to-center distance displaces a volume of material (green region), given by

$$V_{\text{disp}} = \frac{2\pi}{3} a^2 (3r - a) \tag{S3.2}$$

Then curvature is minimized when this displaced material takes the form of the solid of revolution obtained by rotating the region bounded by the NC cross-sections and a circle tangent to the NCs (blue region) about the axis connecting the NC centers. The minimum

outer radius of this solid is ρ, which we can find be equating the volume of the solid of revolution, V_{sol}, with V_{disp}, i.e. by equating the volume of the blue region with the volume of the green region. To obtain an expression for V_{sol} we use a Cartesian coordinate system with origin at the midpoint between the NC centers, so that the NC cross-sections have centers at $(\pm(r - a), 0)$, and the circle forming the upper bound of the blue region and tangent to the NCs at the horizontal coordinates $\pm x_{int}$ has radius r_{UB} and center at $(0, k_{UB})$, where

$$r_{UB} = \sqrt{{x_{int}}^2 + \left(k_{UB} - \sqrt{r^2 - (x_{int} + r - a)^2}\right)^2} \tag{S3.3}$$

$$k_{UB} = \sqrt{r^2 - (x_{int} + r - a)^2}\left(1 - \frac{x_{int}}{x_{int} + r - a}\right) \tag{S3.4}$$

Now we equate V_{sol} with V_{disp} and solve for x_{int}:

$$\pi \int_{-x_{int}}^{x_{int}} \left[\left(k_{UB} - \sqrt{{r_{UB}}^2 - x^2}\right)^2 + (x + r - a)^2 - r^2\right] \mathrm{d}x = V_{disp} \tag{S3.5}$$

Finally, ρ is given by

$$\rho = k_{UB} - r_{UB} \tag{S3.6}$$

Note 3.2: Fate of hydroxyls during doping IPL.

FTIR spectra acquired after doping IPL (Figure 3.3b) clearly show elimination of the hydroxyl signal and enhancement of the LSPR signal, but they show no other significant changes. This leaves open the question of the ultimate fate of oxygen and hydrogen atoms after hydroxyl removal. Interactions among hydroxyls, UV photons, and photogenerated electrons/holes may produce a wide variety of chemical species, including neutral OH, atomic O and H, diatomic O_2 and H_2, and H_2O. Broadly speaking, the FTIR spectra allow two possibilities: (1) the species formed are in fact exclusively undetectable via FTIR (IR inactive or active outside the wavenumber range of the measurement) or (2) some or all of the species diffuse out of the film. The latter is perhaps counterintuitive, given that the ZnO NC networks treated with doping IPL are first infilled with Al_2O_3, and that we have proposed that hydroxyl groups are initially

located at or near the ZnO/Al_2O_3 interfaces (so that they interact with charge carriers originating from the ZnO). Still, appreciable diffusion of chemical species out of the films under UV irradiation is a possibility worth considering in more detail.

To understand diffusion through the Al_2O_3-coated ZnO NC networks, it is useful to consider the ALD process by which they are formed. The ALD infilling is a self-limiting process that decreases the porosity of the film until it reaches a value at which the ALD precursors can no longer infiltrate the film under the pulse conditions (temperature = 180 °C, precursor partial pressure ≈ 100 Torr, time = 0.1 s). This minimum porosity was shown to be ~5-10% for ZnO ALD on ZnO NCs by Thimsen *et al*.,[82] and the value for Al_2O_3 ALD is likely similar. Because these pores are what enable ALD precursor infiltration, they likely form continuous or nearly continuous networks from the top to the bottom of the film, i.e. pore networks with a permeability just slightly below that which would enable further deposition under the pulse conditions. These pore networks can therefore later serve as diffusion pathways for species entering and exiting the film. (Indeed, the air stability of these samples is measurably imperfect: whereas conductivity shows no decay after months of storage in the dark under an inert atmosphere, it decays at a rate of ~1% per day under dark ambient conditions, presumably due to room-temperature diffusion of H_2O and/or O_2 into the film.) During IPL, when a molecule is generated at a ZnO/Al_2O_3 interface, the rate-determining step for diffusion out of the film is likely passage through a fairly short length of Al_2O_3 in order to reach a pore network. On average this length is probably no longer than ~7-8 nm, which is the thickness of a 70-cycle Al_2O_3 ALD coating on a flat substrate.

The question then becomes whether, under the irradiation conditions, the diffusion length of a photogenerated species through the Al_2O_3, l, is 7-8 nm. Of particular interest is the low-intensity illumination experiment (Figure S3.4c), in which the film remains close to room temperature. In this experiment, the elapsed time is ~6000 s, and for the sake of argument we can assume that the diffusing species is H_2O. In order to obtain l = 7-8 nm, we require $D_{300K} \approx 10^{-17}$ cm^2/s for H_2O. Generally, diffusion coefficients in Al_2O_3 are measured at temperatures well above 300 K, but still we can use the results of these experiments to gauge plausibility. For H_2O diffusing in polycrystalline Lucalox™

Al_2O_3, ~10^{-17} cm^2/s is the value of D_{600K}.[173] Therefore we require that the activation energy for H_2O diffusion in our Al_2O_3 is approximately half that in Lucalox (assuming comparable D_0). This is in fact not unreasonable, considering that Al_2O_3 grown on ZnO NCs by ALD at 180 °C is amorphous and likely has relatively high densities of coordination defects and impurities due to substrate effects, low growth temperature, and possible chamber contamination. In general, diffusion activation energies vary widely among various forms of Al_2O_3; for example, activation energies for oxygen diffusion in amorphous and γ-Al_2O_3 have been shown to be five times lower than that in α-Al_2O_3.[174]

To conclude, we cannot rule out either of the potential explanations of the FTIR spectra: the chemical species formed after photooxidation of hydroxyls may be difficult to detect, capable of diffusing out of the film, or both. Any of these possibilities is plausible and compatible with main conclusions presented in Chapter 3. Future studies aimed at distinguishing among them should include further analysis of impurities in the films as well as any gases evolved during irradiation.

Note 3.3: Estimate of ξ from $n\rho^3$ vs. ξ from T_{ES}.

It has been shown[126] that ξ in a network of NCs with diameter d, free electron density n, and interparticle contact radius ρ can be estimated from

$$\xi = A\frac{d}{\ln(2/n\rho^3)} \tag{S3.7}$$

provided that (1) the network is far from the IMT on the insulating side and at low temperature so that electron hopping proceeds via elastic cotunneling through chains of NCs and (2) the number of free electrons per NC is greater than $\alpha^{-3/2}$, where $\alpha = 2\delta d/d$. A is a constant of order unity. Applying Equation S3.7 to our sample farthest from the IMT ("0+0", $n\rho^3$ = 0.17) and assuming A = 1, we obtain ξ = 4 nm. For comparison, using Equation 3.4 and T_{ES} = 2600 K while assuming ε = 9, we obtain ξ = 7 nm. Equation S3.7, however, should not be applied to samples approaching the IMT, because it is invalid when $\xi > d$ (for details, see ref. 126). Hence we use scaling theory to model the dependence of T_{ES} on $n\rho^3$ near the IMT, as shown in Figure 3.5d.

Appendix C: Copyright permissions

Chapters 2 and 3 were published in an American Chemical Society (ACS) journal. The ACS copyright policy states: “ACS extends blanket permission to students to include in their theses and dissertations their own articles, or portions thereof, that have been published in ACS journals or submitted to ACS journals for publication, provided that the ACS copyright credit line is note on the appropriate page(s)”. An expanded version of Section 5.5 was published in an American Institute of Physics (AIP) journal. AIP grants authors permission to include their published articles in dissertations.